PHOTOCHEMICAL DEPOSITION OF METAL AND METAL OXIDE FILMS FROM AMORPHOUS FILMS OF INORGANIC PRECURSORS

by

Sharon Louise Blair

B. Sc. St. Francis Xavier University, 1991

THESIS SUBMITTED IN PARTIAL FULFILLMENT OF

THE REQUIREMENTS FOR THE DEGREE OF

DOCTOR OF PHILOSOPHY

in the Department

of

CHEMISTRY

SIMON FRASER UNIVERSITY

December 9, 1996

ISBN 0-612-16802-6

PARTIAL COPYRIGHT LICENSE

I hereby grant to Simon Fraser University the right to lend my thesis, project or extended essay (the title of which is shown below) to users of the Simon Fraser University Library, and to make partial or single copies only for such users or in response to a request from the library of any other university, or other educational institution, on its own behalf or for one of its users. I further agree that permission for multiple copying of this work for scholarly purposes may be granted by me or the Dean of Graduate Studies. It is understood that copying or publication of this work for financial gain shall not be allowed without my written permission.

Title of Thesis/Project/Extended Essay:

Photochemical Deposition of Metal and Metal Oxide Films from Amorphous Films of Inorganic Precursors

Author: _____
(signature)

_____
(name)

Dec. 18/96
(date)

APPROVAL

Name: Sharon Louise Blair

Degree: Doctor of Philosophy (Chemistry)

Title of Thesis: Photochemical Deposition of Metal and Metal Oxide Films from Amorphous Films of Inorganic Precursors

Examining Committee:

Chairperson: Dr. I. D. Gay

Ross H. Hill, Senior Supervisor
Associate Professor of Chemistry, S. F. U.

Derek Sutton, Supervisory Committee
Professor of Chemistry, S. F. U.

Andrew J. Bennet, Supervisory Committee
Assistant Professor of Chemistry, S. F. U.

Gary Leach, Internal Examiner
Assistant Professor of Chemistry, S. F. U.

David C. Johnson, External Examiner
Associate Professor of Chemistry
University of Oregon

Date Approved: Dec 18/96

Abstract

This thesis will describe the photochemistry of amorphous films of inorganic complexes. Photolithographic deposition of metal and metal oxide patterns from amorphous film precursors could reduce the number of steps presently used in computer chip fabrication. The ultimate goal of the research presented in this thesis is to develop methods to lithograph useful materials *via* the photolysis of amorphous films of inorganic complexes on silicon.

The solid state photochemistry of d^8 triplet ground state molecules of the formula *trans*-NiL_4X_2 (L_2= $Et_2NC_2H_4NH_2$, $MeHNC_2H_4NMeH$, X= NO_2, NO_3, NCS) will be presented. This study demonstrated that photoreactions of complexes that are generally labile in solution can be studied in the amorphous solid state. The weak field ligand, X, was photoejected from the weak field axis of these complexes. The ligand, X, was lost photochemically as either the ion or as the radical *via* ligand to metal charge transfer (LMCT) excitation.

The solid state photodecomposition reaction of $Fe(CO)_4PPh_3$ was studied in detail. The primary photoreaction is loss of CO, forming $Fe(CO)_3PPh_3$, followed by rapid thermal decomposition. The photodecomposition reaction was manipulated by trapping the primary photoproduct with PPh_3, forming the thermally stable and photosensitive *trans*-$Fe(CO)_3(PPh_3)_2$. The quantum yield for decomposition of amorphous films of

$Fe(CO)_4PPh_3$ is inversely proportional to the film thickness. This effect is related to the amount of CO available for backreaction with the $Fe(CO)_3PPh_3$ fragment.

A single photon mediated decomposition was observed for films of L_2PtMeN_3 (L_2= dppe/2, PPh_3, PEt_3) and *trans*-$(R_3P)_2M(X)_2$ (M= Ni, R= Et, X= NO_2, NCS, CN; M= Pd, Pt, R= Et, X= NO_2; M= Ni, R= Bu, X= NO_2). The photodeposition of nickel, palladium and platinum films by this method is compatible with current lithographic technology.

Elementally pure oxides of Zr, Pb, Mn, Fe, Ca, Sn and Ti have been deposited photochemically from thin film precursors. This study demonstrated that metal carboxylate as well as acetylacetonate compounds are suitable precursors for the deposition of metal oxides. The required dose to deposit patterns from lead (II) 2-ethylhexanoate was 44 $mJcm^{-2}$. This dosage is compatible with current resist technology. The dose to print from the other precursors was one to three orders of magnitude greater than current resist technology.

If a mixture of metal 2-ethylhexanoates and metal acetylacetonate precursors are codeposited, the mixed metal oxide is produced. Films of contaminant-free $PbZrO_3$, $PbTiO_3$, $Pb(Zr_{0.5}Ti_{0.5})O_3$ were deposited. Various other mixed metal oxides were prepared, for example, $LiMnO_2$, $BaTiO_3$, $BiMnO_3$ and $BaBiO_3$.

Dedication

To those who made it possible...my parents,

Hollis Andrew Blair

and

Margaret Louise Blair

Acknowledgements

I would like to thank my supervisor, Ross H. Hill for his friendship and continuous encouragement.

I would also like to thank the past and present members of my group as well as Sean Clancy for their valuable friendship and support.

I express my appreciation to Wenjia Xia for preliminary experiments on the octahedral nickel complexes. I also thank Dr. Doug G. Bickley for generously supplying some of the compounds used.

I would also like to thank Dr. Brett Heinrich and Ken Myrtle at the Surface Physics Laboratory (Simon Fraser University). They taught me how to use the scanning Auger microprobe, and allowed me to use it freely.

I thank Dr. Jeff Dahn, Immo Koetschau and Alf Wilson, Department of Physics (Simon Fraser University) for their help obtaining and interpreting X-ray powder diffraction spectra. I also thank Dr. Simon Watkins and Dr. George Soerensen, Department of Physics (Simon Fraser University) for the AFM image.

I would also like to express my appreciation to Dr. Vic Bourne, Department of Biological Sciences (Simon Fraser University) for the use of the scanning electron microscope as well as for many interesting discussions.

Finally, I would like to thank Dr. Ross H. Hill and Simon Fraser University for their generous financial support.

Table of Contents

List of Tables

List of Figures

List of Abbreviations

A	absorbance in the FTIR spectrum
A_o	initial absorbance in the FTIR spectrum
A_t	absorbance at time, t
acac	acetylacetonate $(CH_3COCHCOCH_3)^-$
AES	Auger electron spectroscopy
AFM	atomic force microscope
a-Et_2en	N, N-diethylethylenediamine $(C_2H_5)_2NC_2H_4NH_2$
B. M.	Bohr Magnetons
Bu	butyl (C_4H_9)
COD	1, 5-cyclooctadiene (C_8H_{12})
CT	charge transfer
CVD	chemical vapour deposition
DNQ	diazanaphthaquinone
dppe	diphenylphosphinoethane ($Ph_2PC_2H_4PPh_2$)
ε	extinction coefficient in units of cm^2mol^{-1}
ε'	dielectric constant
ε_o	permittivity of free space in units of $CV^{-1}m^{-1}$
Et	ethyl (C_2H_5)
Φ	quantum yield for decomposition
Φ^o	quantum yield for the loss of CO
e-beam	electron beam
FTIR	Fourier transform infrared
HOMO	highest occupied molecular orbital
I_o	incident light intensity in units of $Ecm^{-2}s^{-1}$
IC	integrated circuit
ILD	inter-layer dielectric
i-prop	isopropoxide $(-OCH(CH_3)_2)$

IR	infrared
k_T	rate of thermal decomposition in units of s^{-1}
LMCT	ligand to metal charge transfer
μ_{eff}	magnetic moment in units of B.M.
Me	methyl (CH_3)
MLCT	metal to ligand charge transfer
PCVD	photochemical vapour deposition
Ph	phenyl (C_6H_5)
PZT	lead zirconate titanate ($Pb(Zr_xTi_{1-x})O_3$)
R	alkyl or aryl
SAM	scanning Auger microprobe
s-Me_2en	N, N'-dimethylethylenediamine $(CH_3)HNC_2H_4NH(CH_3)$
SEM	scanning electron microscope
2θ	diffraction angle
UV	ultraviolet
vac	vacuum
vis	visible
XRD	X-ray diffraction

Chapter 1

Introduction

1.1 Photolithography of metals and metal oxides

This thesis will describe the photolithography of metals and metal oxides from amorphous films of inorganic complexes. The direct patterning of materials has great potential in the electronics industry. Photolithographic deposition of metal and metal oxide patterns from amorphous film precursors could reduce the number of steps presently used in computer chip fabrication. The ultimate goal of the research presented in this thesis is to develop methods to lithograph useful materials *via* the photolysis of amorphous films of inorganic complexes on silicon.

The development of metal and metal oxide photolithography from amorphous films of inorganic precursors provokes many questions that will be addressed in this thesis. To solve the practical problems many fundamental issues must be addressed. Some of the questions that need to be answered are: Can metal and metal oxide films be deposited photochemically from the solid state? What are the photoreactions that occur upon irradiation of the films? Can we produce technologically important materials? Are the photolysed products free of impurities? How efficient is the process of decomposition? Is photolithography of materials from films of transition metal complex precursors a useful technology?

In the following sections, some background will be provided that will be useful for understanding the research undertaken in this thesis. Sections 1.2 and 1.3 will provide

background about current deposition methods and lithography techniques in the electronics industry. Section 1.4 discusses target materials for photochemical deposition and their uses in electronics. Sections 1.5 and 1.6 will present background information on the photochemistry of inorganic and organometallic complexes as well as for quantum yield determinations. Section 1.7 discusses requirements to deposit and study the photochemistry of amorphous precursor films. Section 1.8 describes the surface sensitive analysis methods used to study product films. Finally, Section 1.9 will provide the research outline for this thesis.

1.2 Deposition methods for thin films of metals and metal oxides in electronics

In this section, some background of deposition methods which are used in lithography will be given. There is a great deal of interest in the preparation of films of metals and metal oxides due to applications in electronic devices [1-14]. One approach to deposition has been from the vapour phase *via* either chemical [15] or photochemical [16] vapour deposition (CVD/PCVD). Other approaches are deposition from thin films in sol-gel coating [17] and by sputter deposition [18].

In chemical vapour deposition (CVD), one or more gases react at a substrate to form a film. Photochemical vapour deposition requires the addition of light to deposit the film. To deposit pure films by CVD/PCVD methods, there are strict requirements for the precursors. The molecule must have a high enough vapour pressure for transport to the reaction chamber, yet it must have high thermal stability to prevent particle formation in the gas phase. In this method, controllable film growth rate, and smooth films are

attainable. Significant disadvantages include high capital cost and high process temperatures for many materials [19].

In the sol-gel method [17], the sol is spin- or dip- coated onto the substrate. A sol is a colloidal suspension of particles in a liquid. The sol undergoes a sol-gel transition to a rigid two-component system of solid and solvent pores, followed by removal of the solvent. This sol-gel transition is often made by hydrolysis of a film of a metal alkoxide. Important parameters for this process include: temperature, pH, amount of water, solvent and precursor. The gel, which is usually amorphous and porous, can be converted to pure target material (MO_x) by annealing to crystallise the film. Annealing temperatures of only 1/2 to 1/3 melt temperatures in K are generally required with this method [19].

The sol-gel method is a good method for the deposition of pure, homogeneous metal oxide films. The resultant films are porous, therefore, for applications requiring a dense material, an annealing step is necessary. Less volatilisation of metals occurs during the deposition process than with the CVD process. This provides greater control over the composition when mixed metal oxide materials are desired. Another advantage of this method is its efficient material usage. Excess precursor material can be recovered and reused. The disadvantage of sol-gel coating is the cost of raw materials, which makes the process ideal only for specialty applications [19].

Sputter deposition is another common method of metal and metal oxide film deposition. It involves bombardment of a target (metal or metal oxide) with an ion beam (usually argon), having an energy of at least four times the bond energy of the target. This knocks atoms from the target loose thus providing a source of atomised material

which hits the substrate [18, 19]. It is a good method for depositing smooth, uniform films. Films produced this way exhibit good adhesion. Film growth rate is controllable, hence the thickness of films deposited by this method is reproducible. Growth rates are also high, and are comparable to evaporation rates. This deposition method requires moderate vacuum conditions (approx. 0.1 torr) for deposition [20].

Sputter deposition and CVD/PCVD require vacuum chambers [19]. Thermal CVD typically requires relatively high process temperatures to deposit the desired form of the materials [21]. The current methods mentioned deposit metals and metal oxides nonselectively, although photoassisted CVD is capable of patterning [4, 16].

The photochemical deposition from amorphous precursor films does not require a volatile precursor. The precursor film is deposited by applying a drop of an inorganic complex in a volatile solvent onto a spinning substrate. The film is irradiated with UV light, and all ligands are ejected from the precursor, yielding the metal. In the presence of oxygen, the metal oxide is formed. The films resulting from photolysis of the precursor exhibit good adhesion. Metal and metal oxide films deposited by this technique have similar advantages as sol-gel coating. This deposition method has the added advantage of selective patterning at ambient temperature. It has, on the other hand, certain requirements that must be met. The precursor complex must be thermally- as well as air stable, and it must be photosensitive. The metal complex must be soluble in a volatile solvent or be a liquid for spin coating. The precursor must be able to form optical quality films for lithography. Films that are amorphous exhibit good optical quality.

1.3 Lithography

Lithography is the process of the patterning of a material on a substrate. Photolithography is an integral part of computer chip fabrication [18, 22]. The present technology for processing a chip containing a number of devices involves a multistep fabrication process. Figure 1.1 outlines one typical process for the deposition of a metal pattern. It involves 1) the deposition of a photoresist by spin coating onto the substrate. This is followed by 2) irradiation of the resist through a lithography mask. Irradiation of the resist renders it more soluble. The exposed resist is then 3) developed to remove exposed areas. The chip is then 4) nonselectively coated with the required metal. All excess material is then removed by 5) an etching process. Patterns of the metal remain on the surface in the negative pattern of the mask. Positive photoresists are also available, and following a similar process, positive patterns are made. Positive resists become less soluble after exposure, therefore the unexposed regions are rinsed after photolysis. After nonselective coating of the metal and subsequent etching, metal patterns in the positive image of the mask remain.

Figure 1.1 A current fabrication process

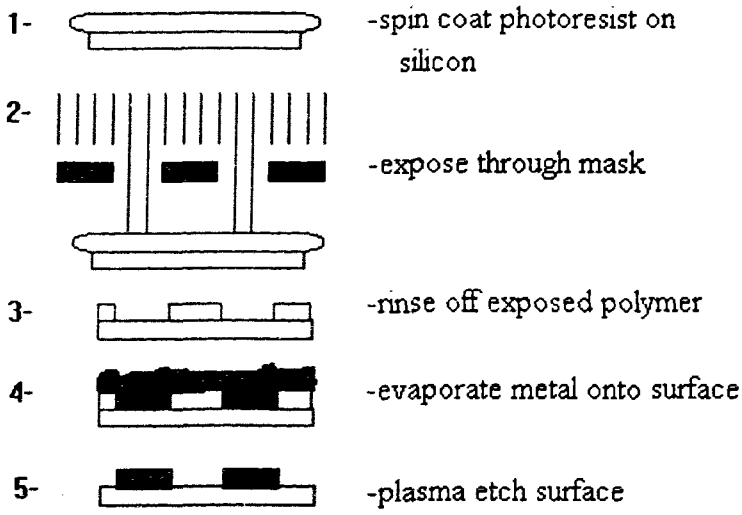

The process of photoresist-free lithography is shown in Figure 1.2. It is a process that has fewer steps than conventional lithography. The process consists of 1) spin coating a film of a photosensitive inorganic compound onto the substrate. The precursor film is then 2) irradiated through a lithography mask. This converts the complex to metal (or metal oxide) in the exposed regions of the film. 3) Rinsing the unexposed regions after photolysis leaves a pattern of the metal (or metal oxide) on the surface. This process does not require a resist. It also does not require an etchant, which is a difficult problem for the patterning of many materials [23].

Figure 1.2 Photoresist free deposition

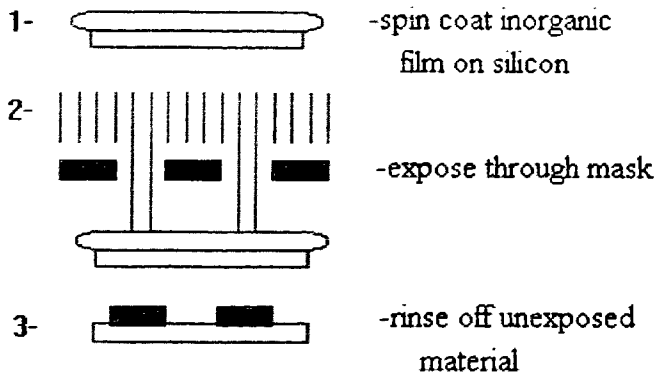

1.4 Target materials for photochemical deposition from amorphous precursor films

One of the goals of my research was to explore the photochemical deposition of technologically important materials from amorphous precursor films. The three groups of materials that were chosen were metals (M), metal oxides (M_xO_y) and mixed metal oxides ($M_wM'_xM''_yO_z$). This section will outline some uses of these materials. This is important as the potential uses of the materials set the requirements (e.g. purity, crystallinity) for deposition.

Metal films are used to make contacts and conducting wires in integrated circuits (IC) [24]. Metal-semiconductor contacts can be made to form Shottky diodes [25]. Platinum is a common metal used in Schottky diodes. Palladium and platinum are also used as gate electrode materials in sensors [26]. Nickel is used as an adhesion layer and as a barrier layer for Cu on polyimide [27]. In this thesis, nickel, palladium and platinum are the target materials for these electronics applications.

Metal oxides and mixed metal oxides are also important materials in ICs. Due to the insulating nature of many metal oxides, they are often used as dielectrics for

capacitors (e.g. Ta_2O_5, Al_2O_3, TiO_2) [27]. They may also be used as interlayer dielectrics (ILD) to electrically separate components [28]. The MO_2 oxides, where M is nickel, titanium, manganese and iron have uses in electrochromic devices [29]. Tin oxide, SnO is a common material for gas sensors [26]. These applications do not require contaminant-free materials.

Mixed metal oxides have numerous properties that may be utilised in electronics. One use of a mixed metal oxide is in micromachining. Addition of CaO or Y_2O_3 to zirconia (ZrO_2), renders the zirconia not brittle, introducing a new class of nonbrittle ceramics. This is an excellent insulating material for electronics applications that sustain mechanical abuse [27]. Mixed metal oxides such as $LiMn_2O_4$ and $LiNiO_2$ also have applications as electrodes in thin film batteries [30, 31].

Many ferroelectric materials are mixed metal oxides. By altering the values of w, x and y in $M_wM'_xM''_yO_z$, the property of interest, such as dielectric constant, can be fine-tuned. The deposition of ferroelectric materials has been intensively investigated recently, due to the wide range of applications of these materials [26, 32-35]. Each of the target metal oxides studied in Chapter 6 can be used as a component in a mixed metal oxide to form a ferroelectric material [36].

Ferroelectrics are a sub-class of piezoelectrics. Piezoelectrics are non-centrosymmetric and possess a unique polar axis. If a change in polarisation is observed with a change in temperature the material is also pyroelectric. If the polarity of a pyroelectric crystal can be reversed by the application of an electric field, then it is known as a ferroelectric. Ferroelectric materials have applications in the electronics industry

involving devices for non-volatile memory and logic circuits on silicon and gallium arsenide, and these applications require the use of thin films [37].

$PbTiO_3$ is a ferroelectric material, and has been the ferroelectric material most investigated for its potential applications in electronics. A $PbTiO_3$ film has a relative dielectric constant, ε', of approximately 80, compared with 8 for Al_2O_3, and 27 for Ta_2O_5 [27]. Substitution of Ti with Zr, forming $Pb(Zr_xTi_{1-x})O_3$ (PZT), results in a dramatic increase in relative dielectric constant (ε' for PZT is ~1000, for x~0.5) [38]. Due to its high dielectric constant, PZT can be used as the dielectric material in high capacitance capacitors.

A capacitor consists of two electrodes separated by a dielectric material. The use of PZT in a capacitor would effectively reduce the area occupied by the capacitor on the chip. This can be explained by the relationship shown in equation 1.1. The capacitance, C, is related to the dielectric constant of the material ($\varepsilon'\varepsilon_o$), the area of the capacitor, A, and the separation between the electrodes, d. To make two films of the same thickness with equivalent capacitance, the material with the higher dielectric constant, ($\varepsilon'\varepsilon_o$), requires a smaller area. Therefore, ferroelectric capacitors would occupy less space on a computer chip than conventional capacitor materials.

$$C = (\varepsilon' \varepsilon_o A)/d \qquad (1.1)$$

C (CV^{-1})= capacitance
ε'= relative dielectric constant of the material
ε_o (8.85×10^{-12} $CV^{-1}m^{-1}$)= permittivity of free space
A (m^2)= area of the capacitor
d (m)= separation between electrodes

1.5 Excited states of inorganic complexes

One of the most efficient ways to induce chemical reactions is with the use of light. There are six types of electronic transitions resulting from irradiating transition metal complexes. These are: ligand field (LF or d-d), ligand-to-metal charge transfer (LMCT), metal-to-ligand charge transfer (MLCT), metal-to solvent charge transfer (MSCT), metal-to-metal charge transfer (MMCT) and intraligand (IL). The first three lead to excited states which result in ligand loss. Therefore, only these will be discussed.

Ligand field (LF or d-d) excited states result from the transfer of an electron between two metal d-orbitals. Carbon donor ligands are relatively high in the spectrochemical series, hence d-d transitions for organometallic complexes are observed at higher energy (in the UV-vis region) than for classical inorganic complexes. The extinction coefficient for these transitions is higher for organometallic (10^3 to 10^4 $M^{-1}cm^{-1}$) than for classical inorganic (10^1 to 10^2 $M^{-1}cm^{-1}$) complexes. The greater covalency of organometallic complexes leads to the metal d-orbitals having significant ligand character. This leads to LF bands for organometallic complexes having significant charge-transfer character and high transition dipole. LF excitation often results in efficient ligand loss in organometallic complexes [39].

Ligand-to-metal charge transfer excited states result from transfer of an electron from a ligand-based orbital to an orbital of primarily metal d- character. The result is reduction of the metal and oxidation of the ligand. These transitions are generally found in the UV region. LMCT excited states are usually found for complexes containing reducing ligands (e.g. NO_2^-, Cl^-) [39]. LMCT excitation often results in ligand loss [40].

Metal-to-ligand charge transfer excited states result from the transfer of an electron from an orbital of primarily metal d- character to a ligand orbital. The result of this excited state is oxidation of the metal and reduction of the ligand. This excitation is likely to occur in complexes with central atoms that have low ionisation potentials, and ligands with low energy empty π^* orbitals (e.g. CN^-, CO) [39].

1.6 Determination of quantum yield in amorphous films

The first law of photochemistry states that, "Only radiations which are absorbed by the reacting system can be effective in producing chemical changes" [39]. The second law states, "Each light quantum absorbed activates one molecule" [39]. The quantum yield, Φ, is defined as the number of molecules that undergo a specific reaction per photon absorbed (equation 1.2). Therefore, the maximum value for a quantum yield is unity, for a molecule that requires the absorption of one photon for reaction.

$$\Phi = \frac{\text{number of molecules undergoing a process}}{\text{number of photons absorbed}} \qquad (1.2)$$

The quantum yield calculations presented in this thesis are all quantum yields for decomposition of a species. A plot of FTIR absorbance *vs.* photolysis time is made for a photoreaction at a specific wavelength. The data from this plot are fit to an exponential decay according to equation 1.3. The equation used to calculate the quantum yield,Φ, (eq. 1.3), has been derived previously in our laboratory [41-43].

$$A_t = A_o \exp[(-2.303\, I_o\, \varepsilon \Phi)t] \qquad (1.3)$$

A_t = absorbance in the infrared region at time t
A_o = initial absorbance in the FTIR
I_o ($Ecm^{-2}s^{-1}$) = incident light intensity at the excitation wavelength
ε (cm^2mol^{-1}) = molar extinction coefficient at the excitation wavelength
Φ = quantum yield
t (s) ≡ photolysis time

1.7 Precursor requirements for metal and metal oxide photodeposition

The use of amorphous films as precursors for photochemical deposition of materials allows us to learn about reactivity of molecules in the amorphous solid state. It may also provide a method to study the photochemistry of complexes that are labile in solution. The photodecomposition of films of inorganic complexes is a low temperature process for the deposition of metal and metal oxide films. Metal and metal oxide films have been deposited by laser irradiation of inorganic thin films [44]. However, this was often a thermal process, utilising heat generated from the laser for reaction. The reactions involved in the process of laser irradiation were not studied [44].

There are some precursor requirements for the photochemical deposition of materials from inorganic film precursors. The precursor films must be amorphous for efficient photochemical decomposition. In crystalline films, the recombination of ejected ligands occurs more readily, forming starting material. This would lead to highly inefficient decomposition reactions. Significant recombination would also incorporate another factor in the quantum yield expression. This makes determination of the photoefficiency more complicated.

The precursor molecules must be air- and moisture stable. They must also be photosensitive. In order to monitor the photochemistry of a molecule by FTIR spectroscopy, the film must be thick enough to exhibit observable bands in the infrared spectrum that are associated with the molecule. The film thickness must also be less than the wavelength of light used to irradiate the film. This ensures uniform irradiation throughout the sample [41-43].

The spin-coated film can range from a liquid to a powder to a uniform gel-like amorphous film. The films would not flow if scratched (i.e. the scratch would remain intact). The spin-coated films are reasonably uniform. For example, the thickness variation across a 4" wafer was less than 4 nm for a 400 nm film. These properties will be discussed in more detail in chapter 6.

1.8 Surface sensitive analysis methods

Irradiation of amorphous films of inorganic and organometallic complexes often results in the photoextrusion of all ligands, as monitored by FTIR spectroscopy. To characterise the products of these reactions surface analysis techniques are needed. The surface analysis techniques that we use are relatively nonstandard for chemists and will therefore be described. These include: optical interferometry, Auger electron spectroscopy (AES), scanning electron microscopy (SEM) and x-ray powder diffraction (XRD).

1.8.1 Optical interferometry

Optical interferometry is a technique which can be used to measure film thickness. The interferometer is a Michelson interferometer (Figure 1.4). A thin film is made by masking a portion of the substrate with adhesive tape, and spin coating a solution of the complex onto this substrate. At this point the mask may be removed, exposing a step-edge. The film is placed under the microscope objective, the step-edge is brought into focus, and an interference filter is placed in the light path. The light from the microscope

passes through a beam splitter, with a portion of the beam going to a movable mirror, and the other to the film-substrate edge. The light reflected back from the sample and the mirror gives interference fringes. At the step-edge, the difference in pathlength provided by the film and the substrate results in a shift in the interference fringes. The magnitude of this shift (measured as a fraction of the fringe) is related to the thickness of the film by equation 1.4. The film thickness can be determined before and/or after photolysis. [21]

Figure 1.3 Optical Interferometer

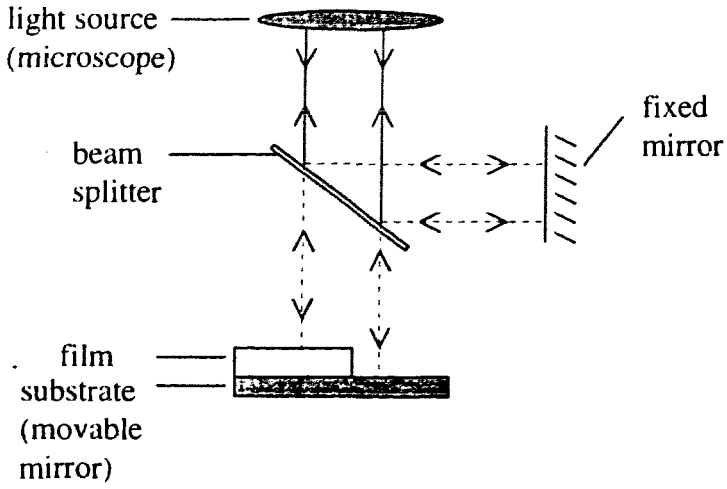

$$\text{film thickness} = N\lambda / 2 \qquad (1.4)$$

N= fringe shift, λ= wavelength

1.8.2 Auger electron spectroscopy

Auger electron spectroscopy (AES) is a method used to determine elemental composition of surfaces. The principle of this technique can be described as follows. A sample is exposed to an electron beam (1 to 10 keV). An incident electron, hits the sample and ejects a core electron from an energy level, E_x. The vacancy caused by ejection of the core electron is then filled by another electron from a higher energy level, E_y, releasing an amount of energy equivalent to $E_x - E_y$. This energy can appear as an X-

ray photon, or, can be given up to a third electron, (the Auger electron), from an energy level, E_z. The Auger electron, having a kinetic energy, E_k, is then ejected from the sample (Figure 1.4). The kinetic energy of the Auger electron, E_k, is given by equation 1.5. The energy of Auger electrons is specific to each element, and the technique can be used to determine relative amounts of each element. In this way it may be used to infer stoichiometry. The technique is surface specific, providing information on the top 10 to 30 Å of the film. A profile of elemental composition with depth can be made by sputtering the film with argon ions and analysing the exposed inner portions of the film [45, 46]. Preferential sputtering may occur, therefore, the stoichiometry inferred from inner portions of the film may have a larger error [46].

Figure 1.4 An Auger process

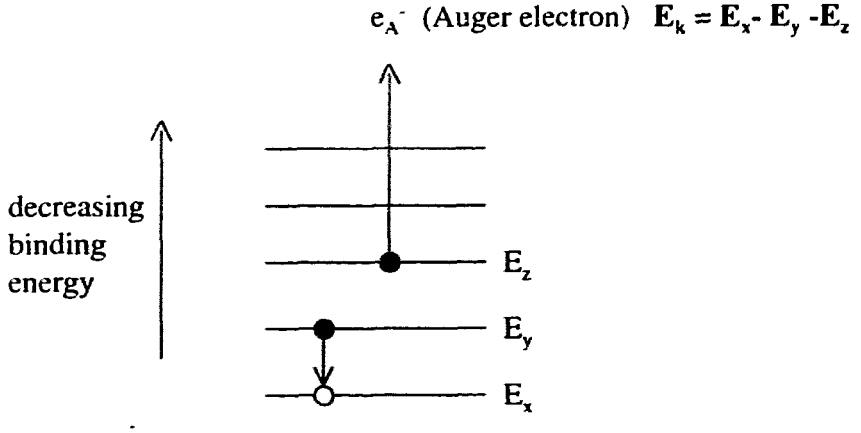

$$E_k = E_x - E_y - E_z \qquad (1.5)$$

1.8.3 Scanning electron microscopy

The scanning electron microscope (SEM) is a useful imaging tool. It can be used to observe the morphology of a surface, as well as determine if features are resolved [47]. The SEM uses a focused electron beam (e-beam) that scans over the surface of a sample. The impinging e-beam ejects secondary electrons from the sample (max. escape depth is approx. 5 nm). The secondary electrons that are emitted are detected by an electron multiplier tube, converted to a voltage signal and imaged on a cathode ray tube (CRT) screen. Small projections on a surface have larger areas of shorter pathlength for the electrons to escape the surface (i.e. more secondary electrons emitted) than flat regions. The more secondary electrons that hit the detector the brighter the image. Hence, a topographical profile may be obtained. The magnification of the image may range from 10x to 100,000x [47].

1.8.4 X-ray diffraction

X-ray powder diffraction is a tool which yields information on the periodic arrangement of atoms [48]. X-rays are electromagnetic radiation with short wavelengths (i.e. a few ångstroms). Since these wavelengths are comparable to interatomic spacings, X-rays are easily diffracted from crystals. This property is used to give us information on the arrangement and the spacing of atoms, and is a practical means for identification of crystalline compounds. The source of monochromatic X-rays is an X-ray tube with suitable filters. When thin films are used, the source is often situated at grazing incidence (typically $< 5°$) to the sample to reduce diffraction patterns originating from the substrate.

The beam of X-rays impinges on the sample at an angle, θ, with respect to the surface and diffracts. The diffracted beams are detected by a scintillation counter which scans a range of diffraction angles. The intensity of the signal is plotted against the angle (2θ). The intensity and spacing of these peaks are used to empirically determine the structure by comparing the spectrum to a database of standard spectra [46, 49].

1.9 Research outline

There were three distinct goals for the research undertaken for this thesis. The first goal, was to investigate the photochemistry of thin amorphous films of inorganic complexes. The second, was to determine if we could lithograph patterns of material by selectively irradiating amorphous films of precursor molecules. The third was to develop this technique for the deposition of technologically useful materials. Chapters 2 through 5 describe the photochemistry of various d^8 inorganic complexes, which demonstrate that patterns of product material can be made. Chapter 6 deals with the deposition of pure metal oxide as well as mixed metal oxide ($M_wM'_xM''_yO_z$) materials using metal 2-ethylhexanoate precursors.

In Chapter 2, the photochemistry of triplet ground state octahedral molecules of nickel will be described. This study demonstrated that such systems that are labile in solution can be effectively studied in the solid state. Chapter 3 describes the photochemistry of thin amorphous films of the trigonal bipyramidal molecule, $Fe(CO)_4PPh_3$. The mechanism of this photoreaction was studied in depth, and experiments demonstrated that trapping of reactive intermediates is possible in the

amorphous solid state. Chapter 4 describes the study of square planar d^8 molecules of the formula $L_2Pt(CH_3)(N_3)$ (L = dppe/2, PPh_3, PEt_3) with the aim of producing thin Pt films with a single photon mediated process. The results of this study indicate that the photochemistry is consistent with a single photon mediated decomposition of the platinum complexes. All ligands are ejected from the complexes upon photolysis. However, phosphorus impurity remained a problem. This led to the more detailed study, described in Chapter 5, of square planar complexes of Ni, Pd and Pt with the general formula *trans*-$(R_3P)_2M(X)_2$. In this chapter, we describe how the pseudohalide ligand was varied to investigate and compare the mechanisms and the photoefficiency of decomposition of the molecules. In the case of *trans*-$(Et_3P)_2Ni(NO_2)_2$, all ligands were lost upon photolysis, with no nitrogen or phosphorus impurity in the final film, however, carbon and oxygen impurities remained a problem. Experiments demonstrated that the reactions were truly molecular in nature. In other words, the reaction efficiency was independent of the film-vacuum and film-substrate interface. Lithographic patterns resultant from photolysis of thin films of d^8 complexes through a mask were obtained for the compounds studied in Chapters 3 through 5. This demonstrated that the process of lithographic deposition from amorphous inorganic precursors is compatible with current lithography technology.

It was found in our laboratory, that metal complexes (e.g. U, Cu) containing carboxylate [41, 50] and acetylacetonate (e.g. U) [51] ligands were photosensitive and yielded pure metal oxide films. Chapter 6 dealt with a range of pure metal oxide films that could be deposited with this technique. The goal of this project was to determine

suitable precursors for the deposition of useful mixed metal oxide films. In Chapter 6 it was demonstrated that pure $Pb(Zr_{0.5}Ti_{0.5})O_3$ films could be deposited. Upon annealing of the irradiated film, a polycrystalline form of the tetragonal perovskite, ferroelectric phase, was formed and was confirmed by x-ray diffraction.

In summary, an ambient temperature process for photoresist-free lithographic deposition of metals and metal oxides has been demonstrated. Results also confirmed that ejection of all ligands may be induced photochemically from amorphous films of inorganic precursors. Technologically useful materials were deposited by this technique. For example, impurity-free metal oxide films of lead, zirconium, titanium, manganese, iron, tin, and calcium were prepared photochemically at room temperature. To my knowledge, the photolithography of PZT by this method is the first demonstration of direct patterning of a ferroelectric material. The dosage required to pattern lead oxide on silicon is 44 $mJcm^{-2}$ and is comparable to photoresist technology. These studies indicate that the photochemical deposition of materials from inorganic precursors is a viable process and is compatible with current methods in the electronics industry.

Chapter 2

Photochemistry of Triplet Ground State d^8 Octahedral Nickel Complexes in the Solid State

2.1 Introduction

In this chapter, the solid state photochemistry of *trans*-NiL_4X_2 (L_2= $Et_2NC_2H_4NH_2$ (a-Et_2en), $MeHNC_2H_4NMeH$ (s-Me_2en), X= NO_2, NO_3, NCS) molecules will be presented. These nickel complexes, with the exception of *trans*-Ni(a-Et_2en)$_2$(NO_3)$_2$, are d^8 octahedral triplet ground state molecules. The complex, *trans*-Ni(a-Et_2en)$_2$(NO_3)$_2$ is diamagnetic (it has a singlet ground state). Octahedral nickel complexes are generally labile in solution. One objective of this study is to elucidate the mechanisms of photodecomposition of these complexes in the solid state. Another objective is to determine if the weak field ligands are ejected from the weak field axis on photolysis for this series of complexes.

There is little evidence pertaining to the photochemistry of complexes of the type Ni(R_2en)$_2X_2$ in solution. This is likely due to the lability of the anionic ligands in many complexes of this formula [52, 53]. However, extensive studies have been carried out on various complexes containing these ligands in solution [40, 54]. Photochemical loss of amine ligands from coordination complexes is well known [39, 55]. Charge transfer irradiation of complexes containing NO_2 is known to result in the reduction of the metal and the formation of NO_2, a volatile product [56-58]. Alternatively, linkage isomerism of the NO_2 ligand has been reported to be the primary photochemical process for

$[Pd(MeEt_4dien)NO_2][NO_3]$ ($MeEt_4dien$ = 1,1,7,7-tetraethyldiethylenetriamine) in solution [59]. Linkage isomerism of the NO_2 ligand has also been observed in the surface photochemistry of *fac*-$Co(NH_3)_3(NO_2)_3$ [60]. Solution studies of the photochemical loss of NCS have demonstrated that both homolytic and heterolytic cleavages of the metal-nitrogen bond occur [40, 54]. The results of these studies indicate that numerous reaction pathways are possible on photolysis of the series of complexes reported here.

The series of complexes discussed in this chapter may yield some insight into the photoreactivity of nickel complexes in which the axial ligands are at weak field with respect to the equatorial ligands. The anionic ligands used in this study are at weak field with respect to the amine ligands and have a *trans* orientation. The mode of bonding in the nitrite complexes is *via* the oxygen, as a nitrito ligand, and hence it is a weak field ligand, whereas if it were N- bound, $-NO_2$ would be a strong field ligand. This is of importance in the prediction of the photochemistry of the complex. For example, in the photochemistry of d^6 and d^3 metal ions, the general trend observed is that the strong field ligand from the weak field axis is photoejected upon ligand field photolysis [61]. A molecular orbital model may be used to rationalise this trend in terms of occupation of the strongly antibonding e_g orbitals. If a similar reactivity is observed with the d^8 complexes studied here, d-d excitation will result in the loss of the weak field ligand (since all complexes are *trans*). In the series of complexes discussed in this chapter, such reactivity will result in the loss of the anionic ligand.

2.2 Results

2.2.1 Preparation of the films

Thin amorphous films of the complexes were deposited onto silicon substrates by spin coating (Figure 2.1). The complex, *trans*-Ni(a-Et_2en)$_2$(NO_2)$_2$ was dissolved in CH_2Cl_2. A drop of this solution was dispensed onto a spinning silicon chip. The solvent evaporated leaving a film of the complex on silicon. The nature of the ligand was crucial for the formation of amorphous films as well as to the resultant film thickness. Complexes *trans*-Ni(R_2en)$_2X_2$ (X= NO_2, NO_3, NCS) with either the asymmetric ethyl substituted (a-Et_2en) or the symmetric methyl substituted (s-Me_2en), could be spin coated from CH_2Cl_2 solutions. Complexes containing the parent ethylene diamine (en) ligand, *trans*-Ni(en)X_2 (X= NO_2, NO_3, NCS), did not yield films thick enough to be detectable by FTIR spectroscopy. This is attributed to the low solubility of these complexes. Attempts at utilising other solvents (such as CH_3OH) to deposit films were unsuccessful. Also, the films that were deposited from complexes containing the en ligand had a tendency to crystallise. Therefore, these complexes were not studied further.

Figure 2.1 The spin coating process

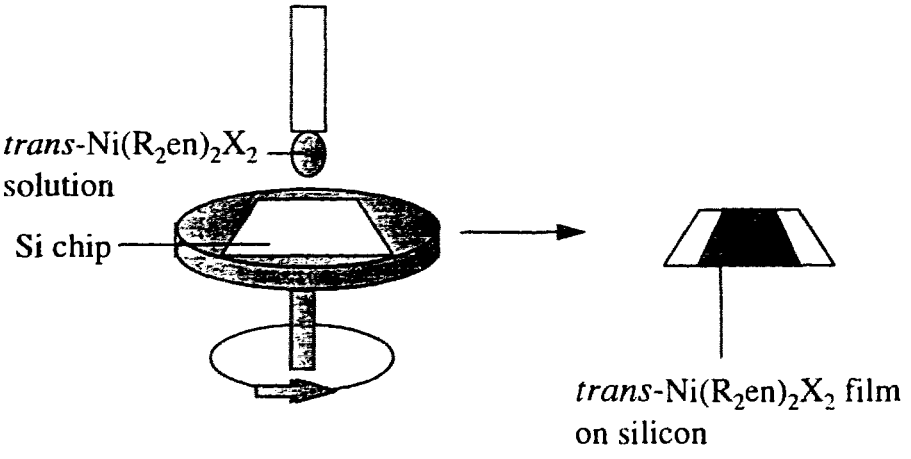

The films were spin-coated from saturated solutions of the complexes in CH_2Cl_2. The complexes that were studied were, without exception, easily cast into films and showed little tendency to crystallise. Optical interferometry was used to determine that the film thickness achievable by this method ranged from 35 ± 15 to 275 ± 30 nm. Regardless of anion, the films were thicker with Ni(s-Me$_2$en)X$_2$ than with Ni(a-Et$_2$en)X$_2$. Film thickness associated with the complexes Ni(s-Me$_2$en)X$_2$ and Ni(a-Et$_2$en)X$_2$ decreased as X was changed from NCS to NO_2 to NO_3. It appears that this is a result of the solubility of the complexes. The greater the solubility of the complex in CH_2Cl_2, the thicker the resultant film.

2.2.2 Spectroscopic data for the complexes

The FTIR spectroscopic data for the complexes are presented in Table 2.1. Whenever possible, literature values of FTIR spectra for *trans*-$Ni(R_2en)_2X_2$ [52, 62] were included in this table for comparison. The FTIR spectra are consistent with the literature values. The nitrite ligands in *trans*-$Ni(s\text{-}Me_2en)_2(ONO)_2$ and the related complex *trans*-$Ni(a\text{-}Et_2en)_2(ONO)_2$ are bound through the oxygen as nitrito ligands [63]. Nitrito (-ONO) coordination is indicated by an increase in ν_a and a decrease in ν_s frequencies from the free NO_2^- ion at 1250 and 1335 cm^{-1} respectively [64]. The antisymmetric and symmetric stretches of the nitrite were reported in the literature at 1337 and 1205 cm^{-1} respectively for *trans*-$Ni(s\text{-}Et_2en)_2(ONO)_2$ [65]. These absorptions were found at 1335 and 1215 cm^{-1} for *trans*-$Ni(s\text{-}Me_2en)_2(ONO)_2$ as a thin film. The related complex, *trans*-$Ni(a\text{-}Et_2en)_2(ONO)_2$ exhibited $\nu(NO_2)$ absorptions at 1365 and 1161 cm^{-1} consistent with literature values (1364 and 1161 cm^{-1}) for nitrito coordination (Table 2.1). The distinction that only one bonding mode is present is important in the case of the nitrite where evidence indicates that a nitro-nitrito equilibrium exists in solution for *trans*-$Ni(a\text{-}Et_2en)_2(ONO)_2$ [65].

Table 2.1 FTIR spectroscopic data and magnetic susceptibilities of the nickel complexes.

COMPLEX	Anion Bands (cm^{-1})	Literature (cm^{-1})	Assignment	μ_{eff} (B.M.)[c]
$Ni(s\text{-}Me_2en)_2(ONO)_2$	1335 1215		$\nu_a(NO_2)$ $\nu_s(NO_2)$	2.97
$Ni(a\text{-}Et_2en)_2(ONO)_2$	1365 1161 825	1364 1161 824[a] [52]	$\nu_a(NO_2)$ $\nu_s(NO_2)$ $\delta(NO_2)$	3.20 [52]
$[NO_2]^-$		1250 1335	$\nu_a(NO_2)$ $\nu_s(NO_2)$	
$Ni(s\text{-}Me_2en)_2(NO_3)_2$	1379 1337 806 613		$\nu_a(NO_2)$ $\nu_s(NO_2)$ $\delta(NO_2)$	3.21
$[Ni(s\text{-}Me_2en)_2(NO_3)]^+$	1447 1208		$\nu(NO)$ $\nu_s(NO_2)$	
$[NO_3]^-$	1367 1334	1368[a] [71]	$\nu_a(NO_2)$ $\nu_s(NO_2)$	
$Ni(a\text{-}Et_2en)_2(NO_3)_2$	1470 1386 1336 827 613		 $\nu_a(NO_2)$ $\nu_s(NO_2)$ $\delta(NO_2)$	diamagnetic [52]
$Ni(s\text{-}Me_2en)_2(NCS)_2$	2081	2090[b] [62]	$\nu(CN)$	3.03
$[Ni(s\text{-}Me_2en)_2(NCS)]^+$	2083		$\nu(CN)$	
$[NCS]^-$	2054		$\nu(CN)$	
$Ni(a\text{-}Et_2en)_2(NCS)_2$	2093	2092[a] [52]	$\nu(CN)$	3.20 [52]
$Ni(a\text{-}Et_2en)(NCS)_2$		2125 2096 2077[a] [52]	$\nu(CN)$	

[a] Nujol mull [b] KBr pellet [c] room temperature values

Spectroscopic evidence for the NCS compounds indicates that coordination is through the nitrogen. This conclusion was based on the ν(CN) positions for isothiocyanate (-NCS) complexes (ca. 2050 to 2100 cm^{-1}). The ν(CN) absorption bands for *trans*-$NiL_2(NCS)_2$ are found at 2081 cm^{-1} for L= s-Me_2en and 2093 cm^{-1} for L= a-Et_2en. The literature values of ν(CN) for *trans*-Ni(s-Me_2en)$_2$(NCS)$_2$ and *trans*-Ni(a-Et_2en)$_2$(NCS)$_2$ are 2090 cm^{-1} [52] and 2092 cm^{-1} [62] respectively. This mode of coordination has also been indicated in a single-crystal diffraction study of *trans*-Ni(s-Me_2en)$_2$(NCS)$_2$ [62].

The FTIR spectra for the nitrate complexes are summarised in Table 2.1. The weak coordination of NO_3^- in the axial positions is sufficient to split the absorption band for free NO_3^- at 1368 cm^{-1} into $\nu_a(NO_2)$ and $\nu_s(NO_2)$ bands at 1379 and 1337 cm^{-1} for *trans*-Ni(s-Me_2en)$_2$(NO_3)$_2$ and 1386 and 1336 cm^{-1} for *trans*-Ni(a-Et_2en)$_2$(NO_3)$_2$. The small splitting is consistent with the weak interaction of the NO_3 ligand with the Ni in these systems. It is also consistent with monodentate coordination of NO_3 *via* the oxygen as reported for the *trans* s-Me_2en complex [66].

The magnetic susceptibilities of the complexes are included in Table 2.1. All measurements were made at room temperature. The complex *trans*-Ni(a-Et_2en)$_2$(NO_3)$_2$ has a magnetic moment of zero indicating that it has no unpaired electrons. This complex has a significant tetragonal distortion reducing the energy of the lowest singlet state with respect to the lowest triplet state, which results in a singlet ground state for the molecule. The s-Me_2en ligands in *trans*-Ni(s-Me_2en)$_2$(NO_3)$_2$ have a smaller steric effect than the a-Et_2en, and the ligand field of the axial NO_3^- is sufficient to limit the tetragonal distortion

and a triplet ground state is obtained [53]. The effective magnetic moment, μ_{eff}, for Ni(s-$Me_2en)_2(NO_3)_2$ is 3.18 B.M., indicating that the complex has two unpaired electrons (triplet ground state), by the relationship $\mu_{eff} = \sqrt{n(n+2)}$ B. M. In all cases except *trans*-$Ni(a\text{-}Et_2en)_2(NO_3)_2$, the complexes have effective magnetic moments (Table 2.1) indicative of two unpaired electrons [52, 66].

The magnetic moment of *trans*-$Ni(a\text{-}Et_2en)_2(NO_3)_2$, indicates that the complex is diamagnetic. Therefore it has a singlet ground state, which is consistent with a weak axial field and large tetragonal distortion. Solutions of tetragonal complexes with labile metal-anion bonds exhibit solvation equilibria. The electrolytic conductance value for a 10^{-3} M solution of *trans*-$Ni(a\text{-}Et_2en)_2(NO_3)_2$ in $PhNO_2$ is 8.0 mhos and increases with increasing coordinating power of the solvent when changed to $MeNO_2$ (75.6 mhos) and MeCN (179 mhos) [52]. The expected conductivity value, if the NO_3^- were dissociated from the nickel in $PhNO_2$ solution, is in the range from 20 to 60 mhos, such as *trans*-$[Ni(a\text{-}Et_2en)_2][BPh_4]_2$ which has a Λ_m of 46.4 mhos (10^{-3} M)[52]. The paramagnetic complexes have conductance values approximately 2 mhos (10^{-3} M), indicating that they are non-electrolytes. The molar conductivity value of 8.0 mhos for *trans*-$Ni(a\text{-}Et_2en)_2(NO_3)_2$ indicates that it is an intermediate electrolyte, therefore the NO_3^- in the complex is coordinated to the nickel. Thus the complex is better represented as $[Ni(a\text{-}Et_2en)_2(NO_3)_2]$ with labile metal-NO_3 bonds rather than $[Ni(a\text{-}Et_2en)_2][NO_3]_2$ [52]. In an amorphous film, the complex would be in a non-coordinating environment, therefore the NO_3 is expected to be coordinated to the nickel.

The electronic absorption spectra for the complexes are summarised in Table 2.2.

The complex *trans*-Ni(s-Me_2en)$_2$(ONO)$_2$ in CH_2Cl_2 solution exhibits d-d absorptions at 1010, 840 and 500 nm and a d-d absorption that is obscured by CT transitions at 324 nm. The spectrum obtained for a thin film of the complex exhibited a d-d absorption band at 500 nm, a d-d and CT absorption at 324 nm and a CT absorption at 238 nm. Unfortunately, the films were not sufficiently absorptive to observe the low energy d-d transitions in typical thin films. However, measurements of the charge-transfer transitions in the film were consistent with the observed energies in dichloromethane solvent. All of the complexes have visible absorption bands associated with d-d transitions [52, 53, 62, 66]. As expected for triplet ground state molecules, weak absorptions in the region 1000 - 1200 nm are observed as the lowest energy d-d transitions. At higher energy, particularly in the UV region, more intense charge transfer transitions dominate. These are associated with charge transfer from the anionic ligand to the metal.

Table 2.2 Electronic absorption data for complexes of the formula NiL_4X_2.

Complex	λ (nm) thin film	λ (nm) solution[a]	λ (nm) solid (lit.)	λ (nm) solution (lit.)	Assign ment
$Ni(s\text{-}Me_2en)_2(ONO)_2$		1010			d-d
		840			d-d
	500	500			d-d
	324	324[a]			d-d, CT
	238				CT
$Ni(a\text{-}Me_2en)_2(ONO)_2$			1144		d-d
			913	930	d-d
			578	580	d-d
			367[b] [53]	492[c] [53]	d-d, CT
$Ni(a\text{-}Et_2en)_2(ONO)_2$	664sh		676	1020	d-d
	604	584	592	587[a] [52]	d-d
	352	352	490[b] [52]		d-d, CT
	248				CT
$Ni(s\text{-}Me_2en)_2(NO_3)_2$		1130	1193		d-d
		860	748		d-d
	572	570	563[a] [66]		d-d
	358	358			d-d, CT
	234				CT
$Ni(a\text{-}Et_2en)_2(NO_3)_2$	588	570	467[e] [52]		d-d
	370	370			d-d, CT
	254sh				CT
	234				CT
$Ni(s\text{-}Me_2en)_2(NCS)_2$		1130	545		d-d
		870	345[e] [62]		d-d
	558	560			d-d
	356	356			d-d, CT
	276	276			CT
	230				CT
$Ni(a\text{-}Et_2en)_2(NCS)_2$		1160		1100sh	d-d
		840	667	909	d-d
	558	560	572	582	d-d
	366	366	363[b] [52]	364[c] [52]	d-d, CT
	282sh	282			CT
	240				CT

[a] CH_2Cl_2 solvent [b] solid, reflectance [c] $CHCl_3$ solvent [d] Nujol mull [e] C_4Cl_6 mull

At this point, it is worth noting that the irradiation source for the following studies was the Pyrex and water filtered output of a high pressure mercury lamp. Given the weak

absorption of the films in the d-d region it was not practical to undertake single-wavelength photolysis in the visible region. This was confirmed by exploratory photolysis of the complexes overnight with visible light irradiation of the d-d transitions. No significant photoreaction was induced on this timescale for any of the complexes used in this study. Hence, the photolysis experiments were conducted using both the UV and visible output (λ>320 nm) of the Hg lamp thus resulting in the excitation of primarily the lowest energy charge transfer transitions.

2.2.3 Photochemistry of the complexes on silicon surfaces

A thin film prepared from *trans*-Ni(s-Me_2en)$_2$(ONO)$_2$ was stable in the dark, under vacuum. Upon photolysis of the film in vacuum, the FTIR absorption bands associated with the complex at 1335 and 1215 cm^{-1} decreased in intensity and no new infrared absorptions were observed. The decay of the absorption bands was extremely slow and the photolysis time required to reach half the initial intensity was approximately 5 hours using a Pyrex and water filtered output of the mercury lamp (λ> 320 nm). The absorptions due to the nitrite and diamine ligand were lost and no new absorptions associated with the free ligands were observed. This is indicative of loss of ligands to the atmosphere. This result was also observed for a sample photolysed in an air atmosphere. The a-Et_2en analogue reacted in a similar manner.

It is worth noting that both Ni(R_2en)(NO_2)$_2$ (R $\equiv$ H, a-Et) are known, stable complexes and that the latter may be prepared thermally from *trans*-Ni(Et_2en)$_2$(ONO)$_2$

[67]. If $Ni(R_2en)(NO_2)_2$ (R ≡ s-Me, a-Et) were the primary photoproduct, it should be detectable by FTIR spectroscopy. The loss of NO_2^- would generate the complex $[Ni(R_2en)_2(NO_2)][NO_2]$. The complexes $[Ni(R_2en)_2(NO_2)][X]$ (R_2en= s-Et_2en, a-Me_2en, s-Me_2en, X= ClO_4, BF_4 [68]; R_2en= H_2en, X= NO_3 [69], BF_4 [70]), are all known to be stable. If NO_2^- loss has been induced, the primary photoproduct would have been stable and detectable by FTIR spectroscopy. No products were observed that would be consistent with either diamine or nitrite loss, therefore these reaction pathways may be ruled out as the primary photoprocess. The initial photoreaction appears to be loss of an NO_2 radical to generate an unstable Ni (I) species. This unstable compound then decomposes to generate nickel metal and free ligand as outlined in equation 2.1:

$$\begin{aligned} &\textit{trans}\text{-}Ni(R_2en)_2(ONO)_2 \xrightarrow{h\nu} \\ &\quad [\textit{trans}\text{-}Ni(R_2en)_2(ONO) + NO_2] \xrightarrow{\Delta} \\ &\quad\quad Ni + 2\,NO_2 + 2\,R_2en \end{aligned} \qquad (2.1)$$

R = s-Me, a-Et

Films composed of the isothiocyanate complexes were also photosensitive under the same irradiation conditions. The photochemistry of the isothiocyanate complexes was dependent on the nature of the diamine ligand. The spectroscopic study of the photochemistry of *trans*-Ni(s-Me_2en)$_2$(NCS)$_2$ was most informative and will be described first. Irradiation of films of *trans*-Ni(s-Me_2en)$_2$(NCS)$_2$ with UV light resulted in the spectroscopic changes illustrated in Figure 2.2. The absorption band of the isothiocyanato ligand of the starting complex decayed rapidly in the initial stages of the

reaction. This initial rapid decay is evidenced by a decay in intensity of the isothiocyanato absorption at 2081 cm^{-1} to approximately 75 % of its initial intensity. During this process a shoulder at 2054 cm^{-1} becomes evident and the central, and the still most intense, absorption band shifts slightly to 2083 cm^{-1}. During this initial process an isosbestic point is observed at 2060 cm^{-1}. This partial decay is presumably due to the formation of a photoproduct which is much more photostable than the starting material. Evidence for this comes from a plot of ln $[(A_o - A_f) / (A_t - A_f)]$ *vs.* irradiation time , shown in Figure 2.3. This plot is linear for the initial stages of the reaction, with the choice of A_f of 0.081 (*i.e.* the first 60 min, or A_f= 58 % of A_o). This indicates an intermediate with an absorbance coincident with that of the starting material [43].

Figure 2.2 FTIR spectral changes associated with photolysis of *trans*-$Ni(s\text{-}Me_2en)_2(NCS)_2$ in a surface film.

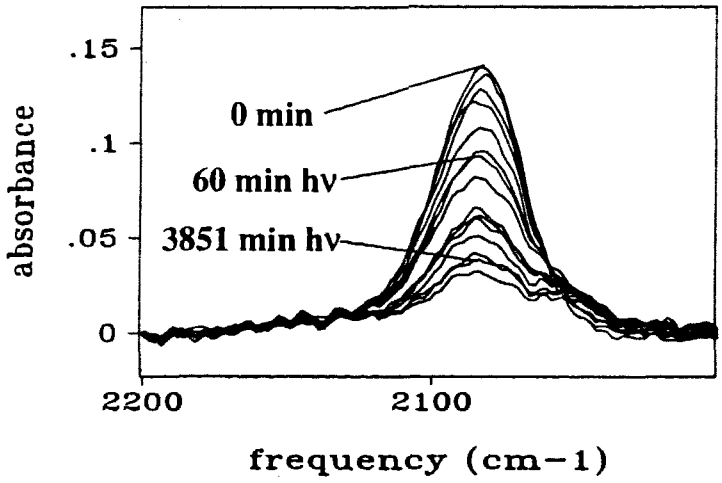

Figure 2.3 A plot of the observed points and best fit line in a plot of $\ln([A_o-A_f]/[A_t-A_f])$ *vs.* irradiation time for the initial photoreaction for a film of *trans*-Ni(s-Me_2en)$_2$(NCS)$_2$ (data from Fig. 2.2). The best fit line was obtained with a value $A_f = 0.081$ (58% A_o).

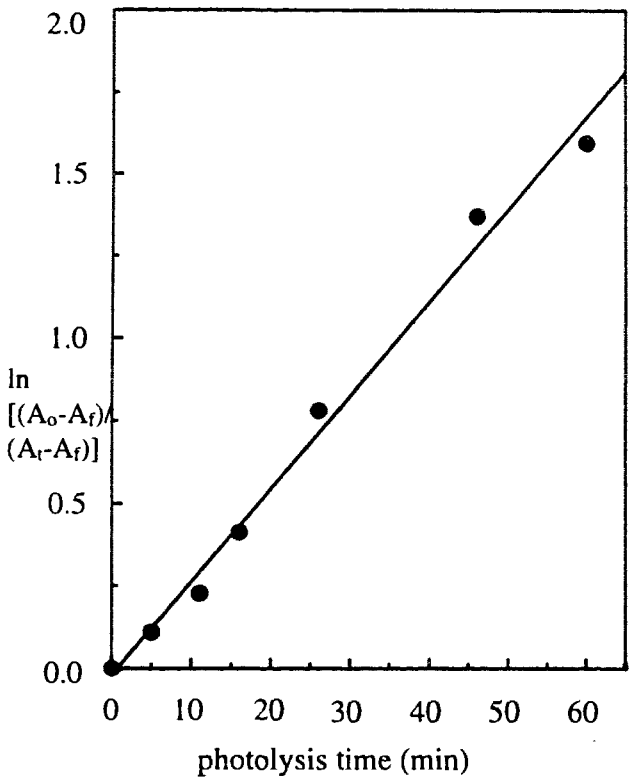

The above results are consistent with photochemical loss of NCS^-, to generate the ion pair [Ni(s-Me_2en)$_2$(NCS)][NCS] as shown in equation 2.2. The IR spectrum of the known K[NCS] with ν(CN) at 2053 cm^{-1} is consistent with the observation of an absorption band at 2054 cm^{-1} observed in the solid state photochemical reaction. The remaining band at 2083 cm^{-1} is consistent with formation of the ionic, five-coordinate complex, [Ni(s-Me_2en)$_2$(NCS)]$^+$. If the complex possessed NCS bridges a six-coordinate environment would result and more than one IR absorption band for the complex would

be observed in the ν(CN) region. Bridging NCS ligands have been identified previously in related Ni(II) complexes [52]. No evidence for bridging isothiocyanate ligands was observed, hence the photoreaction observed is consistent with eq. 2.2.

$$\textit{trans}\text{-Ni(s-Me}_2\text{en)}_2\text{(NCS)}_2 \xrightarrow{h\nu} [\text{Ni(s-Me}_2\text{en)}_2\text{(NCS)}][\text{NCS}] \qquad (2.2)$$

This ionic complex, $[\text{Ni(s-Me}_2\text{en)}_2\text{(NCS)}]^+$, is itself photosensitive, decaying with a normal exponential decay. Under the same irradiation conditions, the photolysis time required for the FTIR absorption to reach half the initial intensity was 60 hours, as demonstrated by the linear plot of $\ln[A_t / 0.081]$ *vs.* photolysis time illustrated in Figure 2.4. This decay may be a result of initial photochemical loss of the NCS as a radical or possibly the diamine ligand. Presumably, it is the isothiocyanate ligand which is lost as a radical to form a Ni (I) species which then decomposes in a reaction which involves an electron transfer with the NCS^- ligand produced in equation 2.2.

Figure 2.4 A plot of the observed points and best fit line in a plot of $\ln([A_o]/[A_t])$ *vs.* irradiation time for the final photoreaction of a film of [Ni(s-Me_2en)$_2$(NCS)][NCS] produced by photolysis of *trans*-Ni(s-Me_2en)$_2$(NCS)$_2$ in a surface film (data from Fig. 2.2). The best fit line was obtained with a value $A_o = 0.081$.

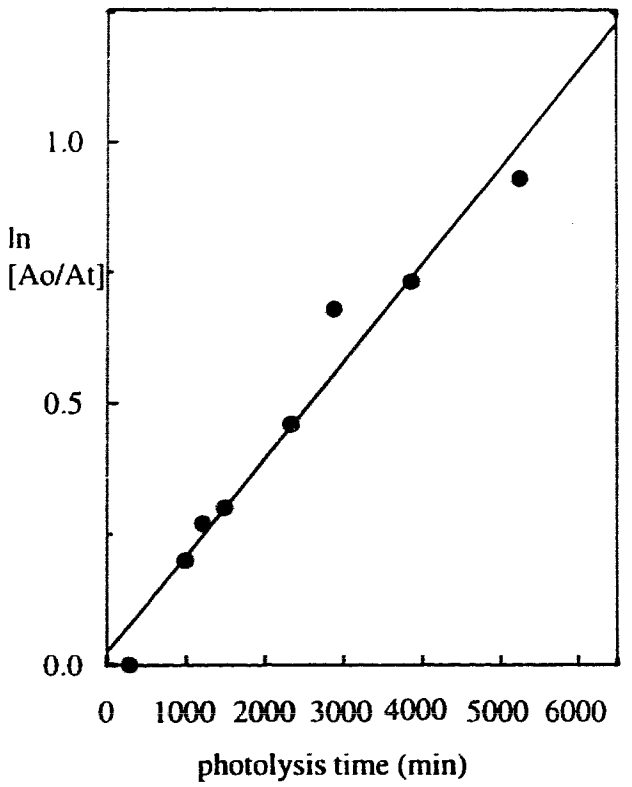

The broad band irradiation of films formed from Ni(a-Et_2en)$_2$(NCS)$_2$ resulted in a photoreaction as evidenced by changes in the FTIR spectrum. The intense absorption band, associated with the anionic ligand at 2093 cm^{-1}, decays steadily as a result of irradiation. No new absorption bands which may be associated with the formation of an intermediate are observed throughout this process. This result is most consistent with the loss of the isothiocyanate ligand as a radical.

If irradiation of $Ni(a\text{-}Et_2en)_2(NCS)_2$ led to the loss of a diamine ligand, this would yield the complex $Ni(a\text{-}Et_2en)(NCS)_2$. This complex has been prepared previously and is known to be stable [52]. If this product had been produced, it should have been observed spectroscopically. Another possibility would be the loss of the isothiocyanate ion. This would also have resulted in spectroscopically detectable products. The remaining alternative, the photoinduced loss of the NCS radical, is consistent with the data. This reaction would lead to the production of an unstable Ni (I) species which would thermalise rapidly yielding nickel metal, a second NCS radical, and free diamine. The overall process is shown in equation 2.3.

$$\begin{aligned} &\textit{trans}\text{-}Ni(a\text{-}Et_2en)_2(NCS)_2 \xrightarrow{h\nu} \\ &\quad Ni(a\text{-}Et_2en)_2(NCS) + NCS \xrightarrow{\Delta} \\ &\quad\quad Ni + 2\,NCS + 2\,a\text{-}Et_2en \end{aligned} \qquad (2.3)$$

As was found for the isothiocyanato complexes, the photochemistry of the two nitrato complexes was dependent on the diamine ligand. Irradiation of *trans*-$Ni(s\text{-}Me_2en)_2(NO_3)_2$ with UV light resulted in decay of the intense absorption bands associated with the coordinated NO_3 at 1379 and 1337 cm^{-1}. As these bands diminished in intensity to approximately 50% of the initial intensity, they underwent a slight shift to lower energy with final positions of 1367 and 1334 cm^{-1}. During this process the concomitant production of two new absorptions at 1447 and 1208 cm^{-1} was apparent. Upon irradiation, the photolysis time required for the FTIR absorptions at 1379 and 1337 cm^{-1} to reach half the initial intensity was 2 hours. Plots similar to those constructed for the

isothiocyanato complexes were made and confirm the presence of absorption bands overlapping with those of the starting material. These spectroscopic changes are consistent with the formation of ionic NO_3^- which has a $\nu_a(NO_2)$ absorption band at 1368 cm^{-1} [71], as evidenced by the formation of an ion pair with absorptions at 1367 and 1334 cm^{-1} and bidentate NO_3^- with associated absorptions at 1447 and 1208 cm^{-1}. This process is shown in equation 2.4. This reaction is the reverse of the thermal reaction of the *cis* ion pair to the *trans* coordinated complex which has been reported previously [66].

$$\textit{trans}\text{-Ni(s-Me}_2\text{en)}_2(NO_3)_2 \xrightarrow{h\nu} \textit{cis}\text{-[Ni(s-Me}_2\text{en)}_2(NO_3)][NO_3] \qquad (2.4)$$

The ionic product, *cis*-[Ni(s-Me_2en)$_2$(NO_3)][NO_3], decays much less efficiently under irradiation. Under identical irradiation conditions as above for *trans*-Ni(s-Me_2en)$_2$(NO_3)$_2$, the FTIR absorptions associated with the *cis* ion pair decay to half the initial intensity in nearly 36 hours. Prolonged photolysis results in the loss of absorption intensity associated with the *cis* ionic product and the production of nickel films. This is consistent with a charge transfer transition, most likely from the coordinated NO_3^- to the metal. This would be expected to result in the production of an unstable Ni(I) species followed by loss of all ligands.

Irradiation of the a-Et_2en analogue, *trans*-Ni(a-Et_2en)$_2$(NO_3)$_2$ resulted in loss of the FTIR absorption bands associated with the anionic ligand at 1386 and 1336 cm^{-1}. During this process no new absorption bands attributable to intermediates were observed. The complex appeared to lose all ligands. The decay of absorption intensity occurred slowly on photolysis, reaching half the initial intensity in 5 days.

Loss of coordination of the nitrato ligand as a result of photolysis would be expected to lead to an ion-pair such as *cis*-[Ni(a-Et_2en)$_2$(NO_3)][NO_3] analogous to equation 2.4. Similar species such as [Ni(en)$_2$(NO_3)][X] (X= ClO_4^-, BF_4^-) [71] as well as *cis*-[Ni(s-Me_2en)$_2$(NO_3)][NO_3] [66] are known, thermally stable complexes. Loss of coordination of one a-Et_2en ligand would lead to a species related to the known stable Ni(R_2en)(NO_3)$_2$ which contains both terminal and chelating nitrate groups. In contrast, loss of NO_3 as a radical would not be expected to generate thermally stable molecular products and is consistent with the observed results. This reaction sequence is shown in equation 2.5.

$$\textit{trans}\text{-Ni(a-Et}_2\text{en)}_2(NO_3)_2 \xrightarrow{h\nu}$$

$$[\text{Ni(a-Et}_2\text{en)}_2(NO_3) + NO_3] \xrightarrow{\Delta} \qquad (2.5)$$

$$\text{Ni} + 2\,NO_3 + 2\,\text{a-Et}_2\text{en}$$

2.3 Discussion

These experiments demonstrate that the loss of NO_2, NO_3, NCS, a-Et_2en and s-Me_2en may be initiated photochemically in the solid state. In each case, the photolysis of *trans*-Ni$(R_2en)_2(X)_2$ (X= NO_2, NO_3, NCS) led to loss of the axial ligand as either X• or X^- according to equations 2.6 or 2.7. Both of these reactions are consistent with being induced *via* the high energy LMCT transitions irradiated. The low quantum yields for all reactions precluded a study with monochromatic light.

$$\textit{trans}\text{-Ni}(R_2en)_2(X)_2 \xrightarrow{h\nu} [Ni(R_2en)_2(X)][X] \qquad (2.6)$$

R= s-Me, X= NCS, NO_3

$$\textit{trans}\text{-Ni}(R_2en)_2(X)_2 \xrightarrow{h\nu} [Ni(R_2en)_2(X) + X\bullet] \qquad (2.7)$$

R= s-Me, a-Et, X= NO_2

R= a-Et, X= NCS, NO_3

All of the molecules studied here, with the exception of *trans*-Ni(a-Et_2en)$_2(NO_3)_2$, are triplet ground state molecules. Figure 2.5 illustrates the orbital occupation of the a) triplet and b) singlet ground state molecules studied. The molecules in the ground state are treated as C_{4v} rather than D_{4h} to maintain the same symmetry along the reaction coordinate. First, the excited states of the triplet ground state molecules will be given. The lowest energy triplet transition is expected to be $^3B_1 \rightarrow {}^3A_2$ in C_{4v} symmetry. It is important to note at this point that the molecule is arranged in the Cartesian coordinates such that the *z*-axis is the unique axis with the weak field ligands on this axis. This

arrangement leads to a situation in which the $d_{x^2-y^2}$ orbital is of higher energy than the d_{z^2} orbital. The configuration is consistent with $(a_1^1 b_1^1)$ for the ground state and $(b_2^1 b_1^1)$ for the lowest energy triplet excited state. In terms of orbitals this is shown in Figure 2.5 a) and 2.6 a) respectively. If the lowest energy triplet d-d transition provides the reactive state for ligand loss, the anionic ligand would be ejected as an anion, X^- consistent with Figure 2.6 b).

Figure 2.5 Occupation of the metal d-orbitals in the a) triplet ground state and the b) singlet ground state.

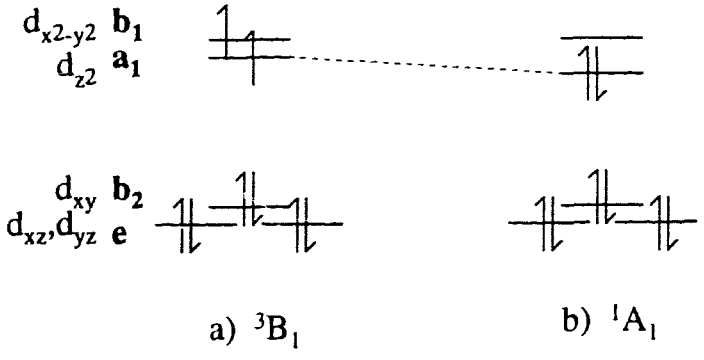

Figure 2.6 Orbital occupation associated with a) the lowest energy triplet d-d transition resulting in b) anion loss as X^-, and c) the lowest energy LMCT transition resulting in d) radical loss as $X^{\bullet}$.

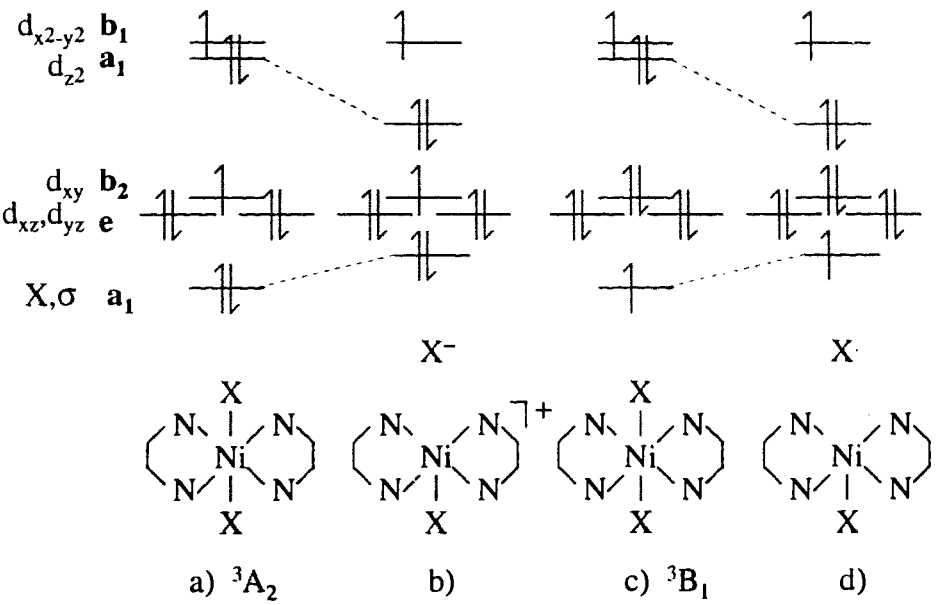

One of the lowest energy LMCT transitions is expected to be $^3B_1 \rightarrow {}^3B_1$ which represents a configuration consistent with $(a_1^1 b_1^1)$ for the ground state and $(a_1^1 b_1^1)$ for the excited state. The respective orbital configurations corresponding to these states are shown in Figure 2.5 a) and 2.6 c). The transition corresponds to charge transfer of an electron from the sigma orbital of an anionic ligand to the metal d_{z^2} antibonding orbital. Elongation of the M-X bond as a result of excitation would lead to loss of the anionic ligand as a radical, consistent with Figure 2.6 d). It should be noted that the same reactivity is expected if the LMCT transition originates from a pi orbital of the anionic ligand to the Ni d_{z^2} antibonding orbital.

The excited state is expected to have a greater repulsion along the *z*-axis and

hence labilization along this axis is expected for the lowest energy d-d triplet excited state (Fig. 2.6 a)). The lowest energy LMCT transition would also be expected to populate the d_{z^2} orbital as in Fig. 2.6 c). This excited state would also be expected to result in the loss of an axial ligand. Since it is common for internal conversion to be fast, it would not be exceptional for the reactive states to be either the thermally populated lowest energy triplet LF (d-d) or LMCT state as a result of LMCT excitation. It is interesting to consider the possibility that d-d excited states lead to loss of the anionic ligand as the anion (eq. 2.6) whereas the LMCT excited states result in loss of the anionic ligand as a radical (eq. 2.7). The orbital configurations consistent with this reactivity are shown in Figure 2.6. Occupation of the d_{z^2} orbital causes greater repulsion along this axis. Elongation of the axial M-X bond lowers the energy of the d_{z^2} orbital sufficiently to make loss of the anionic ligand favourable. In the case of a reactive d-d excited state, ligand loss would occur with both electrons on the X, hence , as the anion (Figure 2.6 b)). For the reactive LMCT excited state, the ligand would be ejected with one electron in the sigma orbital of X, therefore, radical loss results (Figure 2.6 d)). In spite of this apparent agreement with our data, further work will be required to demonstrate whether this interpretation of the results is correct.

Well known reactivity studies of metal ions of other d^n configurations such as d^3 and d^6 metal ions have been investigated. These studies indicate that loss of the strong field ligand from the weak field axis is observed for the excited states of these ions [39, 40, 54]. The results of the study presented here, of triplet ground state d^8 molecules, are consistent with photochemical loss from the weak field axis.

The one example of a singlet ground state molecule considered in this study is *trans*-Ni(a-Et_2en)$_2$(NO_3)$_2$. The distortion along the *z*-axis for this molecule is larger than for the other complexes. Presumably, this is due to the steric effect of the bulkier a-Et_2en and NO_3 ligands. Thus, a lowering of the d_{z^2} orbital has occurred resulting in spin-pairing to yield double occupation of this orbital. The weak axial perturbation is insufficient to maintain a triplet state. In spite of this, conductivity measurements indicate that the axial ligands are indeed bound in solution and the formation of free ions is not favoured [52].

Photolysis of an amorphous film of *trans*-Ni(a-Et_2en)$_2$(NO_3)$_2$ resulted in loss of the NO_3 ligand as a radical as shown in equation 2.7. The effect of a LMCT transition may be the loss of a large component of the ionic interaction between metal and anionic ligand with concomitant formation of a neutral NO_3 radical. This is the expected result of an NO_3^- (σ) $\rightarrow$ Ni ($d_{x^2-y^2}$) LMCT transition. The loss of ionic bonding evidently results in ejection of the NO_3 ligand as a radical. The resultant Ni(I) complex would then undergo rapid thermal decomposition. This photoinduced electron transfer reaction shows little dependence on the excited state and more on redox reactivity.

The interpretation of the reactivity of *trans*-Ni(a-Et_2en)$_2$(NO_3)$_2$ is fundamentally different from that of the other complexes studied in this chapter. The occupation of an antibonding orbital could be correlated with the expulsion of ligands from the unique axis for the photoreactions of *trans*-(R_2en)$_2$$NiX_2$ (R= s-Me, X= NO_2, NO_3, NCS; R= a-Et, X= NO_2, NCS). In the case of the photochemistry of *trans*-(a-Et_2en)$_2$(NO_3)$_2$, redox reactivity indicates the loss of NO_3 even though occupation of the $d_{x^2-y^2}$ orbital may be expected to labilize ligands in the equatorial positions. This outlines the difference between the

excited states of the singlet and triplet ground state molecules.

2.4 Conclusions

The use of solid state photochemistry to yield an environment in which normally labile complexes may be studied has been demonstrated. The results of this study demonstrate that the loss of ligands from the weak field axis of d^8 metal ions occurs in the excited state. Amorphous films of *trans*-NiL_2X_2 (L= a-Et_2en, s-Me_2en, X= NO_2, NCS, NO_3) photoejected X as either the anion or as the radical *via* LMCT excitation. This initial result indicates that solid state photochemistry may be used to study in detail photochemical reactions of complexes which are labile in solution.

2.5 Experimental details

2.5.1 Instruments and materials

The silicon wafers were obtained from Shin Etsu and were p-type Si(100). The wafers were cut to approximately 10 mm x 15 mm in our laboratory. The CaF_2 and NaCl crystals were obtained from Wilmad Glass Co. Inc.

FTIR spectra were obtained with 4 cm^{-1} resolution using a Bomem MB-120 spectrometer on samples held in an aluminum vacuum chamber by steel clips. The substrates used to obtain the spectra were silicon or CaF_2. The chamber was equipped with NaCl or CaF_2 optics. A 100 W Hg lamp in an Oriel housing equipped with condenser lenses was used as the irradiation source. This light was filtered through a 10

cm water filter with quartz optics. Film thickness was determined using a Leitz Laborlux 12 ME S optical microscope with an interference attachment. Magnetic susceptibility measurements were made using a Johnson Matthey magnetic susceptibility balance.

2.5.2 Preparation of the complexes

All the complexes used in this study were prepared by literature procedures [52, 53, 62, 66, 71] and characterised by elemental analysis (Table 2.3), Fourier transform infrared (FTIR) spectroscopy as well as magnetic susceptibility. Complexes with the ligand s-Me_2en ($MeHNC_2H_4NMeH$) were prepared following the procedure for the a-Et_2en ($Et_2NC_2H_4NH_2$) analogues.

Table 2.3 Elemental analysis for complexes of the formula NiL_4X_2 (L_2 = a-Et_2en, s-Me_2en, X= NO_2, NO_3, NCS).

Complex	%C found (calcd)	% H found (calcd)	%N found (calcd)
(s-Me_2en)$_2$Ni(NO_2)$_2$	29.11 (29.38)	7.34 (7.40)	25.79 (25.70)
(s-Me_2en)$_2$Ni(NCS)$_2$	34.50 (34.20)	6.99 (6.89)	23.70 (23.94)
(s-Me_2en)$_2$Ni(NO_3)$_2$	27.01 (26.76)	6.93 (6.74)	23.01 (23.41)
(a-Et_2en)$_2$Ni(NO_2)$_2$	37.72 (37.62)	8.39 (8.42)	21.69 (21.94)
(a-Et_2en)$_2$Ni(NCS)$_2$	(41.29)	(7.29)	(20.64)
(a-Et_2en)$_2$Ni(NO_3)$_2$	37.72 (37.62)	8.39 (8.42)	21.69 (21.94)

2.5.3 Preparation of the amorphous thin films

Thin films of the precursor complexes were prepared from solutions of the complexes in CH_2Cl_2. A silicon chip was placed on a Laurell Technology Corp. spin

coater and rotated at a speed of 1000 rev min^{-1}. A drop of a solution of *trans*-Ni(a-$Et_2en)_2(NCS)_2$ in CH_2Cl_2 was dispensed from a disposable pipette onto the spinning silicon chip. The solution was allowed to spread and the solvent to evaporate. At this point, the motor was turned off and a thin film of the complex remained on the chip.

2.5.4 Photolysis of complexes as thin films on silicon substrates

All the films prepared by this method are thin enough that the complexes are absorbing only a small portion of the irradiation beam, allowing complete penetration of the light. Typically, the absorption of the complexes was a maximum of 0.1 in the region 200 - 240 nm. Under these conditions the amount of light absorbed by the complexes is linearly related to the coverage of the complexes on the surface. Thus, the concentration of the absorbing species should decay exponentially with photolysis time for a unimolecular photochemical reaction.

All photolysis experiments were done following the same procedure. A typical experiment is as follows. A silicon surface was coated with an amorphous film of *trans*-Ni(s-$Me_2en)_2(NCS)_2$ as described in Section 2.2.1 and was transferred to the vacuum chamber. The chamber was then placed under vacuum and an FTIR spectrum was obtained. The sample was irradiated for 5 minutes and another spectrum was obtained. This process was repeated for the following accumulated photolysis times: 11, 16, 26, 46, 60, 280, 980, 1200, 1476, 2326, 2866, 3851 and 5246 minutes. Control experiments were performed by monitoring the decomposition reaction of an amorphous precursor film in the dark.

Chapter 3

Solid State Photochemistry of Thin Amorphous Films of Trigonal Bipyramidal $Fe(CO)_4PPh_3$

3.1 Introduction

In this chapter, the photochemistry of amorphous films of $Fe(CO)_4PPh_3$ will be presented. The main objective was to investigate the mechanism of photodecomposition of thin films of $Fe(CO)_4PPh_3$. Another objective was to manipulate the decomposition by substitution of the ejected ligands in the amorphous solid state.

The molecule $Fe(CO)_4PPh_3$ was chosen as the precursor for the study of both photodecomposition and substitution reactions. This complex was selected due to the fact that the primary photochemical reactions of $Fe(CO)_5$ and its derivatives are well known. Many derivatives of $Fe(CO)_5$ are identifiable in the FTIR region. The photochemistry of $Fe(CO)_5$ and its substituted derivatives have been examined previously in the gas phase [72], in solution [73, 74], in glasses [75], as matrices [76, 77] and bound to both polymers [78] and surfaces [79]. Precedent suggests that loss of CO, according to equation 3.1, is the dominant primary photoprocess for iron carbonyl complexes. This is the first report of its chemistry as an amorphous thin film. Reaction in the condensed phase may be expected to result in the formation of a variety of products resultant from the thermal chemistry of the $Fe(CO)_3PPh_3$ intermediate, including clusters with iron carbonyl phosphines [80, 81, 82].

$$Fe(CO)_4PPh_3 \xrightarrow{h\nu} Fe(CO)_3PPh_3 + CO \qquad (3.1)$$

In this study we have focused our attention on $Fe(CO)_4PPh_3$. The coordination of a large phosphine, PPh_3, renders the vapour pressure of the complex sufficiently low that evaporation of the starting material during the study is inconsequential. It should be noted that the PPh_3 ligand will have a negative impact on the purity of the photoproduced films. Triphenylphosphine, PPh_3, is bulky and has a low vapour pressure, therefore making it difficult to diffuse out of the film after it is ejected from the complex. However, our concern in this study is directed at investigation of the process rather than the purity of the photoproduced materials. A test for compatibility with current lithography techniques will also be presented.

3.2 Results

3.2.1 Spectroscopic data for the complexes

The FTIR spectra of the carbonyl region of $Fe(CO)_4PPh_3$, $Fe(CO)_3(PPh_3)_2$ and $Fe(CO)_2(PPh_3)_3$ are summarized in Table 3.1. The symmetry of $Fe(CO)_4PPh_3$ is C_{3v} with absorptions associated with the CO stretching modes ($2A_1$ and E). These absorption bands were found at 2048, 1973 and 1931 cm^{-1} respectively. These bands are consistent with the literature values for $Fe(CO)_4PPh_3$ in THF solution which are 2050, 1973 and 1940 cm^{-1} [80]. For $Fe(CO)_3(PPh_3)_2$, the *trans* isomer is expected to have only one absorption observed (E' in D_{3h} symmetry) while either a C_{2v} or a C_S structure would lead to three absorptions being IR active. From a single observed absorption at 1877 cm^{-1} we

can confirm the *trans* geometry of the phosphine ligands. The frequency reported here for *trans*-$Fe(CO)_3(PPh_3)_2$ is consistent with the spectrum reported in THF solution (1887 cm^{-1}) [80]. The literature values for the ν(CO) absorptions of $Fe(CO)_2(PPh_3)_3$ in nujol are 1894 and 1838 cm^{-1} (A_1 and B_1 respectively in C_{2v}) [83]. One absorption band at 1838 cm^{-1} with a very small intensity was observed in a film containing a mixture of $Fe(CO)_3(PPh_3)_2$ and $Fe(CO)_2(PPh_3)_3$. The absorption band expected at approximately 1900 cm^{-1} was too weak to observe and obscured by the noise. The similarity of the IR spectra of the $Fe(CO)_4PPh_3$, $Fe(CO)_3(PPh_3)_2$ and $Fe(CO)_2(PPh_3)_3$ films with the complexes in solution indicates that there are no strong intermolecular interactions in the thin amorphous films.

Table 3.1 Spectroscopic data for $Fe(CO)_4PPh_3$, $Fe(CO)_3(PPh_3)_2$, $Fe(CO)_2(PPh_3)_3$, PPh_3 and $CHPh_3$ on Si(111).

Complex	Energy, cm^{-1} (ε_{IR}, $Å^2molec^{-1}$)[a]	FTIR A/ mono-layer[a,b]	Assignment	Energy, nm (ε_{UV}, cm^2mol^{-1})	Assign-ment
$Fe(CO)_4PPh_3$	2048 (0.031)	0.00047	ν(CO) (A_1)	366 ($3.78x10^6$)	d-d
	1973 (0.022)	0.00034	ν(CO) (A_1)	268 ($34.4x10^6$)	CT
	1931 (0.073)	0.0011	ν(CO) (E)	232 ($99.3x10^6$)	CT
$Fe(CO)_3(PPh_3)_2$	1877 (0.094)	0.0010	ν(CO) (E)	436 ($1.12x10^6$)	d-d
				366 ($5.77x10^6$)	d-d
				348 ($7.69x10^6$)	d-d
				252 ($45.0x10^6$)	CT
				230 ($72.3x10^6$)	CT
$Fe(CO)_2(PPh_3)_3$	1894		ν(CO) (A_1)		
	1838 [83]		ν(CO) (B_1)		
PPh_3	1433 (0.029)	0.00058			
$CHPh_3$	1495 (0.0116)	0.00023			

[a] error approximately 10%, [b] calculated from ε_{IR}

A plot of the absorbance of the ν(CO) stretch at 1931 cm^{-1} for $Fe(CO)_4PPh_3$ and at 1877 cm^{-1} for *trans*-$Fe(CO)_3(PPh_3)_2$ *versus* coverage in molecules/$Å^2$ was found to be linear for the range of film thickness used in all experiments. The plots, shown in Figures 3.1 and 3.2, are linear indicating that the FTIR absorbance may be used as an indication of the amount of a species within the film in this absorbance range. Throughout this chapter, the FTIR absorbance will be used to monitor the extent of reaction in these systems. Similar plots were made for the molecules, PPh_3 and $HCPh_3$.

IR extinction coefficients were calculated from the slope of the plots of absorbance *vs.* molecules/$Å^2$ and are presented in Table 3.1. The extinction coefficient,

ε_{IR}, for the ν(CO) at 1931 cm^{-1} for $Fe(CO)_4PPh_3$ is 0.073 $Å^2$molecule^{-1}. The extinction coefficient, ε_{IR}, for the ν(CO) at 1877 cm^{-1} for $Fe(CO)_3(PPh_3)_2$ is 0.094 $Å^2$molecule^{-1}.

Figure 3.1 Plot of FTIR absorbance *vs.* coverage for $Fe(CO)_4PPh_3$.

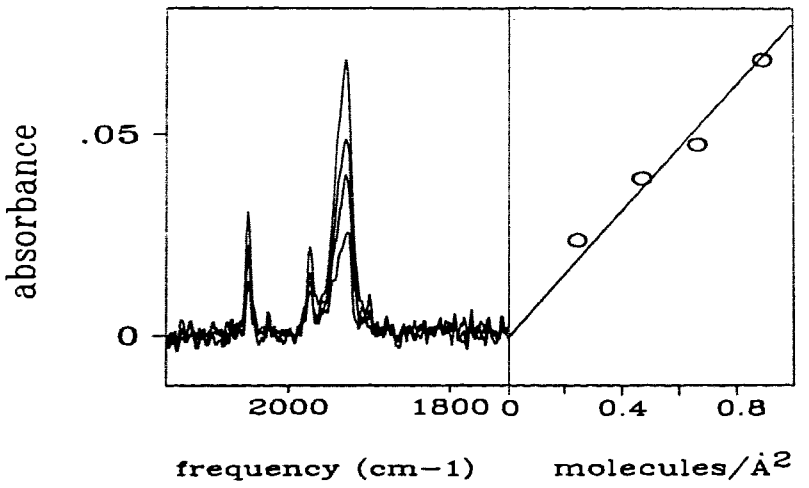

Figure 3.2 Plot of FTIR absorbance *vs.* coverage for *trans*-$Fe(CO)_3(PPh_3)_2$.

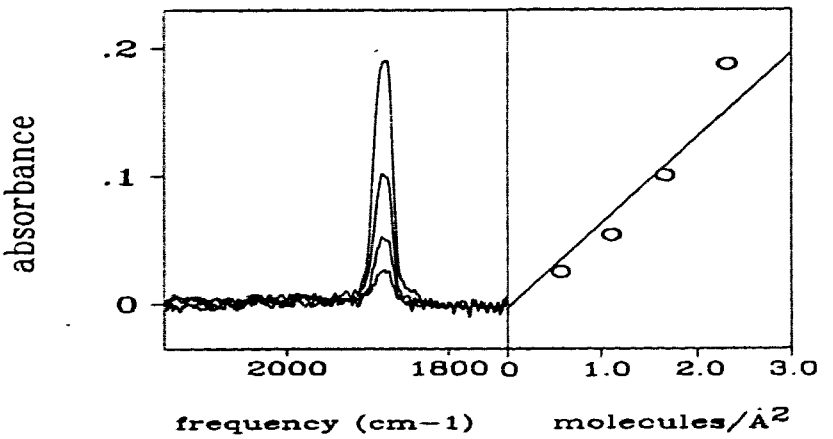

Electronic absorption spectra for amorphous films of the pure compounds were obtained and the results are summarized in Table 3.1. Absorption spectra of the films are comparable to the spectra obtained for these molecules in other media [75]. The molar extinction coefficient for an electronic transition, ε_{UV}, of a complex as a film was calculated. The calculation used is the ratio of UV absorbance (at a specific wavelength) to FTIR absorbance (at a specific frequency) of a film, times the extinction coefficient, ε_{IR} (cm^2mol^{-1}) at the FTIR frequency used. Optical quality spin coated films were used for the determination of the extinction coefficients for electronic transitions. A direct calibration by electronic absorption spectroscopy is precluded by problems associated with light scattering. Light scattering is a function of wavelength. Poor quality films scatter UV light more than infrared light. The extinction coefficient for $Fe(CO)_4PPh_3$ at 366 nm is 3.78 x 10^6 cm^2mol^{-1}. The extinction coefficient for *trans*-$Fe(CO)_3(PPh_3)_2$ at 366 nm is 5.77 x 10^6 cm^2mol^{-1}. Extinction coefficients for other electronic transitions for the complexes are reported in Table 3.1. The uncertainty in the calculation of number of monolayers of $Fe(CO)_4PPh_3$ from IR absorbance is ±9 monolayers. This value was obtained from the signal-to- noise ratio of an $Fe(CO)_4PPh_3$ film with an IR absorbance of 0.036(±0.01), which is 33(±9) monolayers.

3.2.2 Photochemistry of $Fe(CO)_4PPh_3$

The spectroscopic changes resultant from photolysis of a 134 (±9) monolayer film (calculated from the IR absorbance at 1931 cm^{-1}) of $Fe(CO)_4PPh_3$ under vacuum are

shown in Figure 3.3. A decrease in intensity to baseline of the FTIR absorptions at 2048, 1973 and 1931 cm^{-1} associated with the carbonyl stretching vibrations, is observed. This indicates the loss of all starting material. The decrease in intensity of each absorption occurs with no change in the relative intensities of the absorption bands. Also, no new absorption is observed, therefore no direct evidence is found for the formation of an intermediate. This is consistent with an initial primary photoprocess yielding a thermally unstable intermediate, $Fe(CO)_3PPh_3$ as shown in equation 3.1. This intermediate then undergoes rapid thermal decomposition (eq. 3.2).

$$Fe(CO)_3PPh_3 \xrightarrow{k_2} Fe + 3\,CO + PPh_3 \qquad (3.2)$$

Figure 3.3 FTIR spectral changes associated with the photolysis for 0, 60,120, 210, 270, 330, 600 and 1365 min of a 134(±9) monolayer film of $Fe(CO)_4PPh_3$ deposited on Si(111).

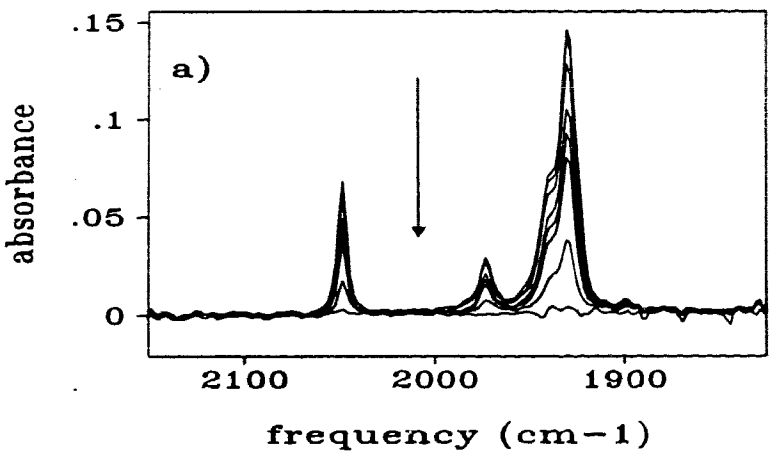

FTIR spectroscopic data following photolysis of $Fe(CO)_4PPh_3$ indicates loss of all starting material. The resultant film was analysed by Auger electron spectroscopy to determine if the ejected ligands diffused out of the film. The surface of the film was

composed of 14.1% Fe, 16.1% O, 1.6% P and 68.3% C. The results of the analysis of the film produced from $Fe(CO)_4PPh_3$ are indicative of loss of CO and PPh_3 from the film leaving a film composed primarily of carbon, iron, oxygen and PPh_3 (Table 3.1). The surface layer is oxidized, as expected for iron [84]. Further evidence for PPh_3 being retained in the film arises from the depth profiling experiments. The surface of the film contains less PPh_3 as indicated by the observation of an 8.8:1 ratio of iron-to-phosphorus on the surface. For longer sputtering times the interior of the film is exposed and higher amounts of phosphorus, a 5:1 Fe:P ratio, is evident. This is indicative of a greater ease of loss of PPh_3 from the surface than from the interior of the film. The C:P ratio was aproximately 43:1 on the surface and 21:1 inside the film. This is consistent with PPh_3 trapped in the film (C:P= 18:1) with excess carbon contamination.

Results of analysis of a film produced from *trans*-$Fe(CO)_3(PPh_3)_2$ were similar to the results from $Fe(CO)_4PPh_3$. The surface contained 10.3% Fe, 7.7% O, 1.9% P and 77.8% C. The Fe:P ratio was 5.4:1 on the surface, and 1.6:1 inside the film. On the surface, the C:P ratio was 41:1 on the surface and 14:1 inside the film. The reduced C:P ratio within the film is consistent with preferential sputtering of carbon. Presumably, the trphenylphosphine was trapped intact in the film. The Auger results are shown in Table 3.2.

Table 3.2 Auger analysis of films resultant from photolysis of $Fe(CO)_4PPh_3$ and *trans*-$Fe(CO)_3(PPh_3)_2$.

Initial Film Composition	Sputter Time (min)	% Fe[a]	% P[a]	% C[a]	% O[a]
$Fe(CO)_4PPh_3$	0	14.1	1.6	68.3	16.1
	3	16.9	3.4	71.8	7.8
$Fe(CO)_3(PPh_3)_2$	0.25	10.3	1.9	77.8	7.7
	1	8.6	5.5	77.9	8.0

[a] error approximately 5 atom % [85].

Previous studies of $Fe(CO)_4PPh_3$ [75] in other media indicated that the expected primary photoproducts are $Fe(CO)_3PPh_3$ and CO. This coordinatively unsaturated system is known to be susceptible to attack by two electron donor ligands, L, to yield $Fe(CO)_3PPh_3L$ [75].

In order to investigate if $Fe(CO)_3PPh_3$ was indeed formed in the thin film photoreaction, a film of codeposited $Fe(CO)_4PPh_3$ and PPh_3 was studied. This reaction was done with the aim of trapping the intermediate, $Fe(CO)_3PPh_3$, with PPh_3 to form $Fe(CO)_3(PPh_3)_2$. Spin coating a chip with a solution containing $Fe(CO)_4PPh_3$ and PPh_3 results in the formation of amorphous films composed of both compounds. In Figure 3.4, the spectroscopic changes resultant from photolysis of a film composed of both $Fe(CO)_4PPh_3$ and PPh_3 are shown.

Figure 3.4 Spectral data for the photolysis with 366 nm light of a film of $Fe(CO)_4PPh_3$ and PPh_3. The accumulated photolysis times are: 0, 5, 10, 15, 20, 30 and 75 min.

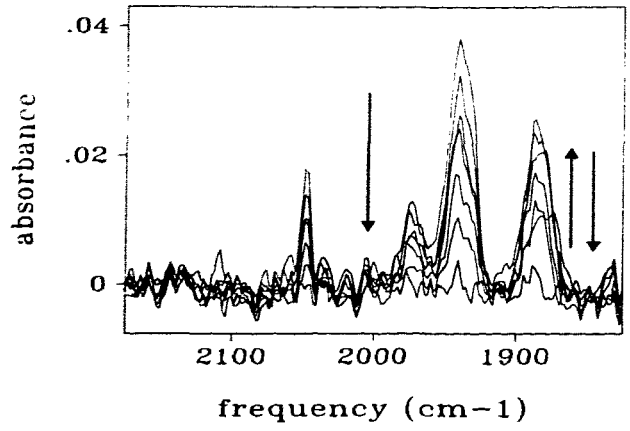

The loss of carbonyl absorption bands associated with $Fe(CO)_4PPh_3$ is observed and is accompanied by the growth of a new absorption at 1877 cm^{-1}. This absorption increases in intensity, reaches a maximum and then decays in intensity as a result of further photolysis. The transient absorption band at 1877 cm^{-1} is associated with the ν(CO) for *trans*-$Fe(CO)_3(PPh_3)_2$. This assignment has been confirmed by comparison with the absorption associated with an authentic sample of *trans*-$Fe(CO)_3(PPh_3)_2$ (Table 3.2). This assignment is consistent with the primary photoprocess being loss of the axial CO, forming $Fe(CO)_3PPh_3$ as in equation 3.1. This intermediate is trapped by PPh_3 within the film, according to equation 3.3 to form *trans*-$Fe(CO)_3(PPh_3)_2$, in competition with the decomposition reaction of $Fe(CO)_3PPh_3$ as in equation 3.2. It is also apparent that an additional weak absorption due to $Fe(CO)_2(PPh_3)_3$ is observed at 1838 cm^{-1}. The

formation of this species is associated with the subsequent photoreactions of *trans*-$Fe(CO)_3(PPh_3)_2$ which are treated separately in *Section 3.2.4.*

$$Fe(CO)_3PPh_3 + PPh_3 \xrightarrow{\Delta} \textit{trans}\text{-}Fe(CO)_3(PPh_3)_2 \qquad (3.3)$$

In order to assess the efficiency of the trapping reaction of $Fe(CO)_3PPh_3$ with PPh_3 (eq. 3.3) in competition with the decomposition of $Fe(CO)_3PPh_3$ (eq. 3.2), studies were done in which the amount of PPh_3 additive within the film was varied. The efficiency of trapping can be expressed as the ratio of *trans*-$Fe(CO)_3(PPh_3)_2$ formed to $Fe(CO)_4PPh_3$ lost. After 10 min photolysis of a 27(±9) monolayer film of $Fe(CO)_4PPh_3$ and PPh_3, the change in absorbance at 1931 cm^{-1} was 0.012 (11±7 monolayers). The change in absorbance of the band at 1877 cm^{-1}, corresponding to formation of *trans*-$Fe(CO)_3(PPh_3)_2$, was 0.014 (14±5 monolayers). After 30 min photolysis the total change in $Fe(CO)_4PPh_3$ was 19±9 monolayers, and 15±5 monolayers of *trans*-$Fe(CO)_3(PPh_3)_2$ was present. The ratio of *trans*-$Fe(CO)_3(PPh_3)_2$ formed to $Fe(CO)_4PPh_3$ lost decreases with photolysis time due to the photosensitivity of *trans*-$Fe(CO)_3(PPh_3)_2$.

The results of several experiments indicated that when no PPh_3 was added to the film, no *trans*-$Fe(CO)_3(PPh_3)_2$ is observed to form throughout the reaction. For films with 19 to 50 monolayers of PPh_3 added, the initial ratio of *trans*-$Fe(CO)_3(PPh_3)_2$ formed to $Fe(CO)_4PPh_3$ lost is R=1 within error, as long as some *trans*-$Fe(CO)_3(PPh_3)_2$ is observed. Due to the photosensitivity of *trans*-$Fe(CO)_3(PPh_3)_2$ this ratio decreases as the photolysis continues.

3.2.3 Quantum yield studies on $Fe(CO)_4PPh_3$

The variation in quantum yields for decomposition of $Fe(CO)_4PPh_3$was studied as the reaction conditions were changed. The effect of both film thickness and additives on the quantum yield for disappearance of $Fe(CO)_4PPh_3$ will be reported. First the effect of film thickness on the quantum yield will be presented.

For a 134(±9) monolayer film of $Fe(CO)_4PPh_3$ at room temperature, irradiation with 366 nm light led to loss of absorption bands associated with the starting material and no evidence was found for the formation of an intermediate (Fig. 3.3). A plot of absorbance *vs.* irradiation time was plotted as shown in Figure 3.5. These data were fit to an exponential decay which corresponds to equation 3.4. The incident light intensity, I_o (8.47×10^{-9} $Ecm^{-2}s^{-1}$), and the extinction coefficient, ε_{UV}, at 366 nm (3.78×10^6 cm^2mol^{-1}) were entered into equation 3.4. The quantum yield for decomposition, Φ, of $Fe(CO)_4PPh_3$ was calculated as 0.00038 (± 0.00005). Thermal decay rates for $Fe(CO)_4PPh_3$ (eq. 3.5), were also determined by a plot of absorbance *vs.* time. The thermal decomposition rate, k_T, for a film of $Fe(CO)_4PPh_3$ under vacuum was 1×10^{-6} s^{-1}. This is less than 5 % of the photochemical decay rate under these conditions and was therefore neglected in the quantum yield expression (equation 3.4).

$$A = A_o\exp[-(2.303\varepsilon I_o\Phi + k_T)(t)] \quad (3.4)$$

$$Fe(CO)_4PPh_3 \xrightarrow{k_T} Fe + 4\,CO + PPh_3 \quad (3.5)$$

Figure 3.5 Plot of the exponential decay of the absorbance at 1931 cm^{-1} *vs.* photolysis time for $Fe(CO)_4PPh_3$.

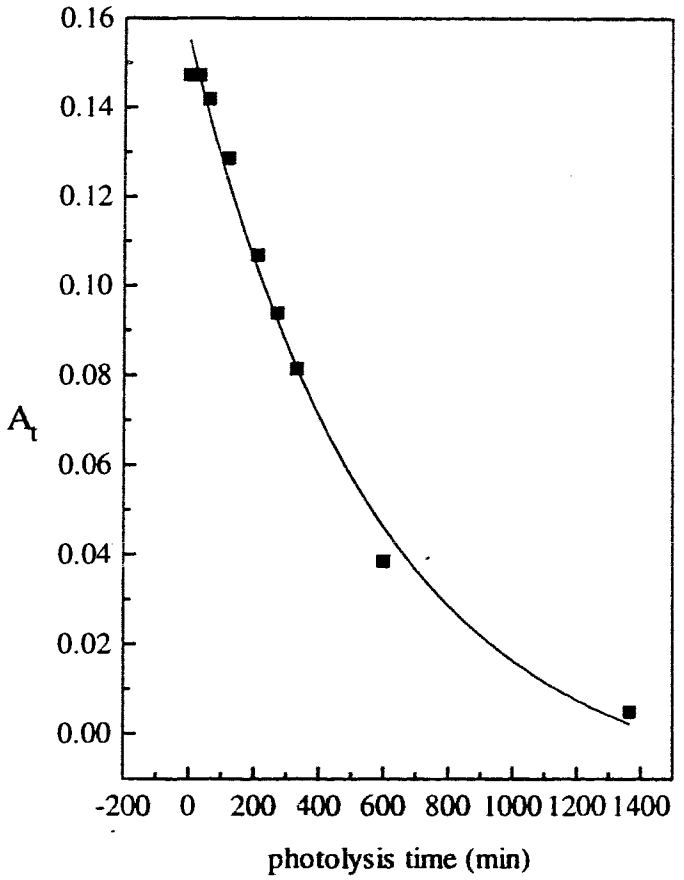

The dependence of the photoefficiency of $Fe(CO)_4PPh_3$ on film thickness was studied in some detail. Films of varying thickness were prepared and the photochemistry monitored for each film. The quantum yields are reported in Table 3.3. The general

trend observed is that as the film thickness increases the quantum yield decreases. For example, the quantum yield was 0.003 (±0.001) for a 7(±9) monolayer film, 0.0007 (±0.0001) for a 78(±9) monolayer film and 0.00038 (±0.00005) for a 134(±9) monolayer film. A detailed interpretation of this result is presented in the discussion. Before considering the interpretation of these quantum yields the influence of additives on the quantum yield will be presented.

Table 3.3 Quantum yields for decomposition of $Fe(CO)_4PPh_3$ as thin films.

Coverage molec/Å^2 (monolayers[a])	A_o	I_o (Es^{-1} cm^{-2})	Quantum Yield, Φ ($\pm \Phi$)	Atmos-phere	Add-itives	Additive Coverage[b], monolayers
0.10 (7)	0.0076	$9.08x10^{-9}$	0.0032 (± 0.001)	vac		
0.50 (33)	0.0362	$9.08x10^{-9}$	0.0016 (±0.0002)	vac		
0.66 (44)	0.0484	$9.08x10^{-9}$	0.0023 (± 0.0008)	vac		
1.18 (78)	0.0862	$8.99x10^{-9}$	0.00071 (± 0.0001)	vac		
2.01 (134)	0.147	$8.47x10^{-9}$	0.00038 (± 0.00005)	vac		
0.97 (64)	0.0707	$5.81x10^{-10}$	0.043 (± 0.004)	air		
1.12 (74)	0.0817	$8.56x10^{-10}$	0.011 (± 0.002)	air		
0.40 (27)	0.0293	$9.48x10^{-10}$	0.047 (± 0.02)	vac	PPh_3	48
1.35 (89)	0.0984	$8.56x10^{-10}$	0.048 (± 0.01)	air	PPh_3	39
1.18 (79)	0.0865	$8.99x10^{-9}$	0.0009 (± 0.0001)	vac	$HCPh_3$	20

[a]error ±9 monolayers $Fe(CO)_4PPh_3$, [b]calculated from IR absorbance

One additive to consider is the effect of air on the reaction. When films were monitored in an air atmosphere the spectral changes were similar to those observed in a vacuum. The quantum efficiency of the reaction in air was much higher than for films of

comparable thickness under vacuum. This indicates that the intermediate is oxygen sensitive. The data in Table 3.3 indicates an order of magnitude increase in the quantum yield as a result of conducting the photochemistry under an air atmosphere. For example, the quantum yield, Φ, for a 78(±9) monolayer film under vacuum was 0.0007 (±0.0001), whereas Φ for a 74(±9) monolayer film in air was 0.011 (±0.002).

The quantum yield for reaction of the films containing both $Fe(CO)_4PPh_3$ and PPh_3 can also be determined from FTIR spectral changes upon photolysis. Control experiments indicated that films containing both $Fe(CO)_4PPh_3$ and PPh_3 are thermally sensitive and the decay rates were measured. In this case the rate of thermal decomposition, k_T (s^{-1}), of $Fe(CO)_4PPh_3$ (eq. 3.5) could not be neglected.

The spectral changes presented in Figure 3.4 for a film containing 27(±9) monolayers of $Fe(CO)_4PPh_3$ and 48(±7) monolayers PPh_3 were used to determine the quantum yield. The quantum yield for the loss of $Fe(CO)_4PPh_3$ in films composed in part of PPh_3 can be calculated from an exponential decay fit of absorbance *vs.* irradiation time as shown in Figure 3.6. The light intensity, I_o (9.48×10^{-10} $Ecm^{-2}s^{-1}$), extinction coefficient at 366 nm, ε_{UV} (3.78×10^6 cm^2mol^{-1}) and thermal decay rate k_T (0.0004 ± 0.0001 s^{-1}) were entered into eq. 3.4. The quantum yield, Φ, is 0.05 (± 0.02). This value is significantly greater than the quantum yield in the absence of the PPh_3 additive.

Figure 3.6 Plot of the absorbance at 1931 cm^{-1} *vs.* photolysis time for a film composed of 27(±9) monolayers of $Fe(CO)_4PPh_3$ and 48(±7) monolayers of PPh_3.

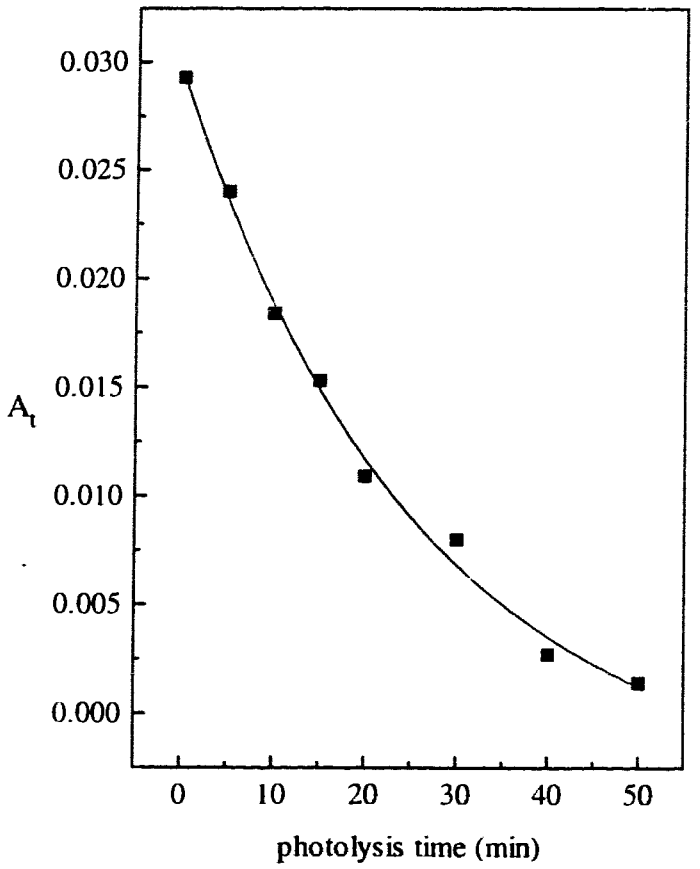

The effect of air on the quantum yield for a film mixture of $Fe(CO)_4PPh_3$ and PPh_3 was studied. For an 89(±9) monolayer film of $Fe(CO)_4PPh_3$ in the presence of both air and 39(±7) monolayers of PPh_3, the quantum yield, Φ,was 0.05 (±0.01). This quantum yield is the same as the quantum yield under vacuum conditions, of

$Fe(CO)_4PPh_3$ with a coverage of 27(±9) monolayers and 48(±7) monolayers PPh_3 as shown in Table 3.3 (Φ= 0.05 ±0.02). This comparison is only a qualitative one. The coverage of $Fe(CO)_4PPh_3$ and amount of PPh_3 added were different.

When an inert substance, such as $HCPh_3$ (20±10 monolayers) is added to a film of 79(±9) monolayers of $Fe(CO)_4PPh_3$, the quantum yield was 0.0009 (±0.0001). The quantum yield of a film with the same coverage of $Fe(CO)_4PPh_3$ with no additives is 0.0007 (±0.0001) which is not significantly different from the quantum yield in the presence of an inert substance.

3.2.4 Photochemistry of trans-$Fe(CO)_3(PPh_3)_2$

Amorphous films of trans-$Fe(CO)_3(PPh_3)_2$ exhibit a single ν(CO) absorption band at 1877 cm^{-1}. Irradiation of a thin film of trans-$Fe(CO)_3(PPh_3)_2$ results in a decrease in intensity of the single CO absorption band as illustrated in Figure 3.7. No new absorptions associated with a thermally stable intermediate were observed. The overall reaction initiated by photolysis occurs as in equation 3.6. Further evidence for the loss of all ligands from the complex comes from the Auger analysis which is consistent with the loss of all ligands yielding an impure (Table 3.2) iron surface.

$$\textit{trans}\text{-}Fe(CO)_3(PPh_3)_2 \xrightarrow{h\nu} Fe + 3\,CO + 2\,PPh_3 \qquad (3.6)$$

Figure 3.7 The FTIR spectral changes associated with the photolysis of a 14(±5) monolayer film of *trans*-$Fe(CO)_3(PPh_3)_2$ for 0, 2, 15, 30, 60, 120 and 245 min.

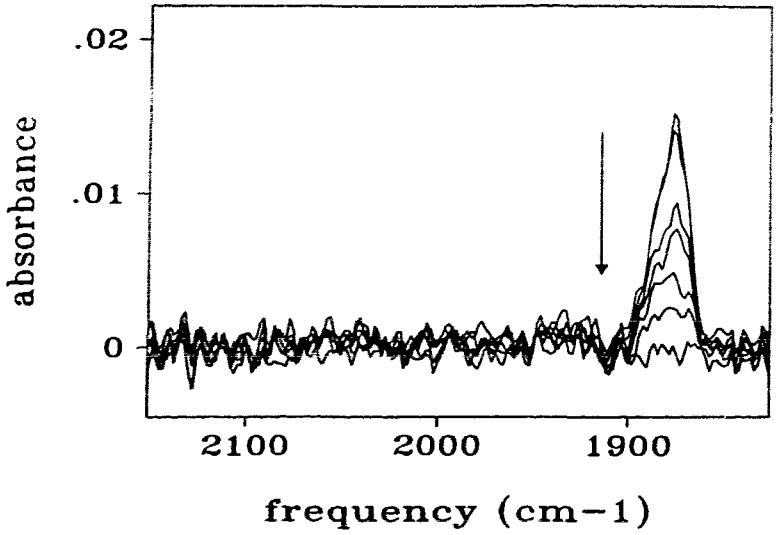

One interpretation is that the primary photoreaction of *trans*-$Fe(CO)_3(PPh_3)_2$ is the loss of CO yielding the thermally unstable species, $Fe(CO)_2(PPh_3)_2$. This would be consistent with the absence of any observable $Fe(CO)_n$ species. Further thermal decomposition would lead to iron, carbon monoxide and PPh_3. An alternative possibility would be the loss of the PPh_3 ligand leading to the unstable $Fe(CO)_3PPh_3$ discussed in *Section 3.2.2.*

In order to determine the primary photoprocess in the photoreaction of *trans*-$Fe(CO)_3(PPh_3)_2$ thin films, we prepared films of $Fe(CO)_3(PPh_3)_2$ with PPh_3 codeposited. If the initial photoreaction was CO loss, photolysis of these films would be expected to yield $Fe(CO)_2(PPh_3)_3$, *via* PPh_3 trapping of $Fe(CO)_2(PPh_3)_2$. Alternatively, if the initial photoreaction was loss of PPh_3, in the presence of codeposited PPh_3, the starting material,

$Fe(CO)_3(PPh_3)_2$ would be regenerated (eq. 3.3). This would be observed by a decrease in the decay rate compared to photolysis of films of *trans*-$Fe(CO)_3(PPh_3)_2$ with no additive.

Irradiation of a film of 34(±5) monolayers of *trans*-$Fe(CO)_3(PPh_3)_2$ and 14(±7) monolayers of PPh_3 results in the loss of intensity of the ν(CO) absorption at 1877 cm^{-1} for *trans*-$Fe(CO)_3(PPh_3)_2$. Concomitant growth of an absorption band at 1838 cm^{-1} is observed. This band and another at 1894 cm^{-1} (which overlaps the absorption centered at 1877 cm^{-1}) are attributed to the formation of $Fe(CO)_2(PPh_3)_3$ [83]. The steady state concentration of this species was quite small. The formation of $Fe(CO)_2(PPh_3)_3$ was also observed when a film of $Fe(CO)_4PPh_3$ and PPh_3 was photolysed as shown in Figure 3.4.

The photolysis of trans-$Fe(CO)_3(PPh_3)_2$ results in the loss of CO yielding $Fe(CO)_2(PPh_3)_2$ according to equation 3.7. The coordinatively unsaturated intermediate may either decompose (eq. 3.8), or in the presence of PPh_3, react to form $Fe(CO)_2(PPh_3)_3$ (eq. 3.9). The observation of $Fe(CO)_2(PPh_3)_3$ confirms that at least one reaction pathway must be CO loss.

$$\textit{trans}\text{-}Fe(CO)_3(PPh_3)_2 \xrightarrow{h\nu} Fe(CO)_2(PPh_3)_2 + CO \qquad (3.7)$$

$$Fe(CO)_2(PPh_3)_2 \xrightarrow{\Delta} Fe + 2\,CO + 2\,PPh_3 \qquad (3.8)$$

$$Fe(CO)_2(PPh_3)_2 + PPh_3 \xrightarrow{\Delta} Fe(CO)_2(PPh_3)_3 \qquad (3.9)$$

Alternatively, PPh_3 loss is a possible primary photoreaction (eq. 3.10) of *trans*-$Fe(CO)_3(PPh_3)_2$. If the photoreaction followed equation 3.10 then we would expect that the photoefficiency of reaction of *trans*-$Fe(CO)_3(PPh_3)_2$ in films containing PPh_3 should be lower than those containing no PPh_3. This is expected to result from trapping the

photogenerated $Fe(CO)_3PPh_3$ intermediate forming starting material as observed with the $Fe(CO)_4PPh_3$ system (*Sections 3.2.2 and 3.2.3*). If the photochemistry of the system is adequately described by equations 3.7, 3.8 and 3.9 then the quantum yield for films containing PPh_3 should be higher than the quantum yields for pure films. In the presence of PPh_3, the primary photoproduct, $Fe(CO)_2(PPh_3)_2$ can react with PPh_3 forming $Fe(CO)_2(PPh_3)_3$ (eq. 3.9). The formation of $Fe(CO)_2(PPh_3)_3$ would reduce the amount of $Fe(CO)_2(PPh_3)_2$ available to back react with CO, forming starting material. This competition of reaction pathways would increase the Φ for decomposition of *trans*-$Fe(CO)_3(PPh_3)_2$. Quantum yields for the decomposition of *trans*-$Fe(CO)_3(PPh_3)_2$ in films both with and without PPh_3 were measured in order to further assess the reaction pathway.

$$\textit{trans}\text{-}Fe(CO)_3(PPh_3)_2 \xrightarrow{h\nu} Fe(CO)_3PPh_3 + PPh_3 \qquad (3.10)$$

3.2.5 Quantum yield studies on trans-$Fe(CO)_3(PPh_3)_2$

The quantum yields for the photoreaction of *trans*-$Fe(CO)_3(PPh_3)_2$ were determined by monitoring the decay of starting material as a function of photolysis time. In Figure 3.8 the absorption at 1877 cm^{-1} for *trans*-$Fe(CO)_3(PPh_3)_2$ is plotted against photolysis time and fit to an exponential decay (eq. 3.4). In the absence of additives, the thermal decomposition rate, k_T, is minimal (<5% of the photochemical decay rate) and was neglected in the quantum yield calculation. The quantum yield of a 15(±5)

monolayer film of *trans*-$Fe(CO)_3(PPh_3)_2$ was calculated as follows. The incident light intensity, I_o, was 8.99 x 10^{-9} $Ecm^{-2}s^{-1}$, and the extinction coefficient at the irradiation wavelength, ε_{366}, is 5.77 x 10^6 cm^2mol^{-1}. The resultant quantum yield for disappearance of 15(±5) monolayers of *trans*-$Fe(CO)_3(PPh_3)_2$ is 0.004 (± 0.001) calculated using equation 3.4.

Figure 3.8 Plot of A_t *vs.* photolysis time for a film of *trans*-$Fe(CO)_3(PPh_3)_2$.

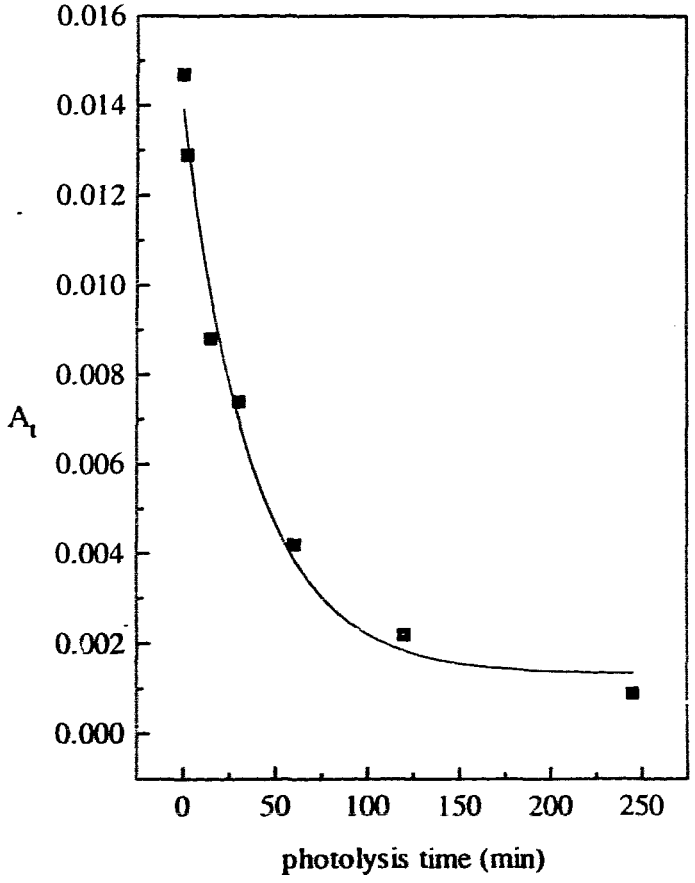

The quantum yield for a thicker film of *trans*-$Fe(CO)_3(PPh_3)_2$ was determined. A 79(±5) monolayer film of *trans*-$Fe(CO)_3(PPh_3)_2$ had a quantum yield of 0.006 (± 0.001). This is not significantly different from the quantum yield for a 15(±5) monolayer film (Table 3.4). In this system we find no quantum yield variation associated with the film thickness.

Similar experiments were conducted on samples with additives. Thermal decomposition rates, k_T, for film mixtures of *trans*-$Fe(CO)_3(PPh_3)_2$ and PPh_3 could not be neglected in the quantum yield calculation. The quantum yield for a 34(±5) monolayer film of *trans*-$Fe(CO)_3(PPh_3)_2$ with 14(±7) monolayers of PPh_3 was calculated as 0.07 (± 0.04). A 26(±5) monolayer film of *trans*-$Fe(CO)_3(PPh_3)_2$ with 21(±7) monolayers of PPh_3 had a quantum yield of 0.012 (± 0.007) in air. The results are summarized in Table 3.4.

Table 3.4 Quantum yields for reaction of *trans*-$Fe(CO)_3(PPh_3)_2$ in thin films.

Coverage, molec/Å^2 (monolayers)[a]	A_o	I_o ($Es^{-1}cm^{-2}$)	Quantum Yield, Φ ($\pm\Phi$)	Additive	Additive Coverage[b], monolayers	Atmos-phere
0.16 (15)	0.0147	$8.99x10^{-9}$	0.004(± 0.001)			vac
0.84 (79)	0.0788	$5.69x10^{-9}$	0.006(±0.001)			vac
0.36 (34)	0.0337	$9.79x10^{-10}$	0.07(±0.04)	PPh_3	14	vac
0.28 (26)	0.0263	$9.48x10^{-10}$	0.012(±0.007)	PPh_3	21	air

[a]calculated from absorbance at 1877 cm^{-1} (±9 monolayers) [b]calculated from absorbance at 1433 cm^{-1} (±7monolayers).

The results indicate that a large increase in the quantum yield for decomposition of *trans*-$Fe(CO)_3(PPh_3)_2$ is associated with the presence of PPh_3 in the film. The large

increase in quantum yield indicates that the primary photoreaction is CO loss as opposed to PPh_3 loss. The photoreactions involved are summarized in equations 3.7, 3.8, and 3.9.

3.2.6 Lithography

A film of $Fe(CO)_4PPh_3$ was irradiated through a standard lithography mask. The mask was placed in contact with the surface. Following photolysis the mask was removed and the unexposed starting material was rinsed with CH_2Cl_2. The surface resultant from this procedure is shown in Figure 3.9. The pattern produced consists of 1 μm by 50 μm lines of product material. The surface photochemistry is compatible with lithography in that patterned surfaces may be formed.

Figure 3.9 Optical micrograph of 1 μm features obtained by the photolithography of $Fe(CO)_4PPh_3$ on a Si(111) surface.

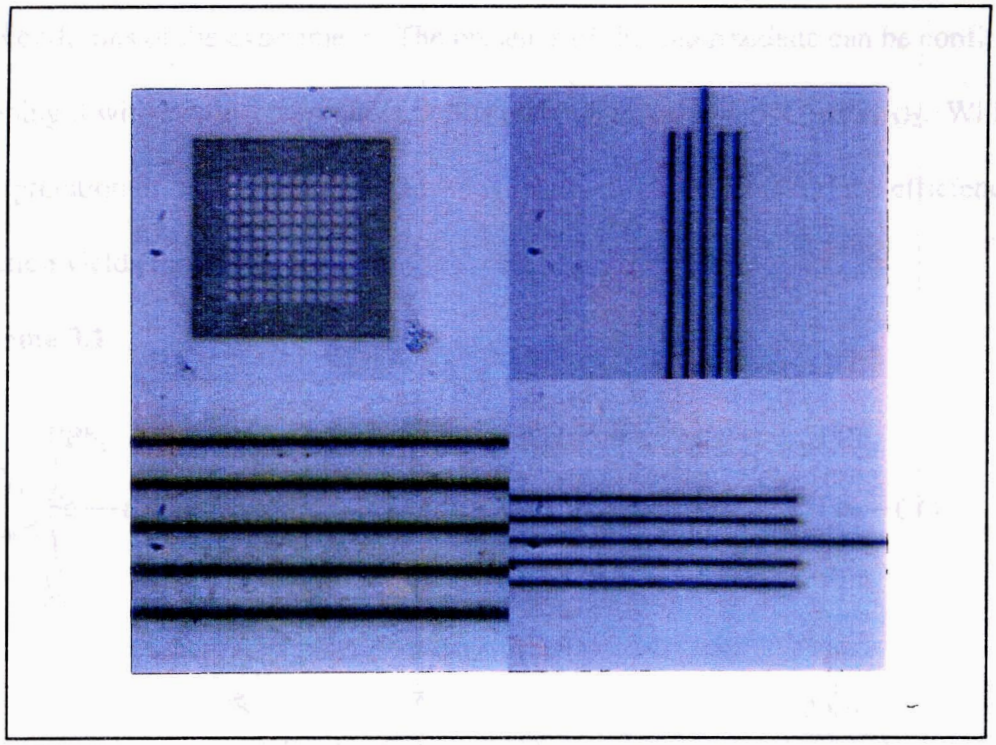

3.3 Discussion

The evidence presented in this chapter supports the mechanism outlined in Scheme 3.1. Photolysis of $Fe(CO)_4PPh_3$ leads to CO loss according to equation 3.1. The product, $Fe(CO)_3PPh_3$, is not sufficiently stable to be observed spectroscopically under the conditions of the experiment. The presence of this intermediate can be confirmed by trapping it with PPh_3. The product of this reaction is *trans*-$Fe(CO)_3(PPh_3)_2$. While this interpretation of the reaction mechanism is relatively straightforward the efficiency of the reaction yields further details.

Scheme 3.1

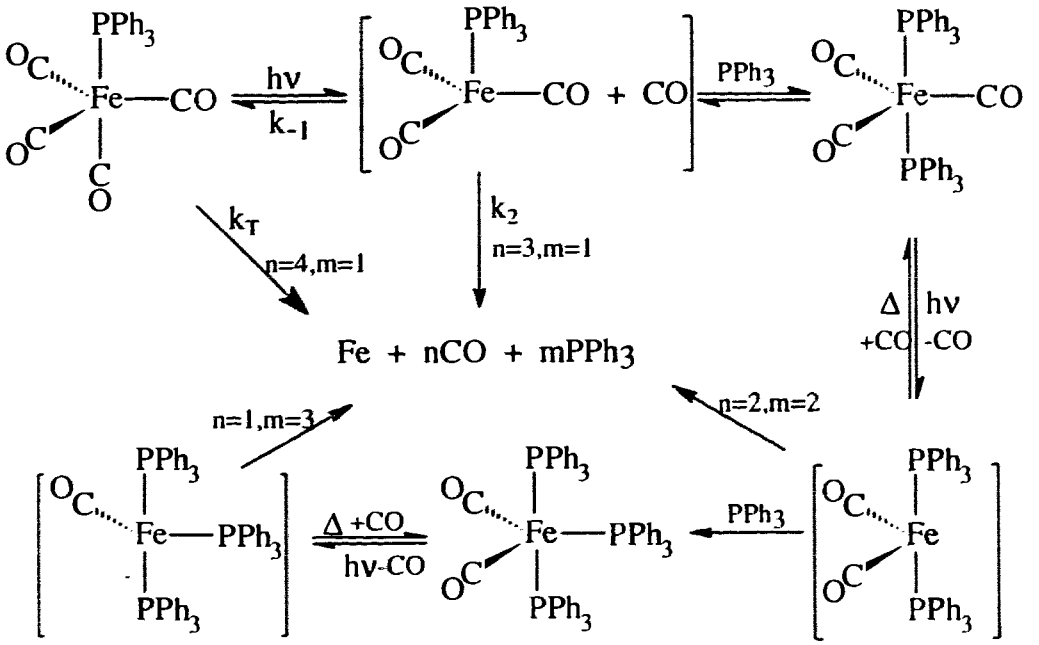

The quantum yield for this process has been measured for a variety of film thicknesses and is presented in Table 3.3. Thin films have a higher quantum yield for decomposition. This behaviour is due to the reaction of uncoordinated CO with the

unsaturated intermediate, $Fe(CO)_3PPh_3$. The intermediate was sufficiently stable to react with PPh_3 yielding *trans*-$Fe(CO)_3(PPh_3)_2$. It is expected that the photoproduced $Fe(CO)_3PPh_3$ within the films may be able to also trap the photogenerated CO according to equation 3.11. Thicker films would be expected to retain more CO leading to more efficient trapping and an overall lower quantum yield.

The photodecomposition of $Fe(CO)_4PPh_3$ fits the reaction summary shown in Scheme 3.1. The initial quantum yield, Φ^0, is for the loss of CO according to equation 3.1, forming $Fe(CO)_3PPh_3$. This intermediate can either decompose thermally with a rate, k_2, as in equation 3.2, or be trapped by CO with a rate of $k_{-1}[CO]$ as shown in equation 3.11. The quantum yield, Φ, may be expressed as a function of the initial quantum yield, Φ^0, times the fraction of $Fe(CO)_3PPh_3$ which thermally decomposes (k_2) prior to trapping by CO ($k_{-1}[CO]$) as shown in equation 3.12.

$$Fe(CO)_3PPh_3 + CO \xrightarrow{k_{-1}} Fe(CO)_4PPh_3 \qquad (3.11)$$

$$\Phi = \Phi^0 \frac{k_2}{k_{-1}[CO] + k_2} \qquad (3.12)$$

A plot of Φ^{-1} *vs.* [CO] is expected to yield a straight line. In our case the source of CO is the photochemical reaction itself. For thick films the quantum yield changes with time, indicating a buildup of CO. For thin films this does not occur indicating that CO diffuses out of the film and does not attain a sufficient concentration to alter the quantum yield. No direct measure of [CO] within the film is available although an estimate for the dependence of film thickness may be made.

Assuming the rate of effusion of CO in a film is constant then the CO concentration will be a function of the thickness of the film. Under these conditions we assume the proportion of CO retained, and hence [CO] to be related directly to film thickness. Under these assumptions equation 3.12 is rearranged and [CO] is replaced by a function of thickness. The expression is shown in equation 3.13 where L is the thickness in monolayers of the film and c is the proportionality constant. A plot of $(\Phi)^{-1}$ *vs.* number of monolayers is expected to be linear.

$$\frac{1}{\Phi} = \frac{k_{-1}cL}{\Phi^0 k_2} + \frac{1}{\Phi^0} \tag{3.13}$$

The plot of Φ^{-1} *vs.* number of monolayers of $Fe(CO)_4PPh_3$ is presented in Figure 3.10. This result is consistent with the functional form shown in equation 3.13.

Figure 3.10 Plot of Φ^{-1} *vs.* number of monolayers of $Fe(CO)_4PPh_3$.

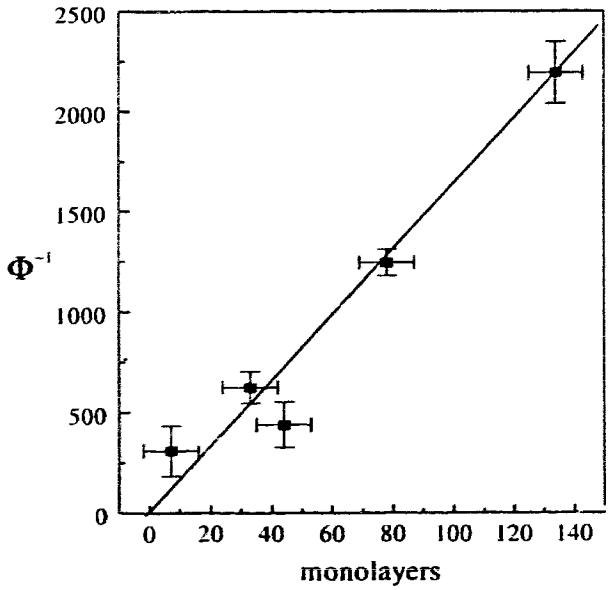

The results of the plot of Φ^{-1} *vs.* number of monolayers indicate that CO can also back react with the photoproduced fragment, $Fe(CO)_3PPh_3$. Therefore, equation 3.1 is reversible. This reaction is also illustrated in Scheme 3.1. Thicker films have lower quantum yields due to the fact that the photoejected CO has more opportunity to react with photofragments. This reduces the efficiency of decomposition of $Fe(CO)_4PPh_3$.

The reaction of PPh_3 with the unsaturated intermediate should also lead to a change in the quantum yield. The quantum yield variation resultant from a change in film composition is presented in Table 3.3. Treatment of this system is more complex as a change in the composition will affect not only the chemistry but also the physical properties of the film. The quantum yield for a film of codeposited PPh_3 and $Fe(CO)_4PPh_3$ was greater than the quantum yield for a $Fe(CO)_4PPh_3$ film of comparable coverage. This quantum yield increase is consistent with the primary photoreaction being CO loss. The trapping of the $Fe(CO)_3PPh_3$ intermediate with PPh_3 introduces a competition between recoordination of $Fe(CO)_3PPh_3$ with CO (eq. 3.11) and coordination of $Fe(CO)_3PPh_3$ with PPh_3 (eq. 3.3). The reactivity is summarized in Scheme 3.1.

Photoinduced loss of the axial CO in $Fe(CO)_4PPh_3$ results in the formation of $Fe(CO)_3PPh_3$. This species is thermally unstable and undergoes rapid thermal decomposition yielding iron films. Some recoordination of CO occurs in thick films. This presumably is due to the trapping of photoejected CO by the $Fe(CO)_3PPh_3$ fragment.

In the presence of a coordinating ligand, such as PPh_3, the intermediate is stabilised by the coordination of the added ligand. In the case of PPh_3, the product of

association is $Fe(CO)_3(PPh_3)_2$. This coordination results in an increase in the observed photoefficiency of decomposition of $Fe(CO)_4PPh_3$.

In the presence of the noncoordinating $HCPh_3$, the quantum yield was not significantly different from the quantum yield for $Fe(CO)_4PPh_3$ films of comparable thickness. There was no evidence for the formation of a thermally stable intermediate, indicating that $HCPh_3$ did not coordinate with the $Fe(CO)_3PPh_3$ fragment as expected. This indicates that dilution of the complex in a noncoordinating medium does not affect the efficiency of decomposition. This further supports that in the presence of PPh_3, the increase in quantum yield is a result of coordination of the additive.

Photolysis of *trans*-$Fe(CO)_3(PPh_3)_2$ led to loss of a CO ligand resulting in the formation of thermally unstable $Fe(CO)_2(PPh_3)_2$. In the presence of PPh_3, the quantum yield increased by an order of magnitude and the product of association is $Fe(CO)_2(PPh_3)_3$, observed in a low steady state concentration. The reaction mechanism is shown in Scheme 3.1.

3.4 Conclusions

Photochemical studies of amorphous films of $Fe(CO)_4PPh_3$ showed a dependence of quantum yield on film thickness. The primary photoreaction, loss of CO, is irreversible in thin films resulting in loss of all ligands with higher quantum yields. In thick films, the ejected CO does not diffuse through the film as fast and as a result reacts with the $Fe(CO)_3PPh_3$ intermediate. When the initial film is a mixture of $Fe(CO)_4PPh_3$ and PPh_3 the $Fe(CO)_3PPh_3$ intermediate reacts with PPh_3 forming *trans*-$Fe(CO)_3(PPh_3)_2$

which is photosensitive. The $Fe(CO)_3PPh_3$ intermediate was found to be oxygen sensitive based on the larger quantum yield for photodecomposition in air than that in vacuum. Independent photochemical studies of pure *trans*-$Fe(CO)_3(PPh_3)_2$ resulted in loss of all ligands with no observable intermediate. The primary photoreaction is CO loss followed by thermal decomposition of the thermally unstable $Fe(CO)_2(PPh_3)_2$ intermediate. This system was demonstrated to be compatible with current lithography techniques. However, Auger analysis indicated that the resultant films were contaminated with phosphorus and carbon. This was expected, due to the low volatility of PPh_3. For practical applications, a more volatile phosphine ligand in $Fe(CO)_4PR_3$ would be preferable due to increased diffusibility, such as $Fe(CO)_4PEt_3$.

3.5 Experimental details

3.5.1 Instruments and materials

The silicon wafers were obtained from Pacific Microelectronics Centre, Canada. Si (111) surfaces were used in these studies and the wafers were p-type silicon with tolerances and specifications as per SEMI Standard M1.1.STD.5 cut to the approximate dimensions 10 x 12 mm as needed. The CaF_2 crystals were obtained from Wilmad Glass Co. Inc.

The Fourier transform infrared (FTIR) spectra were obtained with 4 cm^{-1} resolution using a Bomem Michelson 120 FTIR spectrophotometer. The sampies were held in an anodized aluminum sample mount within a NaCl faced vacuum chamber. Under vacuum in the chamber was approximately 1 torr. Electronic absorption spectra

were obtained using an HP 8452A diode array spectrophotometer with a range 180 - 800 nm.

The photolysis beam was an Osram 100 W Hg lamp in an Oriel housing. The lamp was equipped with condenser lenses and the light was filtered through a 10 cm water filter with quartz optics. Additional filters (band pass 350 - 400 nm) to isolate the 366 nm emission line were used. The intensity of the light source was measured with an International Light IL1350 Radiometer.

Auger spectra were obtained using a PHI double pass CMA at 0.85 eV resolution at the Surface Physics Laboratory, Department of Physics, Simon Fraser University. The chromium plated quartz lithography mask was kindly donated by IBM Corp. The light source used for lithography experiments was an Osram 150 W high pressure Xe lamp. The resultant lithography images were printed on a Mitsubishi Colour Video Printer CP-10U.

3.5.2 Preparation of the amorphous thin films

The complexes $Fe(CO)_4PPh_3$ and *trans*-$Fe(CO)_3(PPh_3)_2$ were prepared by literature procedures by H. Blom [86, 87],and characterised by elemental analysis and FTIR and UV-vis spectroscopy. Results from elemental analysis are shown in Table 3.5. The films of the precursor complexes were prepared from solutions of the complexes in CH_2Cl_2. In the case of film mixtures of precursor and PPh_3, a solution of the two compounds was made. The following is a typical procedure for thin film preparation. A silicon chip was placed on a Teflon platform attached to a motor. The motor was turned

on and the silicon chip started spinning. A drop of a solution of $Fe(CO)_4PPh_3$ in CH_2Cl_2 was dispensed from a disposable pipette onto the silicon chip. The solution was allowed to spread and the solvent to evaporate. At this point, the motor was turned off and a thin film of the complex (or mixture) remained on the chip.

Table 3.5 Elemental analysis for the complexes $Fe(CO)_4PPh_3$ and *trans*-$Fe(CO)_3(PPh_3)_2$.

Complex	% C found (calc)	% H found (calc)
$Fe(CO)_4PPh_3$	61.67 (61.43)	3.55 (3.51)
trans-$Fe(CO)_3(PPh_3)_2$	70.69 (70.50)	4.44 (4.55)

3.5.3 Calibration of absorption on the surface

A stock solution of $Fe(CO)_4PPh_3$ (0.0134 g) was prepared in CH_2Cl_2 (5 ml). This solution was then diluted by a factor of 10 with CH_2Cl_2. A drop (0.0045 ml) of this solution was then deposited on the surface of a silicon chip. The solvent was allowed to evaporate and the FTIR spectrum was obtained. This process was repeated for several successive drops yielding the spectra shown in Figure 3.1. The area over which the film was deposited was measured to be 0.79 cm^2. Each drop of the solution corresponds to a coverage of 0.21 molecules per $Å^2$. The corresponding calibration curve of absorbance versus molecules/$Å^2$ for the absorbance at 1931 cm^{-1} is shown in Figure 3.1. The slope of this line yields an absorbance of 0.073 (± 10 %) $Å^2$/molecule. Assuming a molecular volume of approximately (8.1 Å)^3 [88], this corresponds to an absorbance of 0.0011/monolayer for the absorption at 1931 cm^{-1}. The corresponding extinction coefficients of the other absorption bands were obtained from their relative intensity to the absorption at 1931 cm^{-1} and are presented in Table 3.1.

The same treatment of a solution prepared from $Fe(CO)_3(PPh_3)_2$ (0.0055 g) in CH_2Cl_2 (5 ml) resulted in each drop contributing 0.56 molecules/Å^2 to the film. The spectra for the sequential drops and the resultant calibration curve are illustrated in Figure 3.2. An absorbance of 0.094 (± 14 %) Å^2/molecule is found for the single absorbance at 1877 cm^{-1}. The molecular volume of this molecule[1] is approximately (9.5 Å)^3 and the absorbance is 0.0010/monolayer.

Stock solutions of both PPh_3 and $HCPh_3$ were also made and the same procedure as described above was followed for each compound. The results for the calibration of absorbance on the surface can be found in Table 3.1.

The electronic absorption spectra were obtained by spin coating samples onto CaF_2 plates. Both FTIR and UV-vis spectra were obtained for each sample. The energies of the electronic transitions are obtained directly while the extinction coefficients were obtained relative to the absorption the infrared. Energies and extinction coefficients for both compounds are reported in Table 3.1.

The molar extinction coefficient at 366 nm for a film of $Fe(CO)_4PPh_3$ was determined as follows. An amorphous film of $Fe(CO)_4PPh_3$ was deposited on CaF_2. An electronic absorption spectrum was taken using the HP8452A spectrophotometer. An FTIR spectrum of this film was also taken. The ratio of the absorbance, A_{UV}, at 366 nm (0.054), to the absorbance, A_{IR}, at 1931 cm^{-1} (0.063) is 0.857. This ratio was multiplied by the IR extinction coefficient, ε_{IR}, in units of cm^{2}mol^{-1} (4.40x10^6 cm^{2}mol^{-1}). The extinction coefficient at 366 nm, ε_{UV}, is 3.78 x 10^6 cm^{2}mol^{-1}.

3.5.4 Photolysis of the complexes as thin films on silicon surfaces

All photolysis experiments were done in the same manner. For example, a Si (111) surface was prepared with an $Fe(CO)_4PPh_3$ film by dispensing a drop of a CH_2Cl_2 solution containing the iron complex onto the spinning silicon chip. This resulted in the formation of a uniform, amorphous coating of the silicon chip. The chip was then transferred to an anodized aluminum vacuum chamber. The system was placed under vacuum and the FTIR spectrum was obtained. The sample was then irradiated for 60 minutes and another FTIR spectrum was obtained. This procedure was repeated for the following (accumulated) photolysis times: 120, 210, 270, 330, 600 and 1365 minutes. The spectra are illustrated in Figure 3.3.

The intensity of the light source was measured before and after experiments, and the photon output was found to be constant throughout the experiments (to within 10%). The quantum yields were calculated as described elsewhere [41]. The results are described in Table 3.2.

In some experiments, additives were codeposited with the iron precursors from a single solution containing both components. The spectral results of photolysis of a mixture of PPh_3 with $Fe(CO)_4PPh_3$ is shown in Figure 3.4. The spectral results of photolysis of $Fe(CO)_3(PPh_3)_2$ are illustrated in Figure 3.5.

3.5.5 Lithography

A film containing $Fe(CO)_4PPh_3$ was spin coated onto a Si (111) surface, as described above. The sample was placed in contact with a lithography mask and irradiated through a 10 cm water filter and the mask using a 150 W high pressure Xe lamp for 36 hours. The sample was removed and rinsed with CH_2Cl_2 to dissolve the unexposed starting material. The image presented in Figure 3.9 was obtained using an optical microscope.

Chapter 4

Solid State Photochemistry of d^8 Square Planar Molecules of Platinum

4.1 Introduction

In this chapter, the photochemistry of amorphous films of square planar molecules of the formula $L_2Pt(CH_3)(N_3)$ (L= dppe/2, PPh_3, PEt_3), where dppe is $Ph_2PC_2H_4PPh_2$, is presented. The primary objective of this work is to deposit thin platinum films on silicon *via* a single photon mediated decomposition of precursor films of platinum complexes. Platinum complexes studied previously in our laboratory exhibited multiphoton decomposition. These molecules were selected due to the fact that they were predicted to have no stable intermediate in the photodecomposition reactions. The second objective is to determine if patterns of platinum can be photolithographed by irradiating precursor films through a standard lithography mask.

Platinum is useful in the electronics industry as Shottky diode contacts to both silicon and gallium arsenide [5]. The deposition of platinum by both chemical and photochemical vapour deposition has been investigated by a variety of workers [3-5, 89]. Our approach to deposition of platinum films allows for mild processing temperatures [43, 50, 51, 90]. However the efficiency of photodecomposition of amorphous films of platinum complexes, and the purity of the platinum films remain a problem.

The photochemical reactions of thin films of some $L_2Pt(CH_3)(N_3)$ complexes on Si(111) are presented here. The interest in these specific complexes is, in part, a result of earlier studies in which we investigated some diazide complexes of platinum. In these

earlier studies, we demonstrated that amorphous films of $(COD)Pt(N_3)_2$ (COD≡ 1,5-cyclooctadiene) [91] and $(dppe)Pt(N_3)_2$ [90] lost all azide ligands photochemically and yielded platinum films contaminated with carbon and, in the latter case, phosphorus. Each of these complexes decomposed in a stepwise process as outlined in equations 4.1 and 4.2. The first photochemical step was loss of an azide to form a thermally stable Pt(I) complex, L_2PtN_3, as shown in equation 4.1. This product was also photosensitive as shown in equation 4.2. The reactivity outlined in equation 4.1 is analogous to the solution photochemistry of palladium and platinum compounds of the formula $(Ph_3P)_2M(N_3)_2$ [92, 93, 94]. Subsequent photodecomposition of these complexes occurred *via* reaction with the solvent.

$$L_2Pt(N_3)_2 \xrightarrow{h\nu} L_2Pt(N_3) + N_3\cdot \qquad (4.1)$$

$$L_2Pt(N_3) \xrightarrow{h\nu} Pt + 2\,L + N_3\cdot \qquad (4.2)$$

The requirement of a second photon to decompose the Pt(I) intermediate is undesirable because it presents a limitation on the overall efficiency of the deposition process. Such a limitation on reaction efficiency is undesirable if these processes are to be implemented industrially. Therefore, in this study, monoazide complexes of platinum were investigated as precursors for the deposition of platinum films. The goal was to produce platinum films with a single photon mediated process. One of the azide ligands was replaced with a methyl group giving the formula, $L_2Pt(CH_3)(N_3)$. If the primary photoprocess is loss of an azide radical, the resultant intermediate expected in the study

reported here is $L_2Pt(CH_3)$. The substitution of the azide by the methyl was expected to result in reduced thermal stability of the Pt(I) intermediate due to the lack of π interaction of the remaining CH_3 with the metal. If the intermediate is sufficiently unstable, the decomposition of $L_2Pt(CH_3)$ will proceed thermally, eliminating the requirement of a second photon. This would result in a more efficient process for decomposition.

The complex (dppe)$Pt(CH_3)(N_3)$ (dppe= $(C_6H_5)_2PC_2H_4P(C_6H_5)_2$) was chosen to compare the mechanism of photodecomposition to that of the (dppe)$Pt(N_3)_2$ complex. The dppe ligand is a chelating ligand and it forces the molecule to have the *cis* orientation for a square planar complex. The PPh_3 and PEt_3 analogues possess the *trans* geometry and were chosen to compare the reactivity between *cis* and *trans* oriented platinum precursors. A difference in photoreactivity has been observed between (dppe)$Ni(N_3)_2$ and *trans*-$(Et_3P)_2Ni(N_3)_2$ [43] as thin films. Photolysis of (dppe)$Ni(N_3)_2$ [90] resulted in loss of the azide radical forming the stable product (dppe)$Ni(N_3)$ [90]. Photolysis of *trans*-$(Et_3P)_2Ni(N_3)_2$, however, ejected PEt_3, forming the stable dimer $[(Et_3P)Ni(N_3)_2]_2$ [43].

4.2 Results and Discussion

4.2.1 Spectroscopic data for the complexes

The FTIR spectra of the antisymmetric azide stretch of (dppe)$Pt(CH_3)(N_3)$, over a coverage range of 50 to 300 molecules/nm^2, on a silicon surface is shown in Figure 4.1 a). This range corresponds to approximately 37 to 222 monolayers [88]. At these coverages no apparent thermal chemistry occurs upon deposition. This is confirmed by the linear

plot of absorbance versus coverage shown in Figure 4.1 b). The energy of the antisymmetric azide stretch and its absorbance are summarised in Table 4.1.

Figure 4.1 Plot of absorbance of the antisymmetric N_3 stretch of (dppe)Pt(CH_3)(N_3) *vs.* coverage.

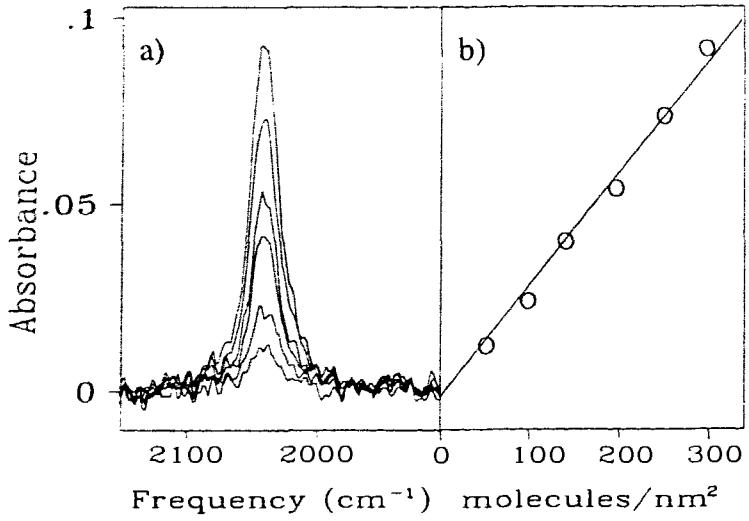

Table 4.1 Spectroscopic data for complexes of the formula $L_2Pt(CH_3)(N_3)$ (L= dppe/2, PPh_3, PEt_3), $(dppe)Pt(N_3)_2$ and $(dppe)Pt(N_3)$.

Complex	ν_a (N_3) (cm^{-1})	Absorbance ($monolayer^{-1}$)[a]
$(dppe)Pt(CH_3)(N_3)$	2043	0.00042
$(Ph_3P)_2Pt(CH_3)(N_3)$	2041	0.00023
$(Et_3P)_2Pt(CH_3)(N_3)$	2037	0.00042
$(dppe)Pt(N_3)_2$	2050, 2045	0.0010
$(dppe)Pt(N_3)$	2033, 2000	

[a] error approx. 10%

Similar spectra are found for the compounds $(Ph_3P)_2Pt(CH_3)(N_3)$ and $(Et_3P)_2Pt(CH_3)(N_3)$. All spectra are summarised in Table 4.1. Also included for comparison are spectral data of other platinum phosphine mono- and diazides that have previously been reported as surface films [90]. The position of the absorbances are similar to those of previously reported complexes on silicon surfaces. The absorbance intensity of the monoazides studied are approximately half the intensity of previously reported platinum phosphine complexes containing diazides (see Table 4.1). This indicates that there is no interaction between the azide ligands in the diazide complex to the intensity of the azide stretch.

4.2.2 Photochemistry of $L_2Pt(CH_3)(N_3)$ in the solid state (L= PPh_3, PEt_3, dppe/2)

Prior to describing the photochemistry of the films, it is worth considering the film thickness. If the molecular volume is estimated as approximately $(0.86\ nm)^3$ [88] then, at a coverage of 500 molecules/nm^2, the film is composed of ≈ 370 monolayers of (dppe)$Pt(CH_3)(N_3)$. The resultant thickness of such a film is approximately 320 nm. Because this thickness is less than the wavelength of light used, the film will be irradiated throughout its thickness. In all photolysis experiments the films were less than 300 nm thick.

A film, approximately 96 monolayers thick (calculated from absorbance at 2043 cm^{-1}), of (dppe)$Pt(CH_3)(N_3)$ was deposited on a silicon surface. Irradiation with ultraviolet light leads to a loss of absorbance of the FTIR band at 2043 cm^{-1} due to the azide ligand. The FTIR spectroscopic changes on photolysis are shown in Figure 4.2. No new absorptions that would indicate the formation of an intermediate were observed.

Similar results were obtained for the other complexes $L_2Pt(CH_3)(N_3)$ L = PPh_3, PEt_3. Photolysis of a 104 monolayer film of $(Ph_3P)_2Pt(CH_3)(N_3)$ (thickness calculated from the IR absorbance) leads to a loss of the absorption band at 2041 cm^{-1}. On photolysis of a 51 monolayer film of $(Et_3P)_2Pt(CH_3)(N_3)$ (thickness calculated from the IR absorbance) the absorption band at 2037 cm^{-1} decreased to baseline. In no case was there an absorption that would be indicative of an intermediate.

Figure 4.2 The FTIR spectral changes associated with the photolysis of a 96 monolayer film of (dppe)Pt(CH_3)(N_3) on Si(111). The cumulative photolysis times are: 0, 15, 25, 30, 40, 60, 90, 180 and 300 seconds.

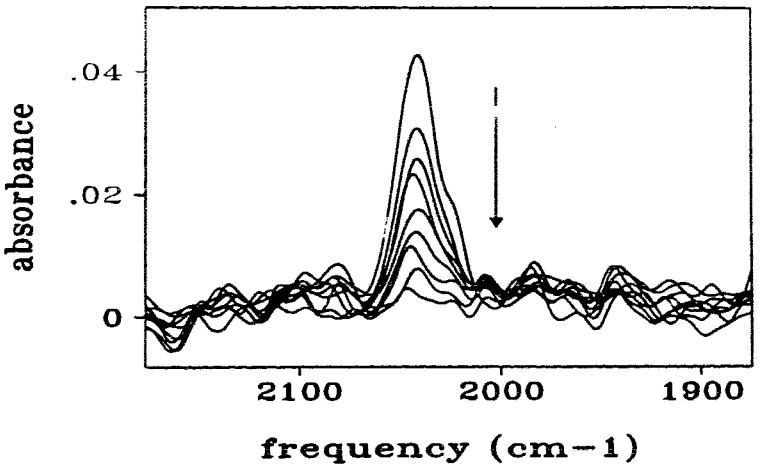

The above result is consistent with the loss of the azide ligand, resulting in thermal decomposition of the complex. Auger analysis was conducted on films resultant from photolysis to confirm that the complexes photodecomposed. In order to determine whether (dppe)Pt(CH_3) was formed during the reaction, two samples of (dppe)Pt(CH_3)(N_3) were prepared and irradiated. When the azide stretch was no longer observable in the FTIR spectrum (approximately 11 min), one of the samples was moved to the Auger spectrometer for further analysis. The other sample was irradiated for an additional 20 hours before Auger analysis. This procedure was also followed for the PPh_3 and PEt_3 analogues.

The results of Auger analysis are summarised in Table 4.2 along with the photolysis times. The results were dependent upon the phosphine donor ligand used. The complex (dppe)Pt(CH_3)(N_3) gave analyses consistent with the formation of primarily

platinum contaminated with some remaining dppe ligand. After 11 min photolysis, the film contained 37.8 % Pt, 4.7 % P and 57.4 % C. For every platinum atom in this film there was 0.12 phosphorus atoms. This indicates that dppe was lost on photolysis, since initially there were 2 phosphorus atoms per platinum atom. Following 20 h photolysis, the film also contained 0.12 phosphorus atoms per platinum atom. A film resultant from photolysis of $(Ph_3P)_2Pt(CH_3)(N_3)$ contained 0.13: 1 ratio of P: Pt after 9 min photolysis and 0.11: 1 of P: Pt following 20 h photolysis.

Table 4.2 Auger analysis following a 30 sec sputter with 3 kV Ar^+ ions of films resultant from photolysis of $L_2Pt(CH_3)(N_3)$ (L= dppe/2, PPh_3, PEt_3) films (pressure approx. 1 torr).

Complex	Photolysis time	Pt (%)[a]	P (%)[a]	N (%)[a]	O (%)[a]	C (%)[a]
(dppe)Pt(CH_3)(N_3)	11 min	37.8	4.7	0	0	57.4
(dppe)Pt(CH_3)(N_3)	20 h	39.6	4.6	0	0	54.4
(Ph_3P)$_2$Pt(CH_3)(N_3)	9 min	30.3	3.9	0	0	65.8
(Ph_3P)$_2$Pt(CH_3)(N_3)	20 h	34.4	3.9	0	0	61.7
(Et_3P)$_2$Pt(CH_3)(N_3)	7 min	67.8	4.2	3.8	3.8	24.0
(Et_3P)$_2$Pt(CH_3)(N_3)	17 h	47.0	3.8	7.9	7.9	38.9

[a] error approx 5% [85]

The experiments conducted on (Et_3P)$_2$Pt(CH_3)(N_3) yielded a significantly lower retention of donor ligand. However, the retention was still close to 0.07 phosphorus atoms per platinum atom. The amount of carbon relative to phosphorus detected was 5.7:1 which is consistent with the 6:1 C:P ratio for the phosphorus donor ligand present in the initial complex. The film resultant from the photolysis of (Et_3P)$_2$Pt(CH_3)(N_3) for 17 hours has approximately a 10:1 C:P ratio. The amount of carbon is in excess of that expected if all the carbon was associated with the remaining PEt_3. This is consistent with the excess carbon originating from hydrocarbon contamination from the atmosphere.

No significant difference was found between those samples irradiated until the FTIR absorption band decayed to baseline and those photolysed for longer periods. Thus, Auger analysis confirmed that at the point where the azide stretch is no longer detectable in the FTIR spectrum, the reaction is complete. This result is not consistent with the formation of a thermally stable intermediate of the formula $L_2Pt(CH_3)$.

The results may be explained in terms of equations 4.3 and 4.4. The initial photochemical reaction is shown in equation 4.3, where the absorption of a photon results in the loss of a single azide. There is precedent for this reaction occurring in amorphous films [90, 91]. The putative Pt(I) intermediates are not thermally stable and decompose to yield the final platinum films (equation 4.4). No difference in reactivity was observed on photolysis of *cis* or *trans* oriented $L_2Pt(CH_3)(N_3)$ films.

$$L_2Pt(CH_3)(N_3) \xrightarrow{h\nu} [L_2Pt(CH_3) + \bullet N_3] \quad (4.3)$$

$$[L_2Pt(CH_3)] \xrightarrow{\Delta} Pt + 2L + CH_3 \quad (4.4)$$

L= dppe/2, PPh_3, PEt_3

The azide radical [95, 96] is not observed, presumably due to its decomposition to nitrogen gas. This initial reactivity, loss of azide radical, is similar to the reactivity reported in solution for $(Ph_3P)_2Pt(N_3)_2$ [92, 93] and as surface films for a variety of diazido complexes [43, 97] including some of platinum [90, 91].

Film thickness measurements were made on films resultant from photolysis using optical interferometry. Film thickness after photolysis ranged from 25-100 nm $(Et_3P)_2Pt(CH_3)(N_3)$; 25 - 150 nm (dppe)$Pt(CH_3)(N_3)$; 50 - 67 nm $(Ph_3P)_2Pt(CH_3)(N_3)$. This is in the film thickness range of technically useful materials [5].

Finally, we demonstrated the compatibility of this method to standard lithography procedures by irradiating a sample of (dppe)$Pt(CH_3)(N_3)$ through a standard mask. The result of this procedure is shown in Figure 4.3. Clear formation of lines 3 μm wide are visible.

Figure 4.3 Scanning electron micrograph of a surface obtained by the photolithography of (dppe)Pt(CH_3)(N_3) on a Si(111) surface.

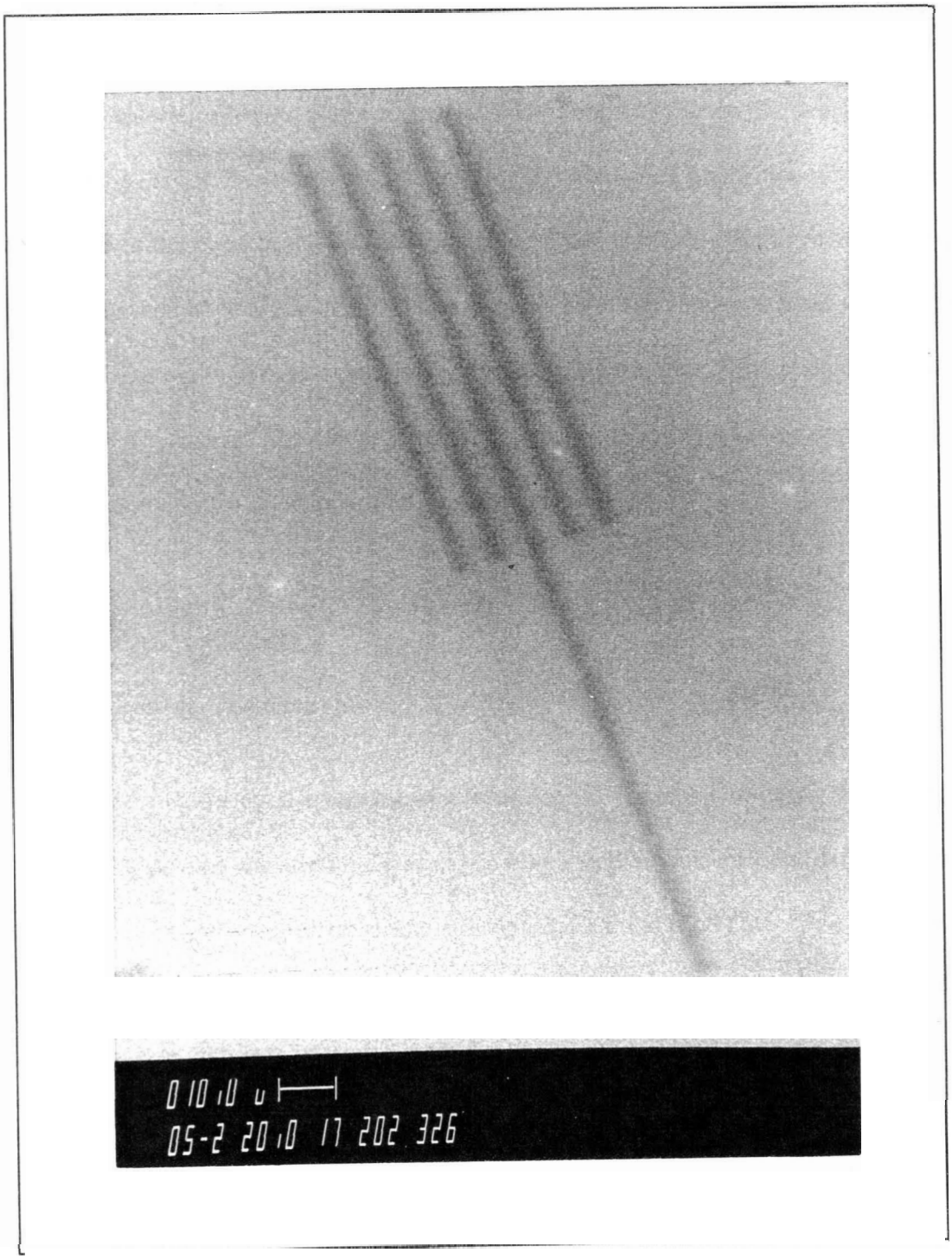

4.3 Conclusions

It was found that the surface reaction of $L_2Pt(CH_3)(N_3)$ could be monitored by FTIR spectroscopy. The complexes are all photosensitive and result in a single photon mediated decomposition to platinum metal. No difference in reactivity was observed between the *cis* and *trans* oriented molecules. The remaining impurities are consistent with some of the phosphorus donor ligand being retained intact. The important point is that greater than 85% of the ligand is lost in each case. The films produced in this way were deposited in thicknesses ranging from < 25 - 150 nm thick. The photochemical deposition of platinum films from amorphous films of $L_2Pt(CH_3)N_3$ (L= dppe/2, PEt_3, PPh_3) is compatible with standard lithography methods.

4.4 Experimental details

4.4.1 Instruments and materials

The silicon wafers were obtained from Pacific Microelectronics Center, Canada. The Si(111) surface was used in these experiments, and the wafers were p- type silicon with tolerances and specifications as per SEMI Standard M1.1.STD.5. The wafers were cut to the approximate dimensions of 10 x 12 mm in our laboratory. The NaCl and CaF_2 crystals were obtained from Wilmad Glass Co. Inc.

The samples were mounted in a NaCl or a CaF_2 -faced anodized aluminum vacuum chamber. The pressure in the chamber was approximately 1 torr under vacuum conditions. The Fourier transform infrared (FTIR) spectra were obtained with 4 cm^{-1}

resolution using a Bomem Michelson 120 FTIR spectrometer.

Electronic absorption spectra were obtained using an HP8452A photodiode array spectrophotometer in the range of 180 - 800 nm. CaF_2 was the substrate used for these experiments.

The irradiation source was an Osram 100 W high pressure mercury lamp in an Oriel housing equipped with condenser lenses and filtered through a 10 cm water filter with pyrex optics. This combination leads to primarily ligand-to-metal charge transfer (LMCT) excitation. Alternatively, a 75 W high pressure xenon lamp was used.

Auger electron spectra were obtained using a PHI double pass cylindrical mirror analyser (CMA) at 0.85 eV resolution at the Surface Physics Laboratory at Simon Fraser University. Scanning electron micrographs were obtained using an ETEC Corp. Autoscan U1 microscope in the Department of Biological Sciences, Simon Fraser University. Film thickness was determined using a Leitz Laborlux 12 ME S optical microscope with an interference attachment.

4.4.2 Preparation of the complexes

All methyl azide platinum complexes were prepared by Shaw and Bickley by the displacement of 1,5-cyclooctadiene (COD) from (COD)Pt(CH_3)(N_3) [98] by addition of the appropriate amount of phosphine in methylene chloride solution. The complex (COD)Pt(CH_3)(N_3) was also prepared by Shaw and Bickley [98 a)] from (COD)Pt(CH_3)(Cl) by metathesis with NaN_3 [98 b)]. The complexes were recrystallized from CH_2Cl_2 / hexane solutions. The spectroscopic data for the complexes are

summarised in Table 4.1. A combination of ^{1}H and ^{31}P NMR spectroscopy indicated a *trans* geometry for the PEt_3 and PPh_3 ligands [98].

4.4.3 Calibration of absorption on surface

A stock solution of $(C_2H_4(Ph_2P)_2)Pt(CH_3)(N_3)$ (0.0155 g) was prepared in CH_2Cl_2 (25 ml). A drop (0.0045 ml) of this solution was then deposited on the surface of a silicon chip. The solvent was allowed to evaporate and the FTIR spectrum was obtained. This area of the drop was found to be 0.5 cm^2. This corresponds to a coverage of 51 molecules per nm^2. This process was repeated several times yielding the spectra shown in Figure 4.1 a). A calibration curve of absorbance *vs.* number of molecules / nm^2 is shown in Figure 4.1 b). The slope of this line yields an absorbance of 0.00031 nm^2 / molecule. Assuming a molecular volume of approximately $(0.86\ nm)^3$ [88], this corresponds to an absorbance of 0.00042 / monolayer. This procedure was followed for all compounds to quantify the surface coverage of the films.

Similar experiments were conducted with $L_2Pt(CH_3)(N_3)$ ($L \equiv PPh_3$, PEt_3) which yields absorbances of 0.00020 and 0.00021 nm^2 / molecule. Making the above assumption of molecular volume yields absorbances of 0.00023 and 0.00042 / monolayer respectively.

4.4.4 Photolysis of complexes as thin films on silicon surfaces

All photolysis experiments were done in the same manner. A typical experiment follows. A silicon surface was prepared with (dppe)Pt(CH_3)(N_3) by dispensing a drop of a solution of the complex in CH_2Cl_2 onto a spinning silicon chip. The solvent was allowed to evaporate and the result was a uniform, amorphous coating of the chip. The chip was then transferred to a vacuum chamber. The system was placed under vacuum and the FTIR spectrum obtained. The sample was then irradiated for 15 sec and another spectrum was obtained. This procedure was repeated for the following cumulative photolysis times: 25, 30, 40, 60, 90, 180 and 300 seconds.

After photolysis, the sample was moved to the optical microscope and the film thickness was measured by interferometry. The samples were then moved to the scanning auger microprobe for elemental composition of the surface.

4.4.5 Lithography

A (dppe)Pt(CH_3)(N_3) film 150 nm thick was prepared on a Si(111) surface, as described above, and placed on a lithography mask. The light source used was a 150 W high pressure Xe lamp. The sample was irradiated from below through a 10 cm water filter and the mask (which was placed in contact with the film). After 44 hr photolysis, the sample was removed and rinsed with acetone. The sample was then transferred to the electron microscope. The image obtained is shown in Figure 4.3.

Chapter 5

A Mechanistic Study of the Solid State Photochemistry of *trans*-Square Planar Nickel, Palladium and Platinum Molecules

5.1 Introduction

This chapter will describe the solid state photochemistry of *trans*-$(R_3P)_2M(X)_2$ (M= Ni, R= Et, X= NO_2, NCO, NCS, CN; M= Pd, Pt, R= Et, X= NO_2; M= Ni, R= Bu, X= NO_2, NCO). The primary objective of this study was to produce nickel, palladium and platinum films on silicon. Many square planar nickel, palladium and platinum complexes studied previously in our laboratory exhibited multiphoton decomposition. In this study, the aim was to deposit nickel, palladium and platinum films *via* a single photon mediated decomposition of the amorphous precursor films. Another objective was to determine how reaction conditions may affect the photochemistry on various substrates. The final objective was to demonstrate that selective photolysis of precursor films using a conventional lithography mask is compatible with current lithography technology.

Previously in our laboratory, the photochemistry of *trans*-$(Et_3P)_2Ni(N_3)_2$ as a surface film was investigated [43]. While ligand field (LF, or d-d) excitation led to loss of $N_3^{\cdot}$, charge transfer (CT) excitation resulted in the photoextrusion of PEt_3. Both of these reactions produced thermally stable molecular products. Prolonged photolysis with UV light resulted in the loss of all ligands from the surface and the production of a (C and N contaminated) nickel oxide film. The related (dppe)$Ni(N_3)_2$ (dppe=

$(C_6H_5)_2PC_2H_4P(C_6H_5)_2$) underwent loss of an azide radical upon charge transfer excitation to yield (dppe)Ni(N_3) which was thermally stable within a surface film [90]. The conversion of this photoproduct to yield a metal film required an additional photon. For practical applications, a single photon mediated process is more desirable since the photochemistry is potentially more efficient. Thus, the aim is to design the precursor molecule such that the expected intermediate would be unstable, and hence undergo rapid thermal decomposition.

Despite the stability of (dppe)Ni(N_3), discussed above, the reactivity of Ni(I) (d^9) planar complexes should be high due to an unpaired electron in the highest occupied molecular orbital (HOMO). The stability of the (dppe)Ni(N_3) photoproduct may be a result of the interactions within the film and may not be a general phenomenon.

One approach to designing the precursor was investigated and discussed in Chapter 4. In Chapter 4, the precursor chosen was $L_2Pt(CH_3)(N_3)$ (L = PPh_3, PEt_3, dppe/2). The result was a single photon process for the decomposition of $L_2Pt(CH_3)(N_3)$, however, phosphorus impurity remained a problem.

In this chapter, one approach to designing the precursor was to select an alternative phosphine ligand. The PEt_3 ligand was chosen since it has a higher volatility than dppe. Also, in the case of a single M-P bond cleavage, the bidentate dppe ligand would be expected to have a greater chance for recombination than the monodentate PEt_3. Therefore, incorporation of PEt_3 or PBu_3 ligands should improve the purity of the final product.

The azide ligand was replaced with other pseudohalide ligands, in order to

investigate the stability of the Ni(I) species with different anionic ligands. Charge transfer excitation, involving metal and NO_2^- in solution often results in metal reduction [56, 57, 58]. If ligand-to-metal charge transfer (LMCT) excitation occurs upon irradiation of a film of *trans*-$(R_3P)_2Ni(NO_2)_2$, the resulting metal fragment would presumably be an unstable Ni(I) species.

Linkage isomerism of the anionic ligand is a possible competing photoreaction pathway which would waste energy without resulting in the production of metal. Linkage isomerism of the NO_2 ligand has been observed previously for complexes in solution as well as in the solid state [59, 60]. The photochemistry of the isothiocyanate (NCS) ligand has also been investigated and ligand loss [99], metal reduction [100], and isomerism [101] have all been reported in solution. Metal-to-ligand charge transfer (MLCT) excitation of cyano complexes is known to lead to anion loss [102, 103]. Substitution photoreactions of cyano (CN) complexes have been reported [104]. Very little has been reported on the photochemistry of isocyanato (NCO) complexes.

This chapter will describe the photodecomposition reactions of films of a series of complexes of the formula *trans*-$(R_3P)_2M(X)_2$ (M = Ni, R = Et, X = NO_2, NCO, NCS, CN; M = Pd, Pt, R = Et, X = NO_2; M = Ni, R = Bu, X = NO_2, NCO). The first part will describe the photodecomposition reactions for these compounds. This also includes surface analysis of the resultant films by Auger electron spectroscopy and photolithography of *trans*-$(Et_3P)_2Ni(NO_2)_2$ to investigate the compatibility of photodecomposition of films of inorganic compounds with current lithography techniques. In the second part of this chapter, the reaction efficiency of *trans*-

$(Et_3P)_2Ni(NO_2)_2$ as a function of substrate and atmosphere were investigated to determine whether the observed reactions were truly molecular in nature. Finally, the efficiency of photodecomposition for the series of complexes *trans*-$(R_3P)_2M(X)_2$ (M= Ni, R= Et, X= NO_2, NCO, NCS , CN;M= Pd, Pt, R= Et, X= NO_2; M= Ni, R= Bu, X= NO_2, NCO) was studied to investigate the stability of M(I) intermediates.

5.2 Results

5.2.1 Preparation of thin amorphous films

The complex, *trans*-$(Et_3P)_2Ni(NO_2)_2$, was dissolved in dichloromethane and spin coated on a silicon chip. Films made with this complex showed little tendency to crystallise. Amorphous films of all compounds were prepared by spin coating. It should be noted that films of *trans*-$(Et_3P)_2Ni(CN)_2$ had a tendency to crystallise, therefore several attempts were necessary to produce a film that would remain amorphous for the duration of the experiment. Amorphous films of all other complexes were spin coated from dichloromethane solutions. These films did not crystallize.

5.2.2 Spectroscopic data for the complexes

The spectroscopic data for all the complexes studied in this chapter are reported in Table 5.1. Assignments for absorption bands in the FTIR as well as UV-visible spectra for the compounds are reported in this table. The FTIR spectrum for the $(Et_3P)_2Ni(NO_2)_2$ complex exhibited 3 absorption bands due to the NO_2 ligand at 1377, 1321 and 816 cm^{-1}.

These absorption maxima were assigned as $\nu_a(NO_2)$, $\nu_s(NO_2)$ and $\delta(ONO)$ respectively [64, 105]. The position of these absorption bands indicate that the NO_2 ligand is N-bound. The nitrito ligand (-ONO), bound through the oxygen, has two $\nu(NO_2)$ absorptions, in the region 1485-1400 cm^{-1} for $\nu(N=O)$ and 1110-1050 cm^{-1} for $\nu(NO)$ [64]. The geometry of this complex is *trans*, as indicated by the absence of a third absorption band in the 1355-1337 cm^{-1} region which would correspond to *cis* geometry. Only one absorption band was observed in the $\delta(NO_2)$ region at 816 cm^{-1} which also corresponds to the *trans* geometry. The *cis* isomer would have 2 sharp absorptions in the $\delta(NO_2)$ region [64]. The three NO_2 analogues, $(Bu_3P)_2Ni(NC_2)_2$, $(Et_3P)_2Pd(NO_2)_2$, and $(Et_3P)_2Pt(NO_2)_2$, also have *trans* geometry. These complexes exhibited similar FTIR spectra and the absorption bands were assigned accordingly (see Table 5.1).

Table 5.1 Spectroscopic data for complexes of the formula *trans*-$(R_3P)_2M(X)_2$ (M= Ni, R= Et, X= NO_2, NCS, NCO, CN; M= Pd, Pt, R= Et, X= NO_2; M= Ni, R= Bu, X= NO_2, NCO).

Complex	UV-vis[a], nm (relative int.)	UV-vis, nm (lit.)	Assignment	IR, cm^{-1}	IR, cm^{-1} (lit.)	Assign-ment
$(Et_3P)_2Ni(NO_2)_2$	366 (0.08)		d-d[b], LMCT	1377	1374[c,d]	$\nu_a(NO_2)$
	323 (0.19)		d-d, LMCT	1321	1319	$\nu_s(NO_2)$
	282 (0.62)		MLCT	816	813	δ(ONO)
	238 (1.0)		MLCT			
$(Bu_3P)_2Ni(NO_2)_2$	370 (0.07)		d-d[b], LMCT	1381		$\nu_a(NO_2)$
	324 (0.20)		d-d, LMCT	1319		$\nu_s(NO_2)$
	284 (0.54)		MLCT	817		δ(ONO)
	236 (1.0)		MLCT			
$(Et_3P)_2Pd(NO_2)_2$	520 (0.01)		d-d[b]	1389		$\nu_a(NO_2)$
	344sh (0.48)		d-d, LMCT	1325		$\nu_s(NO_2)$
	278 (0.89)		MLCT	818		δ_s(ONO)
	236 (0.70)		MLCT			
	206sh (0.94)		MLCT			
	198 (1.0)		CT			
$(Et_3P)_2Pt(NO_2)_2$	514 (0.01)		d-d[b]	1393		$\nu_a(NO_2)$
	318 (0.52)		d-d, LMCT	1329		$\nu_s(NO_2)$
	288 (0.72)		MLCT	820		δ_s(ONO)
	242 (0.80))		MLCT			
	208 (1.0)		MLCT			
$(Et_3P)_2Ni(CN)_2$	346 (0.12)	339[e,f]	d-d[b], CT	2104	2103[e]	ν(CN)
	310sh (0.20)	308	d-d, MLCT			
	298 (0.28)	293	LMCT			
	254 (1.0)	252	LMCT			
	236sh (0.50)	234	CT			

Table 5.1 (continued)

Complex	UV-vis[a], nm (relative int.)	UV-vis, nm (lit.)	Assignment	IR, cm^{-1}	IR, cm^{-1} (lit.)	Assign-ment
$(Et_3P)_2Ni(NCS)_2$	376 (0.75)		d-d[b], LMCT	2091	2088[g]	ν(NC)
	312 (0.89)		d-d, LMCT	860	862	ν(CS)
	292sh (0.76)		LMCT			
	278 (0.72)		CT			
	252 (1.0)		LMCT			
	212sh (0.91)		CT			
$(Me_3P)_2Ni(NCS)_2$		435[h]	d-d[b], LMCT			
		348	d-d[i], LMCT			
		298				
		270				
		240	LMCT			
$(Et_3P)_2Ni(NCO)_2$	418 (0.25)		d-d[b]	2234		ν(NC)
	334 (1.0)		d-d[j], LMCT[k]	1344		ν(CO)
	288 (0.58)		LMCT	631vw		δ(NCO)
	272 (0.47)		LMCT			
	250 (0.78)		CT			
	228 (0.87)		CT			
$(Bu_3P)_2Ni(NCO)_2$	414 (0.13)		d-d[b]	2232		ν(NC)
	334 (0.92)		d-d[j], LMCT	1343		ν(CO)
	278 (0.47)		LMCT	635		δ(NCO)
	266 (0.40)		CT			
	244 (0.73)		LMCT			
	230 (1.0)		CT			
K[NCO]					2155[d]	ν(NC)
					1282,1202	ν(CO)
					630	δ(NCO)

vw= very weak, sh= shoulder

[a][105], [b][106], [c][107], [d][64] [e][108] [f]π(NCS)→d(Ni) [g][109] [h][110] [i]$d_{xz,yz} \rightarrow d_{x^2-y^2}$

[j]spectrum recorded in acetonitrile solution [107] [k]amorphous films on CaF_2 [k]P $\rightarrow d_{x^2-y^2}$

The FTIR spectrum for the complex $(Et_3P)_2Ni(CN)_2$, exhibited one ν(CN) absorption band at 2104 cm^{-1}. This is consistent with the literature value for the ν(CN) absorption for *trans*-$(Et_3P)_2Ni(CN)_2$ in a nujol mull at 2103 cm^{-1} [107].

The complex $(Et_3P)_2Ni(NCS)_2$ exhibited FTIR absorption bands at 2091 and 860 cm^{-1}. These were assigned as ν(NC) and ν(CS) respectively. These absorptions are consistent with the literature values for *trans*-$(Et_3P)_2Ni(NCS)_2$ at 2088 and 862 cm^{-1} [106]. The NCS ligand is coordinated at the nitrogen based on the position of the ν(CS) absorption band appearing at greater than 840 cm^{-1} and ν(NC) appearing below 2100 cm^{-1} [64, 111].

The complex $(Et_3P)_2Ni(NCO)_2$ exhibited ν(NC), ν(CO) and δ(NCO) absorptions at 2234, 1344 and 631 cm^{-1}. The increase in frequency of the ν(NC) and ν(CO) absorption bands from the free ion, which occur at 2183 and 1254 cm^{-1} respectively, indicate terminal coordination of NCO and is expected for N-bonding for the NCO ligand [109, 110]. The ligands are *trans* oriented, otherwise the FTIR spectrum would be expected to have an additional absorption band in the stretching region.

The electronic absorption spectra of the complexes on CaF_2 are reported in Table 5.1 [40, 107, 108, 112]. Charge transfer absorption bands are identified by their high molar extinction coefficients due to large changes in the dipole moment associated with the transition [40, 113]. At lower energy, weaker absorptions associated with d-d transitions are observed, but generally overlap the CT absorption bands. Three transitions are expected in this region for the *trans* planar structure [108, 112]. Figure 5.1 illustrates

the molecular orbital diagram for these molecules in their ground (Fig. 5.1 a)) and various excited (Fig. 5.1 b, c, d) states.

Figure 5.1 Molecular orbital diagrams for d^8 *trans*-planar molecules $(R_3P)_2M(X)_2$ a) ground state b) *i)* $d_{Z^2} \rightarrow d_{X^2-y^2}$ *ii)* $d_{XZ,YZ} \rightarrow d_{X^2-y^2}$ *iii)* $d_{XY} \rightarrow d_{X^2-y^2}$ c) $X(\pi) \rightarrow d_{X^2-y^2}$ (LMCT) d) $d_{Z^2} \rightarrow X(\pi^*)$ (MLCT)

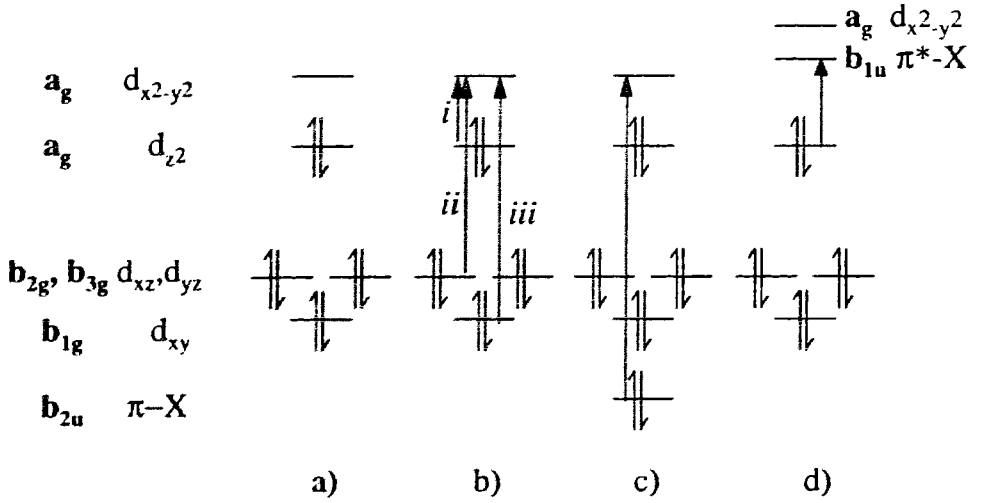

The molecules have approximately D_{2h} symmetry, in which the anionic ligands lie on the x-axis and the phosphine ligands lie on the y-axis. The lowest energy absorption band observed in the UV-vis spectrum for each complex was assigned as d_{XZ}, $d_{YZ} \rightarrow d_{X^2-y^2}$. It should be noted that the two orbitals d_{XZ} and d_{YZ} are not degenerate in *trans* square planar molecules. However, they are close in energy and are not resolved. Therefore, they are written here as degenerate for clarity. The other two d-d transitions ($d_{Z^2} \rightarrow d_{X^2-y^2}$ and $d_{XY} \rightarrow d_{X^2-y^2}$) were not observed. These absorption bands are often not observed for complexes of this type [108]. The energy of the observed d-d absorption for these complexes increases according to the spectrochemical series with respect to the

anionic ligand $NCS^- < NO_2^- < CN^-$ [108].

For complexes of the formula *trans*-$(R_3P)_2M(NO_2)_2$ (M= Ni, Pd, Pt, R= Et; M= Ni, R= Bu), the absorption band found in the region 318-344 nm was assigned as the $(\pi)NO_2 \rightarrow d_{x^2-y^2}$ LMCT transition [112]. This assignment is based on the trend expected for LMCT transitions in d^8 square planar Ni, Pd and Pt complexes [112]. The absorption band at 312 nm for the complex, *trans*-$(Et_3P)_2Ni(NCS)_2$, was assigned to the $(\pi)NCS \rightarrow d_{x^2-y^2}$ LMCT transition based on the literature assignment for *trans*-$(Me_3P)_2Ni(NCS)_2$ (Table 5.1) [108]. Assignments for *trans*-$(R_3P)_2Ni(NCO)_2$ (R= Et, Bu) were made analogous to the NCS complex. The absorption at 310 nm for the complex *trans*-$(Et_3P)_2Ni(CN)_2$ was assigned as the $d_{z^2} \rightarrow \pi^*(CN)$ MLCT transition [107, 108]. This is due to the lowering of the $\pi^*(CN)$ to below that of the $d_{x^2-y^2}$ orbital. Also at this energy is the $(\pi)CN \rightarrow d_{x^2-y^2}$ LMCT transition.

5.2.3 Photochemistry of amorphous films of trans-$(R_3P)_2M(X)_2$ (M = Ni, R = Et, X = NO_2, NCS, CN, NCO; M = Pd, Pt, R = Et, X = NO_2; M = Ni, R = Bu, X = NO_2, NCO)

A plot of the absorbance for the $\nu_s(NO_2)$ stretch for *trans*-$(Et_3P)_2Ni(NO_2)_2$ at 1321 cm^{-1} *versus* coverage in molecules/$Å^2$ was found to be linear for the range of film thickness used in all experiments. This plot is illustrated in Figure 5.2. The slope of this plot, 0.022 $Å^2$/molecule, is the IR extinction coefficient, ε_{IR} for *trans*-$(Et_3P)_2Ni(NO_2)_2$ on silicon. A similar series of spectra was done for all compounds studied here. The results are summarized in Table 5.2. The plots are linear indicating that the FTIR absorbance

may be used as an indication of the amount of a species within the film in this absorbance range. The FTIR absorbance of amorphous films will be used to monitor the extent of reaction in these systems.

Figure 5.2 Plot of absorbance at 1321 cm^{-1} *vs.* coverage for *trans*-$(Et_3P)_2Ni(NO_2)_2$.

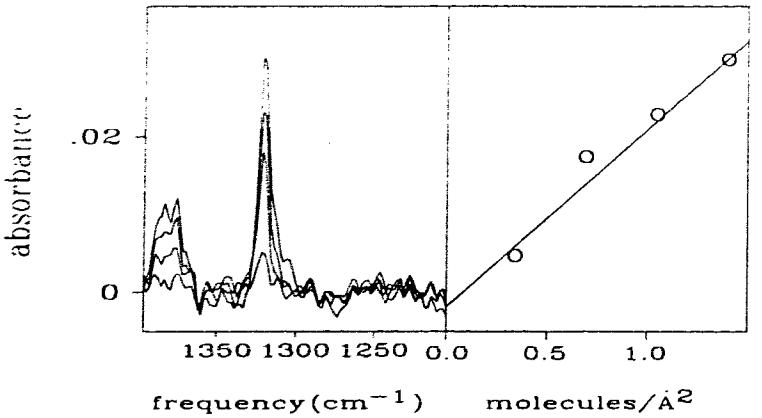

Table 5.2 FTIR absorbance *vs.* coverage data for complexes of the formula *trans*-$(R_3P)_2M(X)_2$ (M= Ni, R= Et, X= NO_2, NCS, NCO, CN; M= Pd, Pt, R= Et, X= NO_2; M= Ni, R= Bu, X= NO_2, NCO).

Complex	IR frequency (cm^{-1})	ε_{IR} ($Å^2$molecule^{-1})[a]	FTIR Abs/monolayer[a]
$(Et_3P)_2Ni(NO_2)_2$	1321	0.022	0.00041
$(Bu_3P)_2Ni(NO_2)_2$	1319	0.011	0.00015
$(Et_3P)_2Pd(NO_2)_2$	1325	0.016	0.00030
$(Et_3P)_2Pt(NO_2)_2$	1329	0.013	0.00024
$(Et_3P)_2Ni(NCS)_2$	2091	0.039	0.00072
$(Et_3P)_2Ni(CN)_2$	2104	0.009	0.00018
$(Et_3P)_2Ni(NCO)_2$	2234	0.051	0.00094
$(Bu_3P)_2Ni(NCO)_2$	2232	0.051	0.00070

[a] error approximately 10%

A thin film of *trans*-$(Et_3P)_2Ni(NO_2)_2$ was photolysed with a high pressure mercury arc lamp. The output of the light was filtered with a band pass 320 nm < λ < 420 nm. This permits the 334 and 366 nm Hg lines to irradiate the sample. Changes in the FTIR spectrum upon irradiation are shown in Figure 5.3. Loss of absorption bands at 1375 and 1321 cm^{-1}, due to the coordinated nitrite, is observed with no evidence for the formation of a thermally stable Ni species.

Figure 5.3 FTIR spectral changes associated with the photolysis for 0, 60, 150, 210, 570 and 1350 min for a film of *trans*-$(Et_3P)_2Ni(NO_2)_2$ deposited on p-type Si(100) in vacuum.

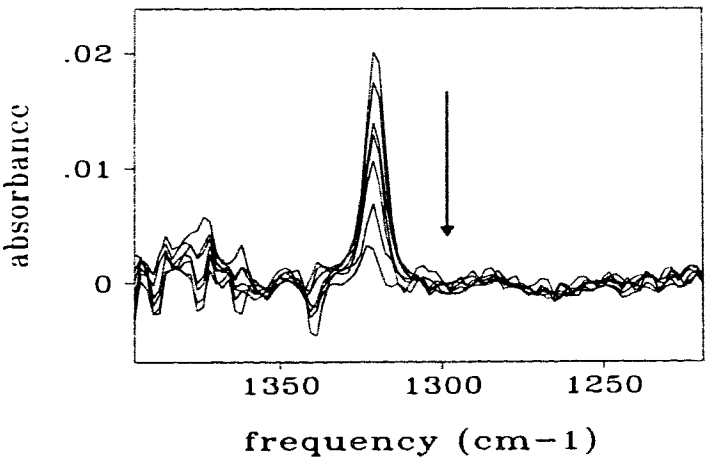

The FTIR spectral results shown in Figure 5.3 are consistent with loss of the NO_2 ligand as a radical forming an unstable Ni(I) species. This is followed by rapid thermal decomposition of the unstable nickel species (eq. 5.1). This behaviour is most consistent with ligand-to-metal charge transfer (LMCT) excitation resulting in the loss of an NO_2 radical, as shown in equation 5.1.

$$\textit{trans}\text{-}(Et_3P)_2Ni(NO_2)_2 \xrightarrow{h\nu}$$

$$[(Et_3P)_2Ni(NO_2) + \bullet NO_2] \xrightarrow{\Delta} Ni + 2\,PEt_3 + \bullet NO_2 \qquad (5.1)$$

Photolysis of films of *trans*-$(R_3P)_2M(X)_2$ (M= Ni, R= Et, X= NCS, CN; M= Pd, Pt, R= Et, X= NO_2; M= Ni, R= Bu, X= NO_2) with $320 < \lambda < 420$ nm (i.e. 334 and 366 nm) light resulted in the loss of FTIR absorption bands associated with the complexes. No evidence for the formation of a thermally stable metal species was observed. This behaviour is consistent with LMCT excitation resulting in the loss of X as a radical followed by rapid thermal decomposition of the metal (I) species (equation 5.2).

$$\textit{trans}\text{-}(R_3P)_2M(X)_2 \xrightarrow{h\nu}$$

$$[(R_3P)_2M(X) + X\bullet] \xrightarrow{\Delta} M + 2\,PR_3 + 2\,X\bullet \qquad (5.2)$$

M= Ni, R= Et, X= NCS, CN;

M= Pd, Pt, R= Et, X= NO_2;

M= Ni, R= Bu, X= NO_2

When *trans*-$(Et_3P)_2Ni(NO_2)_2$ was irradiated with 366 nm light only, the loss of all absorption bands was also observed. However, the decomposition on photolysis with 366

nm light was much less efficient than photolysis with 320 <λ<420 nm light. Absorption of the complex at 366 nm results in both reactive LMCT and unreactive d-d excited states. Therefore, the photodecomposition of the complex *via* LMCT excitation with 366 nm light requires a longer irradiation time. A similar reduction of efficiency of photodecomposition was observed when the complexes *trans*-$(R_3P)_2M(X)_2$ (M= Ni, R= Et, X= NCS, M= Pd, Pt, R= Et, X= NO_2; M= Ni, R= Bu, X= NO_2) were irradiated with 366 nm. In the case of the *trans*-$(Et_3P)_2Ni(CN)_2$ the quantum yield for decomposition was approximately the same at 334 nm and at 366 nm. This is consistent with approximately the same portion of the light absorbed at 320<λ<420 nm and at 366 nm have LMCT character.

The complexes *trans*-$(R_3P)_2Ni(NCO)_2$ (R = Et, Bu), exhibited different reactivity. The spectroscopic data for these reactions are summarized in Table 5.3. Upon photolysis of a film of *trans*-$(Bu_3P)_2Ni(NCO)_2$ with 320<λ<420 nm (i.e. 334 and 366 nm) light, loss of intensity of the absorptions at 2232, 1343 and 635 cm^{-1} was observed. Concomitant growth of new absorption bands at 2188, 1315, 657 and 620 cm^{-1} occurred. This photoproduct was thermally stable. Upon further photolysis all absorption bands decreased in intensity to the baseline (Figure 5.4).

Table 5.3 Spectroscopic data for photodecomposition reactions of *trans*-$(R_3P)_2Ni(NCO)_2$ (R = Et, Bu)

Complex	ν(NC), cm^{-1}	ν(CO), cm^{-1}	δ(NCO), cm^{-1}
trans-$(Bu_3P)_2Ni(NCO)_2$	2232	1343	635
M-N-M[a]	2188s	1315w	657,620
trans-$(Et_3P)_2Ni(NCO)_2$	2234	1344	631
M-N-M[b]	2189s	1317w	nd

s = strong, w = weak, nd = not detectable

[a, b] $[(R_3P)(NCO)(Ni\mu\text{-}(NCO)_2)_xNi(PR_3)(NCO)]$, R= [a]Bu, [b]Et

Figure 5.4 FTIR spectral changes for the photolysis with 320 <λ< 420 nm light of a film of *trans*-$(Bu_3P)_2Ni(NCO)_2$. Accumulated photolysis times were:0, 10, 35, 70, 160, 1250 and 2480 min.

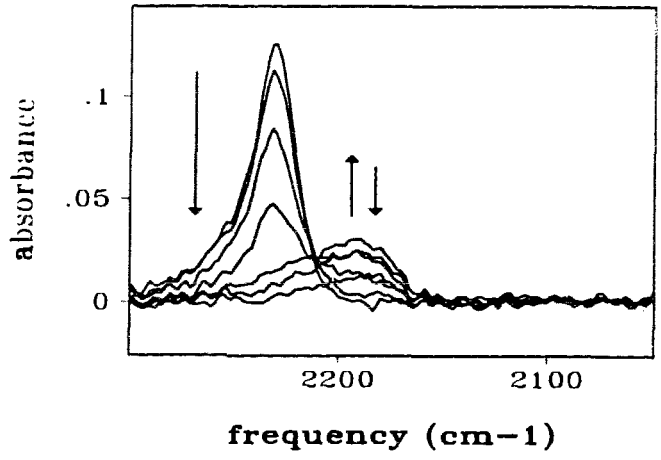

The ν(NC) absorption at 2188 cm^{-1} observed on photolysis of *trans*-$(Bu_3P)_2Ni(NCO)_2$ is consistent with bridging NCO. However, the positions of the ν(CO) and δ(NCO) are necessary to deduce the structure of the photoproduct [109]. The NCO bending mode of the photoproduct was observed at 657 and 620 cm^{-1}. This splitting of

the δ(NCO) of more than 30 cm^{-1} is indicative of bridging NCO. If it were terminally bonded isocyanate, splitting would be 10 cm^{-1} or less [109]. The ν(CO) absorption for *trans*-$(Bu_3P)_2Ni(NCO)_2$ at 1343 cm^{-1} decayed on photolysis with concomitant growth of a weak absorption band at 1315 cm^{-1}. This evidence further supports the bridging mode since ν_s(CO) is 30 - 60 cm^{-1} lower in bridged complexes and has a much reduced intensity. The bridging NCO ligand is believed to be bonding by M-N-M rather than M-NCO-M (Figure 5.5). The ν(NC) was observed at 2188 cm^{-1} whereas if it were bonded by M-NCO-M, the ν(NC) would be expected to be higher in energy than 2200 cm^{-1} [109]. To date, the only established mode of bonding for the bridging isocyanate ligand is M-N-M [110].

Figure 5.5 Possible bonding modes for the isocyanate ligand.

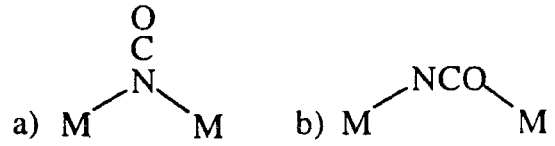

The FTIR data for the photoproduct following photolysis of *trans*-$(Bu_3P)_2Ni(NCO)_2$ is consistent with the formation of a thermally stable bridging NCO species. If the product was $[(Bu_3P)_2Ni(\mu\text{-}NCO)]_2$ produced by NCO radical loss the product would be a Ni(I) species which should be unstable. The FTIR spectral changes are consistent with PBu_3 loss on photolysis. The reactive Ni(II) intermediate either decomposes or dimerises with another Ni(II) fragment forming $[(Bu_3P)Ni(NCO)(\mu\text{-}NCO)]_2$ (equation 5.3). This dimer is also photoreactive ejecting another PBu_3 ligand (equation 5.4). The Ni(II) dimer fragment (eq. 5.4) may either react with another Ni(II) monomeric fragment (equation 5.5) or decompose thermally (equation 5.6). The FTIR

absorptions due to the terminal NCO may be obscured by the starting material or too weak to observe.

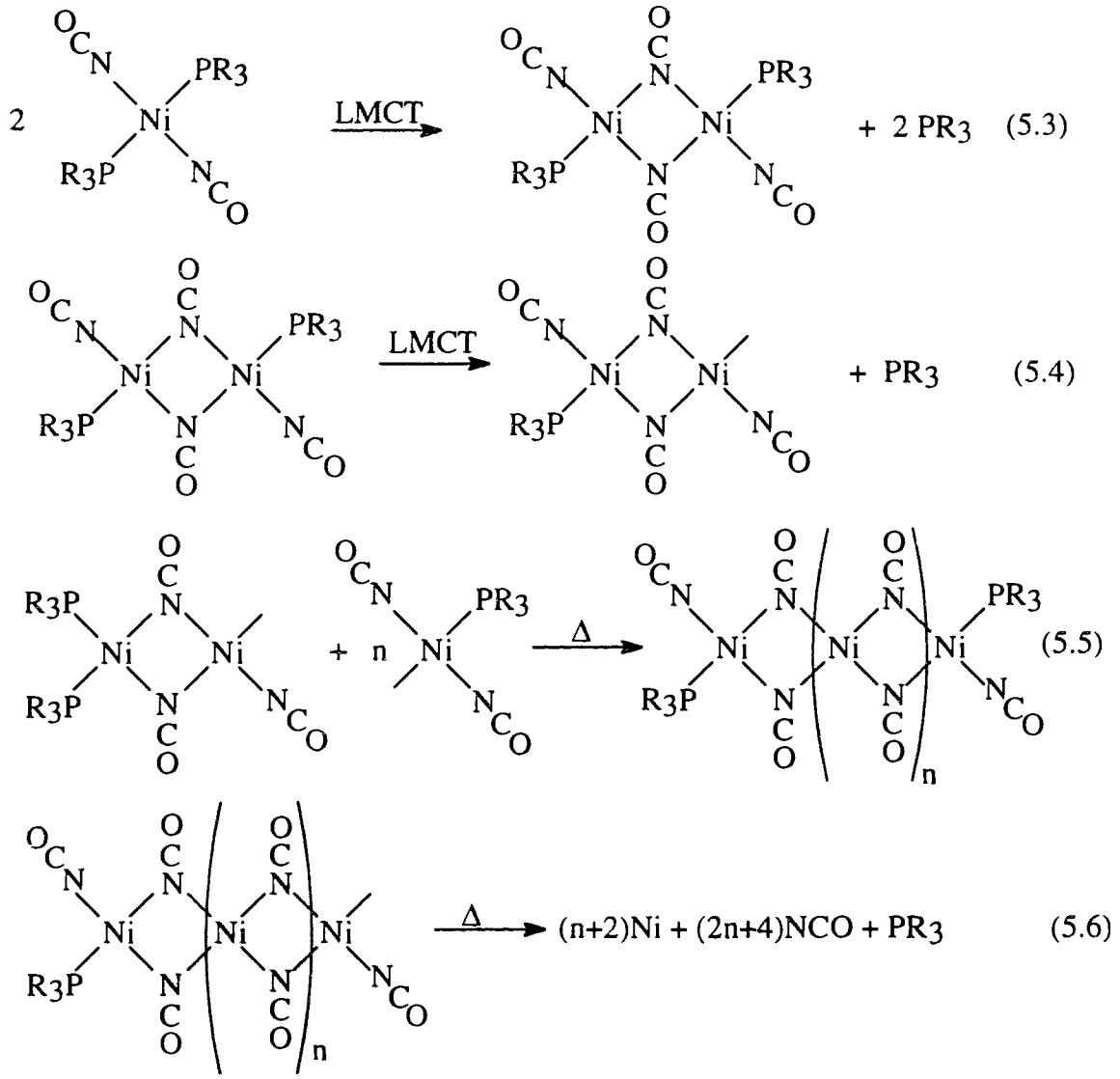

Reactivity analogous to *trans*-$(Bu_3P)_2Ni(NCO)_2$ was observed for *trans*-$(Et_3P)_2Ni(NCO)_2$ upon photolysis with $320 < \lambda < 420$ nm light. A decay in the intensity of the ν(NC) absorption at 2234 cm^{-1} was observed. The bridged photoproduct was

distinguished by the presence of two new FTIR absorption bands, one at 2189 cm^{-1} and a very weak absorption at 1317 cm^{-1}, corresponding to the ν(NC) and the ν(CO) absorption bands respectively. The δ(NCO) absorptions were too weak to observe. Based on these assignments (Table 5.3), the photoreactions of *trans*-$(Et_3P)_2Ni(NCO)_2$ with $320 < \lambda < 420$ nm light are shown in equations 5.3, 5.4, 5.5 and 5.6.

The spectroscopic changes on photolysis of *trans*-$(Bu_3P)_2Ni(NCO)_2$ with 366 nm light only are similar to the changes observed when *trans*-$(Bu_3P)_2Ni(NCO)_2$ was irradiated with $320 < \lambda < 420$ nm (i.e. 334 and 366 nm) light. Upon photolysis of *trans*-$(Bu_3P)_2Ni(NCO)_2$ with 366 nm light, the absorption at 2232 cm^{-1} decayed. An absorption band at 2188 cm^{-1} was observed to grow in and subsequently decay on further photolysis (Fig. 5.6).

Figure 5.6 Spectroscopic changes associated with photolysis of *trans*-$(Bu_3P)_2Ni(NCO)_2$ with 366 nm light. Accumulated photolysis times are: 0, 3.5, 28.5, 47, 50 and 72 hr.

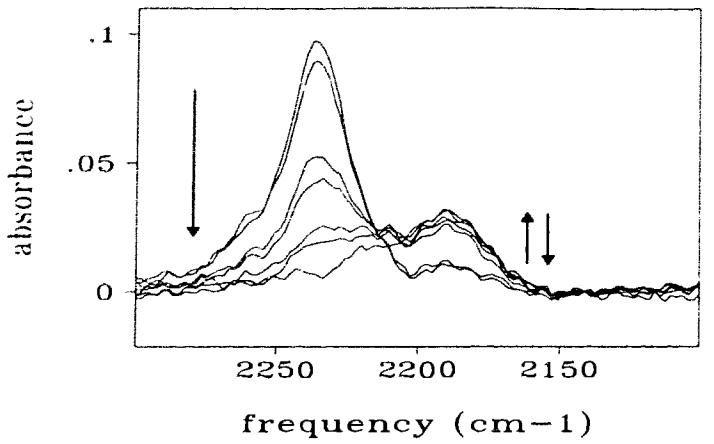

Photolysis of a film of *trans*-$(Et_3P)_2Ni(NCO)_2$ with 366 nm light resulted in the complete decay of the absorption at 2234 cm^{-1}. No evidence for the formation of a thermally stable intermediate was observed (Figure 5.7). The fact that no photoproduct was formed is indicative that different reactivity occurs when *trans*-$(Et_3P)_2Ni(NCO)_2$ is irradiated with 366 nm light than with 334 nm light. The loss of the ν(NC) absorption at 2234 cm^{-1} with no formation of a thermally stable nickel species is consistent with NCO radical loss. The thermally unstable Ni(I) intermediate, $[(Et_3P)_2Ni(NCO)]$, rapidly decomposes (equation 5.7).

Figure 5.7 Spectroscopic changes associated with photolysis of *trans*-$(Et_3P)_2Ni(NCO)_2$ with 366 nm light. Accumulated photolysis times are: 0, 30, 60, 120, 290 and 1140 min.

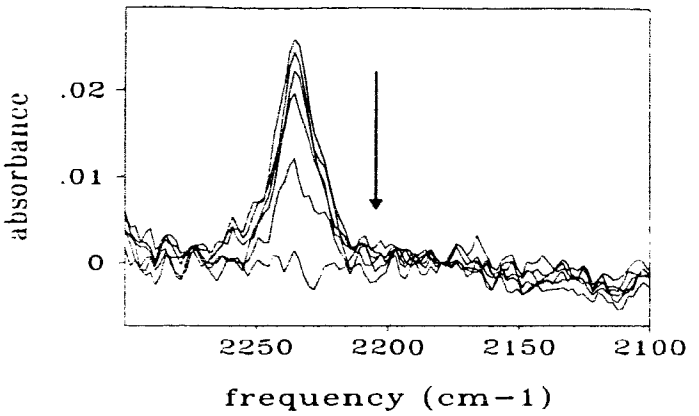

$$\textit{trans}\text{-}(Et_3P)_2Ni(NCO)_2 \xrightarrow{h\nu}$$

$$[(Et_3P)_2Ni(NCO) + \bullet NCO] \xrightarrow{\Delta} Ni + 2PR_3 + 2\bullet NCO \qquad (5.7)$$

R= Et, Bu

5.2.4 Quantum yields for decomposition of the complexes

The efficiency of photodecomposition was determined for each complex when irradiated with 334 nm as well as with 366 nm light. The quantum yields for decomposition of the complexes on silicon are reported in Table 5.4.

Table 5.4 Quantum yields for decomposition of films of the *trans*-$(R_3P)_2M(X)_2$ complexes.

Complex	I_o[a] (366nm) ($Es^{-1}cm^{-2}$)	ε_{366} (cm^2mol^{-1})	Φ_{366} ($\pm \Phi_{366}$)[b]	I_o[a] (334 nm) ($Es^{-1}cm^{-2}$)	ε_{334} (cm^2mol^{-1})	Φ_{334} ($\pm \Phi_{334}$)[b]
$(Et_3P)_2Ni(NO_2)_2$	$7.71x10^{-10}$	$3.24x10^6$	0.00024 ($\pm 1x10^{-5}$)	$4.13x10^{-10}$	$5.26x10^6$	0.008 ($\pm$0.004)
$(Et_3P)_2Ni(NO_2)_2$	$6.12x10^{-10}$	$3.24x10^6$	0.00024 ($\pm 1x10^{-5}$)	--	--	--
$(Bu_3P)_2Ni(NO_2)_2$	$7.72x10^{-9}$	$8.06x10^6$	$9x10^{-5}$ ($\pm 4x10^{-5}$)	$4.13x10^{-9}$	$1.73x10^6$	0.021 ($\pm$0.002)
$(Bu_3P)_2Ni(NO_2)_2$	$1.57x10^{-9}$	$8.06x10^6$	$9x10^{-5}$ ($\pm 4x10^{-5}$)	--	--	--
$(Et_3P)_2Ni(NCS)_2$	$8.49x10^{-9}$	$9.02x10^6$	$1.8x10^{-5}$ ($\pm 3x10^{-6}$)	$4.54x10^{-9}$	$7.71x10^6$	0.0030 ($\pm$0.0003)
$(Et_3P)_2Ni(NCS)_2$	$8.44x10^{-9}$	$9.02x10^6$	$1.8x10^{-5}$ ($\pm 3x10^{-6}$)	--	--	--
$(Et_3P)_2Ni(CN)_2$	$6.10x10^{-9}$	$3.28x10^6$	0.0024 ($\pm$0.0005)	$3.26x10^{-9}$	$3.69x10^6$	-0.0020 ($\pm$0.0004)
$(Et_3P)_2Ni(CN)_2$	$2.97x10^{-9}$	$3.28x10^6$	0.0024 ($\pm$0.0005)	--	--	--
$(Et_3P)_2Pd(NO_2)_2$	$1.00x10^{-8}$	$1.18x10^6$	$5.0x10^{-5}$ ($\pm$0.002)	$5.37x10^{-9}$	$2.59x10^6$	0.001 ($\pm$0.002)
$(Et_3P)_2Pd(NO_2)_2$	$6.12x10^{-9}$	$1.18x10^6$	$5.0x10^{-5}$ ($\pm$0.002)	--	--	--
$(Et_3P)_2Pt(NO_2)_2$	$1.17x10^{-8}$	$1.71x10^6$	0.0005 ($\pm 8x10^{-7}$)	$6.28x10^{-9}$	$1.66x10^6$	0.024 ($\pm$0.003)
$(Et_3P)_2Pt(NO_2)_2$	$3.98x10^{-10}$	$1.71x10^6$	0.0005 ($\pm 8x10^{-7}$)	--	--	--
$(Et_3P)_2Ni(NCO)_2$	$5.16x10^{-9}$	$2.81x10^6$	0.0003 ($\pm$0.0001)	$2.76x10^{-9}$	$5.66x10^6$	0.0132 ($\pm$0.0009)
$(Et_3P)_2Ni(NCO)_2$	$2.66x10^{-9}$	$2.81x10^6$	0.0003 ($\pm$0.0001)	--	--	--
$(Bu_3P)_2Ni(NCO)_2$	$4.41x10^{-9}$	$1.66x10^6$	0.0009 ($\pm$0.0003)	$2.36x10^{-9}$	$8.25x10^6$	0.0054 ($\pm$0.0003)
$(Bu_3P)_2Ni(NCO)_2$	$2.48x10^{-9}$	$1.66x10^6$	0.0009 ($\pm$0.0003)	--	--	--

[a] for band pass 320 $<\lambda<$ 420 nm, the light intensity at 334 and 366 nm was corrected [114].

[b] error calculated from the error in the exponential decay fit (equation 5.8).

The quantum yield of *trans*-$(Et_3P)_2Ni(NO_2)_2$ was determined as follows. A film of the complex was spin coated on p-type Si (100). Upon irradiation of *trans*-$(Et_3P)_2Ni(NO_2)_2$ with band pass 320 <λ< 420 nm light, loss of absorption bands due to the nitrite ligand was observed (Figure 5.3). No evidence for the formation of an intermediate was observed. A plot of absorbance at 1321 cm^{-1} *vs.* photolysis time is shown in Figure 5.8. Irradiation with band pass 320 <λ< 420 nm light allows passage of both 334 nm and 366 nm light. The plot of absorbance *vs.* photolysis time is fit to an exponential decay according to equation 5.8. The rate of decomposition of a film of *trans*-$(Et_3P)_2Ni(NO_2)_2$ on p-type Si (100) in the dark, under vacuum, k_T, was 3 x 10^{-8} s^{-1}. The rate of thermal decomposition was negligible compared to the rate of photochemical decomposition. Therefore, the thermal decay of *trans*-$(Et_3P)_2Ni(NO_2)_2$ (equation 5.9) was neglected in the quantum yield expression (equation 5.8).

Figure 5.8 Plot of absorbance at 1321 cm^{-1} *vs.* photolysis time for the reaction of *trans*-$(Et_3P)_2Ni(NO_2)_2$ on p-type silicon under vacuum, data from Figure 5.3.

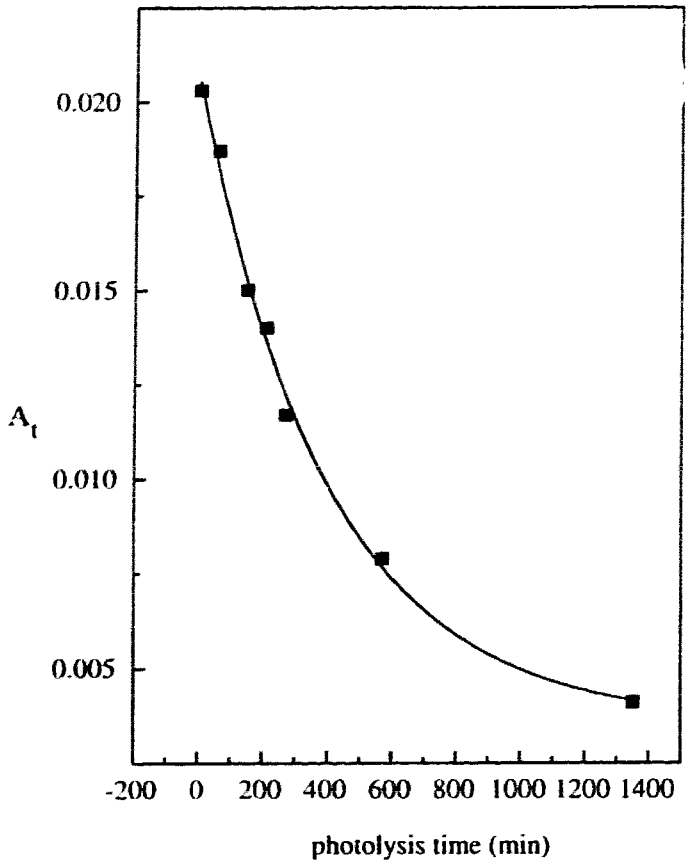

$$A_t = A_o \exp[-(2.303 I_{o(334)} \varepsilon_{334} \Phi_{334} + 2.303 I_{o(366)} \varepsilon_{366} \Phi_{366})(t)] \qquad (5.8)$$

A_t= FTIR absorbance at photolysis time, t
A_o= initial absorbance
Φ_λ= quantum yield for decomposition
$I_{o(\lambda)}$ ($Es^{-1}cm^{-2}$)= incident light intensity
ε_λ (cm^2mol^{-1})= extinction coefficient at irradiation wavelength
λ (nm)= wavelength
t (s)= photolysis time

$$trans\text{-}(Et_3P)_2Ni(NO_2)_2 \xrightarrow{k_T} Ni + 2\,PEt_3 + 2\,\bullet NO_2 \qquad (5.9)$$

There are two unknowns in equation 5.8, Φ_{334} and Φ_{366}. To solve for Φ_{334}, a separate experiment was conducted to independently determine the quantum yield for decomposition with 366 nm light, Φ_{366}.

The quantum yield, Φ_{366}, was determined as follows. Upon irradiation of *trans*-$(Et_3P)_2Ni(NO_2)_2$ with 366 nm light, loss of the $\nu_a(NO_2)$ and $\nu_s(NO_2)$ absorptions at 1375 and 1321 cm^{-1} respectively, was observed. No evidence was found for the formation of an intermediate. A plot of absorbance at 1321 cm^{-1} *vs.* photolysis time was fit to an exponential decay according to equation 5.8. Since only 366 nm light irradiated the sample, $I_{o(334)}$ equals zero. Therefore, the term $2.303I_{o(334)}\varepsilon_{334}\Phi_{334}$ was zero. The incident light intensity at 366 nm, $I_{o(366)}$ was 6.12 x 10^{-10} $Es^{-1}cm^{-1}$ and the extinction coefficient, ε_{366}, is 3.24 x 10^6 cm^2mol^{-1}. The quantum yield for decomposition with 366 nm light, Φ_{366}, was 0.00024 ($\pm 10^{-5}$).

The quantum yield for decomposition with 334 nm light, Φ_{334}, was then determined. The plot of absorbance at 1321 cm^{-1} *vs.* photolysis time was fit to an exponential decay, and converted to the quantum yield, Φ_{334}, by equation 5.8. The incident light intensity, $I_{o(334)}$, was 4.13 x 10^{-10} $Es^{-1}cm^{-2}$ [114] and the extinction coefficient for a film of this complex at 334 nm, ε_{334} is 5.26 x 10^6 cm^2mol^{-1}. The incident light intensity at 366 nm, $I_{o(366)}$ was 7.71 x 10^{-10} $Es^{-1}cm^{-2}$ [114], the extinction coefficient, ε_{366} is 3.24 x 10^6 cm^2mol^{-1}, and Φ_{366} was 0.00024 ($\pm 10^{-5}$). The quantum yield for

decomposition of the film with 334 nm light, Φ_{334}, was 0.008 (±0.004). These results are summarized in Table 5.4.

The photodecomposition of a film of *trans*-$(Et_3P)_2Ni(NO_2)_2$ with 366 nm light is much less efficient than when the complex is irradiated with 334 nm light. The decomposition quantum yield for a film of *trans*-$(Et_3P)_2Ni(NO_2)_2$ irradiated with 366 nm light, Φ_{366} was 0.00024 ($\pm 1 \times 10^{-5}$). The quantum yield for photolysis with 334 nm light, Φ_{334}, was 0.008 (±0.004).

The quantum yields for the decomposition of *trans*-$(R_3P)_2M(X)_2$ (M= Ni, R= Et, X= NO_2, NCO, NCS, CN; M= Pd, Pt, R= Et, X= NO_2; M= Ni, R= Bu, X= NO_2, NCO) are reported in Table 5.4. The quantum yields when the complexes were photolysed with 366 nm light are significantly smaller than when photolysed with 334 nm light.

The quantum yields for decomposition of *trans*-$(Et_3P)_2Ni(CN)_2$ at 334 and 366 nm is reported in Table 5.4. The quantum yield at 334 nm, Φ_{334}, was calculated as -0.0020 (± 0.0001). A quantum yield cannot be negative. This indicates that a competing process occurs at one or both wavelengths (334 and 366 nm). This was not accounted for in the quantum yield expression.

Recall that films of *trans*-$(Et_3P)_2Ni(CN)_2$ had a tendency to crystallize. Although the films appeared amorphous when prepared for a photolysis experiment, the film may have been partially crystallized. This would lead to a reduction in the observed quantum yield, due to recombination of the ejected CN radical with the primary photoproduct, $[Ni(PEt_3)_2(CN)]$, to reform starting material. There is no way to quantify the amount of recombination within the films. Therefore, the quantum yield values for decomposition

of the complex with 334 and 366 nm light (Φ_{334} and Φ_{366} respectively) are not valid.

The quantum yield for decomposition with 334 nm light for *trans*-$(Et_3P)_2Ni(NCO)_2$ and *trans*-$(Bu_3P)_2Ni(NCO)_2$ were 0.0132 (± 0.0009) and 0.0054 (± 0.0003) respectively. The decomposition quantum yields at 366 nm for *trans*-$(Et_3P)_2Ni(NCO)_2$ and *trans*-$(Bu_3P)_2Ni(NCO)_2$ were 0.0003 (± 0.0001) and 0.0009 (± 0.0003) respectively.

5.2.5 Auger analysis

A film of *trans*-$(Et_3P)_2Ni(NO_2)_2$ was photolysed until the $\nu_a(NO_2)$ and $\nu_s(NO_2)$ absorptions at 1375 and 1321 cm^{-1} respectively decayed to baseline. The resultant film was placed in the scanning Auger microprobe for analysis. The results are shown in Table 5.5. The surface of the film contained 21.6% Ni, 44.7% O and 33.7% C. This indicates that the surface of the film was nickel oxide contaminated with carbon. Following a 30 sec sputter with argon ions, the film contained 57.5% Ni, 13.8% O and 28.7% C. Nitrogen and phosphorus were not present. Of most importance was that no signal due to phosphorus was observed throughout the film. This result indicated that the carbon contamination did not originate from the PEt_3 ligand. The source of carbon is presumably from the atmosphere. These results are consistent with photolysis leading to loss of all ligands as shown in equations 5.1, 5.2 and 5.6.

Table 5.5 Auger analysis of films resultant from photolysis of complexes of the formula *trans*-$(R_3P)_2M(X)_2$.

Complex	Sputter Time (sec)	% M[a]	% P[a]	% N[a]	% O[a]	% C[a]	% S[a]
$(Et_3P)_2Ni(NO_2)_2$	0	21.6			44.7	33.7	
	30	57.5			13.8	28.7	
$(Et_3P)_2Ni(NCO)_2$	0	12.3	1.2	3.2	13.9	69.4	
	30	18.5	3.5	2.6	6.5	68.9	
$(Et_3P)_2Ni(NCS)_2$	0	13.4	2.8	2.8	3.7	71.2	6.1
	30	11.5	2.9	3.0	3.4	74.4	4.8
$(Et_3P)_2Ni(CN)_2$	0	21.7	7.0	5.9	26.2	39.8	
	5	37.5	17.4	5.2	9.1	30.7	
$(Et_3P)_2Pd(NO_2)_2$	0	25.9	14.1		18.8	41.3	
	10	30.1	23.5		17.7	28.7	
$(Et_3P)_2Pt(NO_2)_2$	0	38.0	14.8	9.8	21.7	15.7	
	10	60.5	20.4	4.8	5.3	9.0	
$(Bu_3P)_2Ni(NCO)_2$	0	17.1	6.2	4.6	21.2	50.9	
	5	28.3	17.5	2.6	3.7	47.9	
$(Bu_3P)_2Ni(NO_2)_2$	0	28.0	5.0		21.7	45.3	
	10	35.5	11.6		3.0	49.9	

[a] error approximately 5 atom% [85]

Auger analysis was conducted on all films resultant from the photolysis experiments. Films produced by photolysis of all the complexes in Table 5.5 except for *trans*-$(Et_3P)_2Ni(NO_2)_2$ contained phosphorus, carbon and oxygen. For example, a film after photolysis of *trans*-$(Et_3P)_2Ni(NCO)_2$, contained 12.3% Ni, 1.2% P, 3.2% N, 13.9% O and 69.4% C. The Ni: P ratio is approximately 10: 1, which indicates that most of the PEt_3 is ejected on photolysis, however some PEt_3 remained trapped in the film. Nitrogen was also found in the film, indicating that the isocyanate ligand was not completely removed from the film.

5.2.6 Lithography

The compound *trans*-$(Et_3P)_2Ni(NO_2)_2$ exhibited the most promise to produce metal films *via* photodecomposition of an amorphous film of the compound. It decomposes with a single photon mediated process, and surface analysis following photolysis detected no traces of nitrogen or phosphorus.

In order to demonstrate the compatibility of the process of photolysing amorphous films of inorganic complexes with current lithographic techniques a film of *trans*-$(Et_3P)_2Ni(NO_2)_2$ was photolysed through a lithography mask which was in contact with the surface. Following photolysis the sample was rinsed with acetone to remove the unexposed portion of the film. In Figure 5.9 a scanning electron micrograph of the resultant pattern is shown. A clear pattern of five lines, each 3.5 μm wide and separated by 3.5 μm is observed.

Figure 5.9 Scanning electron micrograph of a surface obtained by the photolithography of *trans*-$(Et_3P)_2Ni(NO_2)_2$ films on a Si (111) surface.

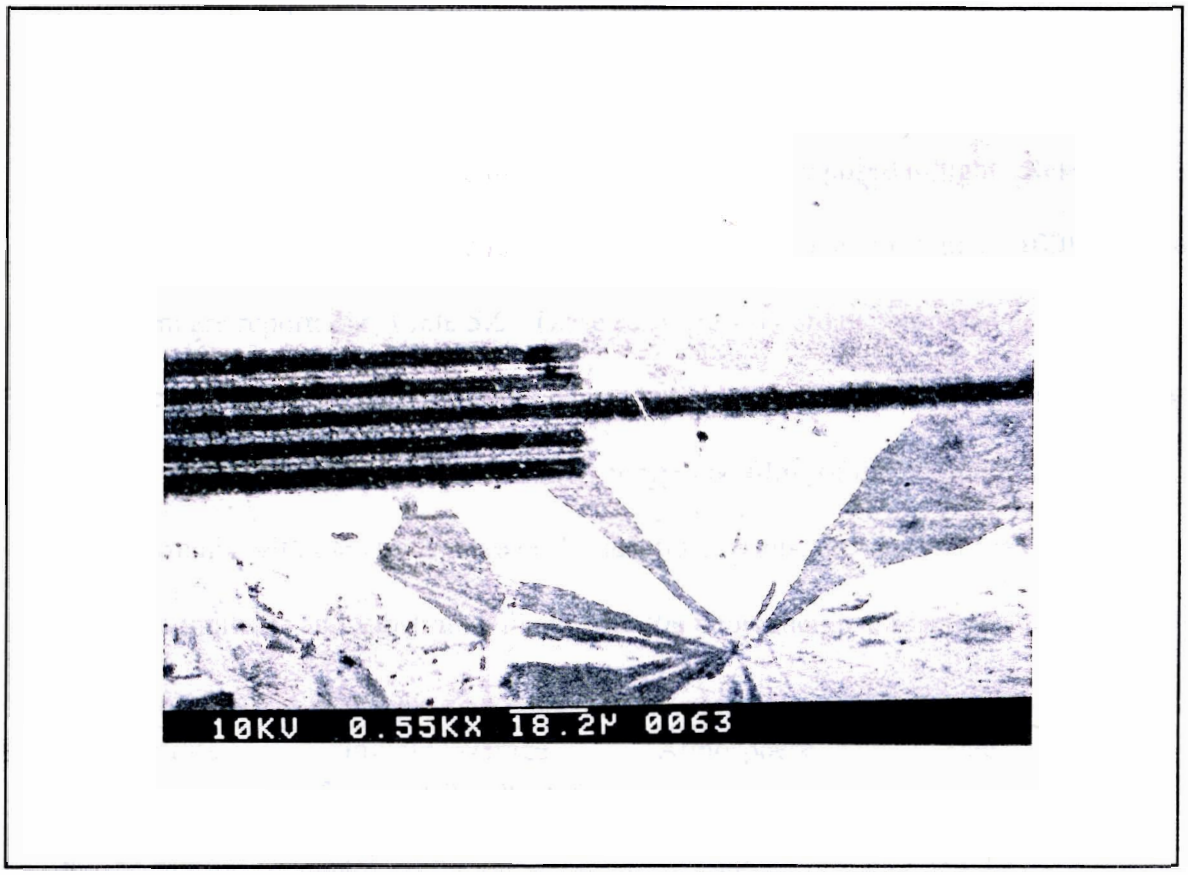

5.2.7 Photoefficiency of decomposition of trans-$(Et_3P)_2Ni(NO_2)_2$ as a function of substrate and atmosphere

The compound *trans*-$(Et_3P)_2Ni(NO_2)_2$ demonstrated the most promise to produce a metal or metal oxide film of the series of complexes studied in this chapter. Therefore, it was selected as the example for the study of photoefficiency as a function of substrate and atmosphere. The rate of decomposition for the compound in the dark under vacuum is negligible compared to the rate of decomposition when exposed to light. Results of thermal decomposition rates for *trans*-$(Et_3P)_2Ni(NO_2)_2$ on p- and n-type Si(100) in air and in vacuum are reported in Table 5.6. These rates are very small compared to rates of photodecomposition and can therefore be neglected in the calculation of quantum yields (equation 5.8). These results indicate that amorphous films of the compounds do not react thermally with the atmosphere or the substrate. Thus, the study of the effect of reaction conditions and substrate will apply to the photochemical reactions only.

Table 5.6 Thermal decomposition rates for amorphous films of *trans*-$(Et_3P)_2Ni(NO_2)_2$.

Substrate	Initial Coverage (A_o)	(monolayers)	Atmosphere	Rate (s^{-1})
n-type Si (100)	0.016	39	vacuum[a]	3.9×10^{-8}
n-type Si (100)	0.003	7	air	1.0×10^{-8}
p-type Si (100)	0.012	29	vacuum[a]	3.1×10^{-8}

[a]approximately 1 torr

To investigate the photoefficiency of decomposition of inorganic molecules as thin films, it is necessary to determine whether the reactions involved are truly molecular in nature. This means we must determine whether the photoreactions are induced or altered by the substrate or the reactive atmosphere. Therefore, experiments were performed in which the substrate was varied.

To investigate the possibility of interfacial chemistry being important in the reaction, the photoefficiency of decomposition of *trans*-$(Et_3P)_2Ni(NO_2)_2$ on various surfaces was measured. Three substrates were chosen, two semiconductors of different carrier doping, and an insulating surface. The substrates chosen were p- and n-type silicon, and CaF_2.

The quantum yield of decomposition with 334 nm light, Φ_{334}, for *trans*-$(Et_3P)_2Ni(NO_2)_2$ was determined as described in *Section 5.2.4*. The plot of absorbance at 1321 cm^{-1} *vs.* photolysis time (Figure 5.8) was fit to an exponential decay and converted to the quantum yield, Φ_{334}, by equation 5.8. The quantum yield, Φ_{334}, for decomposition of the complex on p-type Si(100) under vacuum (approx. 1 torr) was 0.008 (±0.004).

The quantum yield Φ_{334}, for decomposition of *trans*-$(Et_3P)_2Ni(NO_2)_2$ on n-type Si(100) under vacuum was also determined. The incident light intensity, $I_{o(334)}$, was 4.13 x 10^{-10} $Es^{-1}cm^{-2}$ [114] and the extinction coefficient for a film of this complex at 334 nm, ε_{334} is 5.26 x 10^6 cm^2mol^{-1}. The incident light intensity at 366 nm, $I_{o(366)}$ was 7.71 x 10^{-10} $Es^{-1}cm^{-2}$ [114], the extinction coefficient, ε_{366} is 3.24 x 10^6, and Φ_{366} was 0.00024 (±1 x 10^{-5}). The quantum yield for decomposition of the film with 334 nm light, Φ_{334}, was 0.0096 (±0.0008). These results are summarized in Table 5.7.

Table 5.7 Quantum yield results for decomposition of *trans*-$(Et_3P)_2Ni(NO_2)_2$ with 334 nm light[a] on various surfaces.

Substrate	Atmosphere	Quantum Yield[b] ($\Phi_{334} \pm \Phi_{334}$[c])
n-type Si(100)	vacuum[d]	0.010 (± 0.008)
n-type Si(100)	air	0.01 (± 0.01)
p-type Si(100)	vacuum[d]	0.008 (± 0.004)
p-type Si(100)	air	0.009 (± 0.001)
CaF_2	vacuum[d]	0.007[e] (± 0.003)
CaF_2	air	0.007[e] (± 0.006)

[a]the Hg light source was filtered $320 < \lambda < 420$ nm and the light intensity was corrected for 334 nm and 366 nm [114]

[b]calculated from equation 5.8: $\varepsilon_{334} = 5.26 \times 10^6$ cm^2mol^{-1}, $\varepsilon_{366} = 3.24 \times 10^6$ cm^2mol^{-1}, $I_{o(334)} = 4.13 \times 10^{-10}$ $Es^{-1}cm^{-2}$, $I_{o(366)} = 7.71 \times 10^{-10}$, $\Phi_{366} = 0.00024$ ($\pm 1 \times 10^{-5}$).

[c]calculated from the error in the rate constant from exponential decay fit

[d]approx 1 torr

[e]corrected for reflectivity by dividing $I_{o(334)}$ and $I_{o(366)}$ by two.

The quantum yield for decomposition, Φ_{334}, of a film of *trans*-$(Et_3P)_2Ni(NO_2)_2$ on CaF_2, under vacuum was 0.007 (± 0.003) (see Table 5.7). When the substrate was CaF_2, the light intensity was corrected for the reflectivity of silicon by dividing the light intensity by two.

Silicon reflects UV light, allowing for light to pass through the film at least twice (exactly twice if perfectly reflected), whereas the CaF_2 substrate transmits the light allowing only single passage. Logic suggests that the light intensity of experiments with silicon substrates should be corrected. However, we do not have a reliable correction factor for the amount of reflectance that occurs. Silicon is predominantly used as the substrate for quantum yield determinations. Rather than adding a new factor into the

quantum yield expression (equation 5.8), dividing the light intensity by two for CaF_2 surfaces, allows us to compare approximately the effect of the substrates on the quantum yield. The results indicate that, apart from the reflectivity of the silicon, the substrate does not influence the photoreaction of the molecule.

The results of the decomposition quantum yield, Φ_{334}, of *trans*-$(Et_3P)_2Ni(NO_2)_2$ on various substrates are presented in Table 5.7. The quantum yields for *trans*-$(Et_3P)_2Ni(NO_2)_2$ on p-type Si(100), n-type Si(100) and CaF_2 surfaces are not significantly different. This indicates that the substrates do not affect the decomposition of the complex.

The formation of oxygen sensitive intermediates may result in changes in the efficiency of reaction. Previous studies have shown that the production of oxygen sensitive intermediates which are thermally stable result in the measurement of different apparent quantum yields in air and vacuum [97]. This effect was also reported for the solid state photodecomposition reaction of *trans*-$Fe(CO)_3(PPh_3)_2$ in Chapter 3.

The effect of atmospheric conditions on the photoefficiency of these reactions was also studied and the results are reported in Table 5.7. The quantum yield for decomposition of *trans*-$(Et_3P)_2Ni(NO_2)_2$ with 334 nm light, Φ_{334}, on p-type Si(100) under vacuum was 0.008 ($\pm$ 0.004). The quantum yield for this complex on p-type Si(100) in air was 0.009 ($\pm$ 0.001). No significant difference was observed when the experiment was conducted in air or in vacuum. Quantum yields, Φ_{334} for films of *trans*-$(Et_3P)_2Ni(NO_2)_2$ in air were 0.01 ($\pm$0.01) on n-type Si(100) and 0.007 ($\pm$ 0.006) on CaF_2. There was no significant difference between the quantum yields determined in air or in

vacuum. This indicates that oxygen sensitive intermediates are not formed in the photodecomposition reaction.

5.3 Discussion

The spectroscopic data for the complexes studied in this chapter indicate that all have the *trans*-planar configuration. The molecular orbital (MO) diagrams for d^8 *trans*-planar molecules in the ground and excited states are illustrated in Figure 5.1. Irradiation of complexes of the formula *trans*-$(R_3P)_2M(X)_2$ (M= Ni, R= Et, X= NO_2, NCS; CN M= Pd, Pt, R= Et, X= NO_2; M= Ni, R= Bu, X= NO_2) with either 334 nm or 366 nm light leads to loss of all ligands with no evidence of a stable intermediate. When *trans*-$(Bu_3P)_2Ni(NCO)_2$ is irradiated with either 334 nm or 366 nm light a thermally stable, photosensitive product is observed. Photolysis of the complex *trans*-$(Et_3P)_2Ni(NCO)_2$ yields a thermally stable, photosensitive product with 334 nm light. Irradiation of *trans*-$(Et_3P)_2Ni(NCO)_2$ with 366 nm light leads to loss of all ligands with no evidence for a thermally stable intermediate. A look at the electronic configurations of the molecules will help elucidate the mechanisms for these reactions.

All of the compounds studied in this chapter have similar ground state electronic configurations. Figure 5.1 a) illustrates the orbital occupation of the d-orbitals for the molecules. If the field is effectively D_{2h} and the primary axis is perpendicular to the ligands, the highest occupied d-orbital is the d_{Z^2} orbital. It should be noted that although the d_{XZ} and d_{YZ} orbitals are illustrated as degenerate, the d_{XZ} orbital is slightly lower in energy. The three d-d transitions are shown in Figure 5.1 b). The lowest energy d-d

transition is $d_{z^2} \rightarrow d_{x^2-y^2}$. This is very weak and not observed. The next absorption is the $d_{xz,yz} \rightarrow d_{x^2-y^2}$ transition, however it overlaps the more intense charge transfer aborption bands. This represents transitions consistent with $A_g \rightarrow B_{2g}$ and $A_g \rightarrow B_{3g}$. The D_{2h} character table is shown in Table 5.8. According to the symmetry of the orbitals, all the d-d absorptions are forbidden, however the splitting of the d_{xz} and d_{yz} orbitals leads to vibronically induced transitions which are observed in the electronic absorption spectrum [112] (Table 5.1).

Table 5.8 The D_{2h} character table

D_{2h}	E	$C_{2(z)}$	$C_{2(y)}$	$C_{2(x)}$	i	σ_{xy}	σ_{xz}	σ_{yz}		
A_g	1	1	1	1	1	1	1	1		x^2,y^2,z^2
B_{1g}	1	1	-1	-1	1	1	-1	-1	R_z	xy
B_{2g}	1	-1	1	-1	1	-1	1	-1	R_y	xz
B_{3g}	1	-1	-1	1	1	-1	-1	1	R_x	yz
A_u	1	1	1	1	-1	-1	-1	-1		
B_{1u}	1	1	-1	-1	-1	-1	1	1	z	
B_{2u}	1	-1	1	-1	-1	1	-1	1	y	
B_{3u}	1	-1	-1	1	-1	1	1	-1	x	

The lowest energy LMCT transition is expected to be $A_g \rightarrow B_{2u}$ which represents a configuration consistent with $(b_{2u}^2\ a_g^0)$ for the ground state and $(b_{2u}^1\ a_g^1)$ for the excited state. In terms of orbitals this corresponds to $\pi_y(X) \rightarrow d_{x^2-y^2}$ (M) (see Figure 5.1 c)). The $\pi(X)$ orbital for $X=NO_2^-$, is illustrated in Figure 5.10. The p_y orbital of the Ni overlaps the symmetric pi bonding system of the two NO_2^- ligands (Fig. 5.10 a)). This orbital has b_{2u} symmetry. It should be noted that the antisymmetric pi-bonding system of the NO_2^- ligand is close in energy to the symmetric pi-bonding system. The antisymmetric pi-bonding sytem of NO_2^- overlaps the d_{xy} (b_{1g} symmetry) orbital of nickel (Fig. 5.10 b)).

An LMCT excited state of this symmetry $A_g \rightarrow B_{1g}$ would have a higher energy than the $A_g \rightarrow B_{2u}$ excited state (see Figure 5.11).

Figure 5.10 The a) b_{2u} and b) b_{1g} NO_2^- π ligand orbitals.

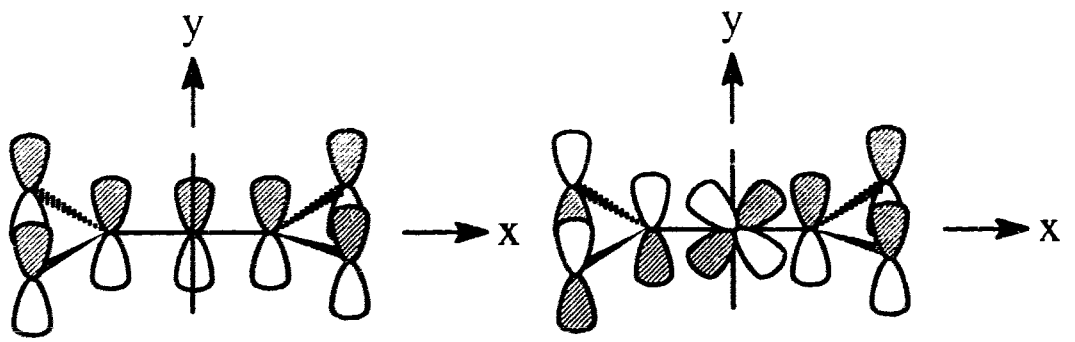

a) b_{2u} b) b_{1g}

Irradiation into the $A_g \rightarrow B_{2u}$ LMCT excited state (Fig. 5.1 c)) would be expected to eject the anionic ligand, X, as the radical. This is the reaction observed when all compounds except for *trans*-$(R_3P)_2Ni(NCO)_2$ (R= Et, Bu) were irradiated with 334 nm light and *trans*-$(Bu_3P)_2Ni(NCO)_2$ was irradiated with 366 nm light (equation 5.10).

$$\textit{trans}\text{-}(R_3P)_2M(X)_2 \xrightarrow{\text{LMCT}}$$

$$[(R_3P)_2M(X) + X\bullet] \xrightarrow{\Delta} M + 2\,PR_3 + 2\,X\bullet \qquad (5.10)$$

M= Ni, R= Et, X= NO_2, NCS; CN (λ= 334, 366 nm);

M= Pd, Pt, R= Et, X= NO_2 (λ= 334 nm, 366 nm);

M= Ni, R= Bu, X= NO_2 (λ= 334 nm, 366 nm);

M= Ni, R= Et, X= NCO (λ= 366 nm)

When all complexes except *trans*-$(Bu_3P)_2Ni(NCO)_2$ were irradiated with 366 nm light only, loss of all ligands was observed and no evidence for the formation of an intermediate was observed. The LMCT absorption band is broad in all cases and overlaps into the 366 nm region. Thus the primary photoreaction observed was also the ejection of the anionic ligand as a radical. This was followed by rapid thermal decomposition of the M(I) fragment (see equation 5.10). The only complex which exhibited different reactivity with 366 nm light was *trans*-$(Bu_3P)_2Ni(NCO)_2$. The photoreactions of this complex will be discussed in the following paragraphs.

When *trans*-$(R_3P)_2Ni(NCO)_2$ (R= Et, Bu) were irradiated with band pass 320 $<\lambda<$ 420 nm light a photoproduct was observed. Irradiation of *trans*-$(Bu_3P)_2Ni(NCO)_2$ with 366 nm light also resulted in a molecular photoproduct. However, irradiation of *trans*-$(Et_3P)_2Ni(NCO)_2$ with 366 nm light alone led to loss of all ligands with no observable intermediates. The photochemistry of *trans*-$(Et_3P)_2Ni(NCO)_2$ will be described first.

Two different excited states are responsible for reactivity with 334 nm and with 366 nm light for the complex *trans*-$(Et_3P)_2Ni(NCO)_2$. At the lower energy (366 nm), excitation into the lowest energy LMCT absorption results in the ejection of the anionic ligand as a radical. This is followed by rapid thermal decomposition of the Ni(I) fragment (equation 5.10).

At higher energy (334 nm) the next LMCT absorption for *trans*-$(Et_3P)_2Ni(NCO)_2$ is expected to be $A_g \rightarrow B_{3u}$. This transition represents a configuration consistent with $(b_{3u}^2 a_g^0)$ for the ground state and $(b_{3u}^1 a_g^1)$ for the excited state. In terms of orbitals this corresponds to the ligand P (p_y) to Ni ($d_{x^2-y^2}$) orbital. For the complex *trans*-

$(Bu_3P)_2Ni(NCO)_2$, irradiation with 334 nm and with 366 nm the same LMCT absorption is responsible for decomposition.

Irradiation of *trans*-$(R_3P)_2Ni(NCO)_2$ (R= Et, Bu) into the $P(p_y)\rightarrow Ni\ (d_{x^2-y^2})$ LMCT absorption band results in the ejection of the PR_3 ligand (see equation 5.3). This Ni(II) fragment is sufficiently reactive to dimerize with another Ni(II) photoproduct (equation 5.4). This photoproduct is also photosensitive losing a PR_3 ligand (equation 5.5) and reacting with another Ni(II) fragment, or decomposing thermally (equation 5.6). The FTIR spectra of the photoproduct(s) show that only bridging NCO ligands are present, however there are two terminal NCO ligands. This can be rationalized by equations 5.3, 5.4, 5.5 and 5.6. The ratio of bridged-to-terminal NCO increases as the reaction progresses, and a low, steady state concentration of terminal NCO is present which is obscured by the absorption of the starting material.

The same excited state was responsible for the photolysis of *trans*-$(R_3P)_2M(X)_2$ (M= Ni, R= Et, Bu, X= NO_2, NCS, CN; M= Pd, Pt, R=Et, X= NO_2; M= Ni, R= Bu, X= NO_2). However, a wavelength dependence was observed for the quantum yields for decomposition. At higher energy (334 nm), the quantum yields were significantly higher than that at lower energy (366 nm) (Table 5.4). This can be rationalized by the greater overlap of nonreactive d-d absorption bands at lower energy. This results in a greater portion of the light absorbed that does not lead to decomposition and therefore results in a lower quantum yield.

The photoefficiency of decomposition of *trans*-$(Et_3P)_2Ni(NO_2)_2$ was invariant with the substrate as well as the atmosphere. This indicates that the photoreactions

observed were a result of the molecules in the film and were not influenced by the nature of the interfaces such as the film-substrate and the film-vacuum interfaces.

The quantum yields for decomposition of *trans*-$(R_3P)_2M(NO_2)_2$ (M= Pt, R= Et; M= Ni, R= Bu) were the highest of all the complexes. The quantum yield for decomposition of *trans*-$(R_3P)_2M(NO_2)_2$, was 0.024 (±0.003) for M= Pt, R= Et, and 0.021 (±0.003) for M= Ni, R= Bu. The quantum yields for decomposition of *trans*-$(Et_3P)_2M(X)_2$ with 334 nm light, Φ_{334}, were 0.0030 (± 0.0003) for M= Ni, X= NCS and 0.001 (± 0.002) for M= Pd, X= NO_2. A large error is associated with the quantum yield, Φ_{334}, for *trans*-$(Et_3P)_2Pd(NO_2)_2$. Perhaps significant recombination of the M(I) fragment with the ejected $\bullet NO_2$ radical occurs due to a partially crystalline film.

The quantum yield, Φ_{334}, for decomposition of *trans*-$(Et_3P)_2Ni(CN)_2$ was not valid (-0.0020 ±0.0004). This indicates that a reaction pathway has not been taken into account in the quantum yield expression (equation 5.8). Recall that it was difficult to deposit an amorphous film of *trans*-$(Et_3P)_2Ni(CN)_2$ on silicon, due to crystallization. Attempts were made to minimize crystallization of the films by utilizing dilute solutions for spin coating and fast spin-speeds. However, the films that were deposited may have partially crystallized. Photolysis of a crystalline (or partially crystalline) film would reduce the efficiency of photodecomposition. The reduction in efficiency is caused by recombination of the photoejected $\bullet CN$ radical with the Ni(I) photoproduct. Unless the amount of recombination is reproducible between experiments, the Φ_{366} term cannot be used in equation 5.8 to determine Φ_{366}. Therefore, neither the Φ_{334} nor the Φ_{366}

calculated for *trans*-$(Et_3P)_2Ni(CN)_2$ are valid.

This system was demonstrated to be compatible with current lithography techniques. Formation of 3.5 x 50 μm lines was made on silicon by photolysing a film of *trans*-$(Et_3P)_2Ni(NO_2)_2$ through a lithography mask. Auger analysis of a film following photolysis of *trans*-$(Et_3P)_2Ni(NO_2)_2$ indicated that the product of photolysis contains nickel, oxygen and carbon. If the desired application requires carbon-free films, a further processing step would be necessary.

5.4 Conclusions

A single photon mediated decomposition of square planar molecules of Ni, Pd, and Pt was observed for the complexes *trans*-$(R_3P)_2M(X)_2$ (M= Ni, R= Et, X= NO_2, NCS, CN; M= Pd, Pt, R= Et, X= NO_2; M= Ni, R= Bu, X= NO_2) with 334 nm light. The complexes *trans*-$(R_3P)_2Ni(NCO)_2$ (R = Et, Bu), required additional photon(s) to decompose the bridging photoproduct. These complexes, when deposited as amorphous films can be photochemically converted to films of nickel, palladium or platinum in an entirely solid state process. Photolysis of *trans*-$(Et_3P)_2Ni(NO_2)_2$ resulted in complete removal of phophorus and nitrogen from the film. For the remaining complexes studied in this chapter, phosphorus and carbon remain as impurity problems. An alternate choice of more volatile ligands would be preferable.

Lithography experiments indicated that this method of metal or metal oxide deposition is compatible with current lithography techniques. This was demonstrated by

the deposition of 3.5 by 50 μm lines of product material from lithography of a *trans*-$(Et_3P)_2Ni(NO_2)_2$.

The photochemistry of *trans*-$(Et_3P)_2Ni(NO_2)_2$ was shown to be a truly molecular process. The quantum yield for decomposition of this complex was invariant with substrate. Therefore no chemically important electron transfer occurs across the film-substrate interface.

5.5 Experimental details

5.5.1 Instruments and materials

The silicon wafers were obtained from Pacific Microelectronics Center, Canada. Si(100) surfaces were used in these experiments, and the wafers were both n- and p- type silicon with tolerances and specifications as per SEMI Standard M1.1.STD.5. The wafers were cut to the approximate dimensions of 10 x 12 mm in our laboratory. The NaCl and CaF_2 crystals were obtained from Wilmad Glass Co. Inc.

The samples were mounted in a NaCl faced anodized aluminum vacuum chamber. The Fourier transform infrared (FTIR) spectra were obtained with 4 cm^{-1} resolution using a Bomem Michelson 120 FTIR spectrometer.

The irradiation source for all quantum yield determinations was an Osram 100 W high pressure mercury lamp in an Oriel housing equipped with condenser lenses and filtered through a 10 cm water filter with quartz optics. For quantum yield determinations a filter (band pass $320 < \lambda < 420$ nm) was used to ensure passage of primarily the 334 nm Hg line. To isolate the 366 nm Hg line, an additional filter was added (band pass $\lambda > 350$

nm). The intensity of the light source was measured using an International Light IL 1350 radiometer. The light source for lithography experiments was a 75 W high pressure xenon lamp.

Auger electron spectra were obtained using a PHI double pass cylindrical mirror analyzer (CMA) at 0.85 eV resolution at the Surface Physics Laboratory at Simon Fraser University. Scanning electron micrographs were obtained using an ETEC Corp. Autoscan U1 microscope in the Department of Biological Sciences, Simon Fraser University.

5.5.2 Preparation of the complexes

The complexes *trans*-$(R_3P)_2M(X)_2$; (M= Ni, R= Et, X= NO_2, NCS, CN; M= Pd, Pt, R= Et, X= NO_2; M= Ni, R= Bu, X= NO_2) were prepared following literature procedures [106, 115, 116, 117, 118]. The complexes, *trans*-$(R_3P)_2Ni(NCO)_2$ (R= Et, Bu) were prepared following the procedure for *trans*-$((Et_2Ph)P)_2Ni(NCO)_2$ [118] as follows. The complex *trans*-$(Et_3P)_2Ni(NCO)_2$ was prepared by dissolving 0.0016 mol KOCN in water and adding this solution to an aqueous solution of 0.0008 mol $NiSO_4 \cdot 6H_2O$. The solution was filtered and then treated with 0.29 ml PEt_3. The product precipitated immediately and was filtered. The precipitate was dissolved in ethanol, and the solution was evaporated to dryness. The complexes were characterised by elemental analysis and FTIR and electronic absorption spectroscopy. The elemental analysis data are reported in Table 5.9. The spectroscopic data for the complexes are summarized in Table 5.1.

Table 5.9 Elemental analysis for complexes of the formula $(R_3P)_2M(X)_2$ (M= Ni, R= Et, X= NO_2, CN, NCS, NCO; M= Pd, Pt, R= Et, X= NO_2; M= Ni, R= Bu, X= NO_2, NCO).

Complex	% C found (calcd)	% H found (calcd)	% N found (calcd)
$Ni(PEt_3)_2(NO_2)_2$	37.54 (37.24)	7.02 (7.24)	7..89 (7.81)
$Pd(PEt_3)_2(NO_2)_2$	33.40 (33.15)	6.69 (6.95)	6.25 (6.45)
$Pt(PEt_3)_2(NO_2)_2$	27.69 (27.54)	5.83 (5.78)	5.57 (5.35)
$Ni(PEt_3)_2(CN)_2$	48.19 (48.45)	8.67 (8.71)	7.95 (8.07)
$Ni(PEt_3)_2(NCS)_2$	40.95 (40.89)	7.47 (7.35)	6.77 (6.81)
$Ni(PEt_3)_2(NCO)_2$	44.30 (44.36)	7.98 (7.98)	7.49 (7.39)
$Ni(PBu_3)_2(NCO)_2$	57.19 (57.05)	9.93 (9.94)	5.21 (5.12)
$Ni(PBu_3)_2(NO_2)_2$	52.14 (51.88)	9.71 (9.81)	5.31 (5.05)

5.5.3 Calibration of absorption on Si surfaces

A stock solution of *trans*-$(Et_3P)_2Ni(NO_2)_2$ (0.0016 g) was prepared in CH_2Cl_2 (4.0 ml). A drop (0.0045 ml) of this solution was then deposited on the surface of a silicon chip. The solvent was allowed to evaporate and the FTIR spectrum was obtained. This area of the drop was found to be 0.79 cm^2. This corresponds to a coverage of 1.12 molecules per $Å^2$. This process was repeated several times and a plot of absorbance *vs.* coverage was made and found to be linear. The FTIR spectra and the corresponding plot of absorbance at 1321 cm^{-1} *vs.* coverage is shown in Figure 5.2. The IR extinction coefficient, ε_{IR}, which is the slope of this plot, is 0.022 $Å^2$molecule^{-1}. This procedure was followed for all compounds to quantify the surface coverage of the films. The IR extinction coefficients for the complexes are reported in Table 5.2.

The molar extinction coefficients, ε_{UV}, for a film of *trans*-$(Et_3P)_2Ni(NO_2)_2$ were calculated. The extinction coefficient for this complex at 366 nm is calculated using the ratio of the absorbance at 366 nm, 0.0698, to FTIR absorbance at 1321 cm^{-1}, 0.0286, of a film on CaF_2. This ratio, 2.44, is multiplied by the IR extinction coefficient, ε_{IR}, converted to the units cm^2mol^{-1} (1.32×10^6 cm^2mol^{-1}). This procedure was followed for each compound and the extinction coefficients at 334 and 366 nm are summarized in Table 5.4.

5.5.4 Photolysis of complexes as thin films on silicon and CaF_2 surfaces

All photolysis experiments were done following the same procedure. A typical experiment is as follows. A film of *trans*-$(Et_3P)_2Ni(NO_2)_2$, was deposited on p-type Si (100) by dispensing a drop of a CH_2Cl_2 solution of the complex onto a spinning Si chip. This resulted in the formation of a uniform coating of the complex as an amorphous film. The chip was then transferred to an anodized aluminum sample holder within a vacuum chamber. The system was placed under vacuum (approx. 1 torr), then placed in the IR beam and an FTIR spectrum was obtained. The absorbance of the $\nu_S(NO_2)$ band at 1321 cm^{-1} was recorded, and was denoted A_o. The sample was then irradiated for 60 min and the FTIR spectrum obtained again. This procedure was repeated for the following cumulative photolysis times: 150, 210, 570 and 1350 min. The resultant spectra are shown in Figure 5.3.

5.5.5 Decomposition quantum yield measurements

The quantum yield for decomposition is defined as the moles of compound reacted over the moles of photons absorbed. Quantum yield determinations were made as follows. A plot of absorbance of the $\nu_S(NO_2)$ band for *trans*-$(Et_3P)_2Ni(NO_2)_2$ *vs.* photolysis time with band pass 320 <λ< 420 nm was made and fit to an exponential decay according to equation 5.8. This plot is shown in Figure 5.8. To solve for Φ_{334} according to equation 5.8, we need, $I_{o(334)}$, $I_{o(366)}$, ε_{334}, ε_{366}, and Φ_{366}. The extinction coefficients, ε_{334} and ε_{366}, are 5.26 x 10^6 cm^2mol^{-1} and 3.24 x 10^6 cm^2mol^{-1} respectively. The light intensity at 334 nm and 366 nm was determined as follows.

The light intensity was measured by removing the exit window of the empty vacuum chamber. The intensity of the light source for band pass 320 < λ < 420 nm was 0.4 mW/cm^2. Both 334 and 366 nm Hg lines are emitted under these conditions, therefore a correction factor was made. This correction was based on the relative intensities of the two wavelengths from the spectral output of the light source [114]. The spectral output of an Oriel model 6281 100 W high pressure mercury lamp is 14 μWcm^2nm at 334 nm, and 8.2 μWcm^2nm at 366 nm. The output ratio of 366 nm/ 334 nm is 1.71. From this ratio, we determined that approximately 37% of the intensity measured with band pass 320 < λ < 420 nm is attributed to the 334 nm Hg line (63% from the 366 nm line). Thus, the photon output at 334 nm ($I_{o(334)}$) with 0.4 $mWcm^2$ intensity was calculated as 4.13 x 10^{-10} $Es^{-1}cm^{-2}$, and $I_{o(366)}$ was 7.71 x 10^{-10} $Es^{-1}cm^{-2}$. The output of the light source was found to be constant (within error ca. 10%) by periodic

measurement of intensity between experiments. When band pass $350 < \lambda < 420$ nm was used, only the 366 nm Hg line is emitted, therefore no correction was necessary.

Two unknowns remain to solve for Φ_{334}. The quantum yield at 366 nm, Φ_{366}, was determined independently. A sample of *trans*-$(Et_3P)_2Ni(NO_2)_2$ was photolysed with $350 < \lambda < 420$ nm light allowing passage of 366 nm light only. The photolysis was monitored by the decay of intensity of the 1321 cm^{-1} absorption. The absorbance was plotted against photolysis time and this data was fit to the exponential decay according to equation 5.8. The term $2.303I_{o(334)}\varepsilon_{334}$ is zero for this experiment. the light intensity at 366 nm was 6.12×10^{-10} $Es^{-1}cm^{-2}$ and ε_{366} is 3.24×10^6 cm^2mol^{-1}. The quantum yield for decomposition of *trans*-$(Et_3P)_2Ni(NO_2)_2$ with 366 nm light, Φ_{366} is 0.00024 ($\pm 1 \times 10^{-5}$). This value was entered into equation 5.8 to solve for Φ_{334}. The quantum yield for decomposition at 334 nm is 0.008 ($\pm$0.004). The quantum yields for each compound at 334 nm and 366 nm are reported in Table 5.4.

In order to compare the effect of substrate on quantum yield, reflectivity of the surface was also a factor. In the experiments that CaF_2 were used as substrates, the light intensity was divided by two.

5.5.6 Lithography

A film of *trans*-$(Et_3P)_2Ni(NO_2)_2$ was prepared on a silicon chip. A lithography mask was placed in contact with the sample. The sample was irradiated for 24 hr from the bottom through the lithography mask.

After photolysis, the film was developed by rinsing the film with acetone, thus removing unexposed starting material. The remaining pattern was clearly visible by both optical and electron microscopy. The image obtained with a scanning electron microscope is shown in Figure 5.9.

Chapter 6

Precursor Molecules for the Deposition of Thin Ferroelectric and Various Other Mixed Metal Oxide Films

6.1 Introduction

Metals and metal oxides are important for the fabrication of integrated circuits. This chapter will describe the deposition of metal oxide films of lead, zirconium, titanium, manganese, tin, calcium, nickel, lithium and iron. The preparation of mixed metal oxides ($M_wM'_xM''_yO_z$) will also be presented. Many mixed metal oxides are ferroelectric materials, which have a wide range of uses in the electronics industry [26, 32, 33, 34, 35]. The examples of ferroelectrics studied in this chapter include $Pb(Zr_xTi_{1-x})O_3$ (PZT), $BaTiO_3$, $BaBiO_3$, $BiMnO_3$.

It was found in our laboratory that copper carboxylate [50] and uranyl acetylacetonate (acac) [51] compounds can readily be cast into amorphous films. Photolysis of thin films of these precursors led to the loss of the carboxylate and acac ligands. If the photolysis was conducted in an air atmosphere, impurity-free metal oxide films were obtained. From these results, it was postulated that a variety of metal compounds containing these ligands would be useful precursors for the deposition of pure metal oxide films. This is the premise for the study described here.

In this chapter, a series of metal compounds were studied in order to investigate the feasibility of room temperature photochemical deposition of amorphous metal oxide films. If pure metal oxide films can be made using this technique, it could also be applied

to making binary and tertiary metal oxides. This would immensely broaden the scope of potential materials that could be deposited by our technique. One important class of materials that falls into this category is ferroelectric materials. Ferroelectric materials have numerous microelectronics applications, including capacitors [32, 34], nonvolatile memory devices [34, 35, 119], electrooptic devices [32, 119] and many others [120]. One goal of this study is to investigate a series of potential precursors for the deposition of complex materials.

The following sections will describe the outcome of photolysis experiments on thin amorphous films of Pb, Zr, Ti, Mn, Sn, Ca, Ni, Li and Fe precursors. Auger analysis results will be reported for films resultant from photolysis. Lithography experiments, including photolithography and dose requirements will be described. X-ray powder diffraction results for PZT films will also be presented.

6.2 Results

6.2.1 Spectroscopic data for the complexes

6.2.1.1 Metal 2-ethylhexanoate complexes

FTIR spectroscopic data for amorphous films of $M(O_2CCH(C_2H_5)C_4H_9)_x$ (M= Ni(II), Zr(IV), Pb(II), Mn(II), Fe(III), Ca(II), Li(I) and Sn(II)) are reported in Table 6.1. The frequency difference between the asymmetric and the symmetric CO_2 stretches, ($\Delta\nu = \nu_a(CO_2) - \nu_s(CO_2)$) is used to distinguish the types of bonding of the carboxylate with the metal. Several types of bonding types are available for this type of complex, shown in Figure 6.1. In general the $\Delta\nu$ values decrease in the order unidentate > ionic > bridging > bidentate bonding of the carboxylate ligand with metals [64]. For metal acetate

complexes, $\Delta\nu$ for ionic acetates is 164 cm^{-1}. Unidentate acetates have $\Delta\nu$ values in the range 200-300 cm^{-1}. Bidentate acetates have $\Delta\nu$ values between 40 and 80 cm^{-1}, and bridging acetates have $\Delta\nu$ values of approximately 140-170 cm^{-1}.

Table 6.1 FTIR spectroscopic data for complexes of the formula $M(O_2CCH(C_2H_5)C_4H_9)_x$

free acid	Ni(II)*	Zr(IV)	Pb(II)	Mn(II)	Fe(III)	Ca(II)*	Li(I)*	Sn(II)	Assignment
1744	1714	1701		1694	1690	1684	1707	1709	$\nu_a(CO_2)$ -unidentate
1709									$\nu_a(CO_2)$ -ionic
	1597	1578		1589	1589	1561	1584	1613	$\nu_a(CO_2)$ -bridging
	1578	1551	1518	1537sh	1551	1541	1545	1562	$\nu_a(CO_2)$ -bidentate
	1417	1462	1458	1462	1458	1458	1458	1460	$\nu_s(CO_2)$ -bidentate
1462		1425	1414	1412	1424	1420	1420	1410	$\nu_s(CO_2)$ -bridging
1418									$\nu_s(CO_2)$ -ionic
1383		1321	1379sh	1316	1381		1381	1314	$\nu_s(CO_2)$ -unidentate
			1319		1323				
1289				1296					
1271	1267			1273			1271	1273	
1229	1231			1235	1235		1231	1236	
1206				1208	1207			1208	
950					957				ν(CC)
	841		900		883				CO_2 def.[a]
			814	804	802		818	804	CO_2 def.[a]
781		733		732	758	783	783	760	CO_2 def.[a]
731		679		683	735				δ(OCO)
	687	636						679	
654	654	608						654	
				553					$\pi(CO_2)$[a]

[a]unidentate acetate has 3 bands (COO deformation) at 920-720 cm^{-1} and one band ($\pi(CO_2)$) at 540 cm^{-1}. These are absent in bridging complexes and reduced in number in bidentate [64]

Figure 6.1 Bonding modes for the 2-ethylhexanoate ligand

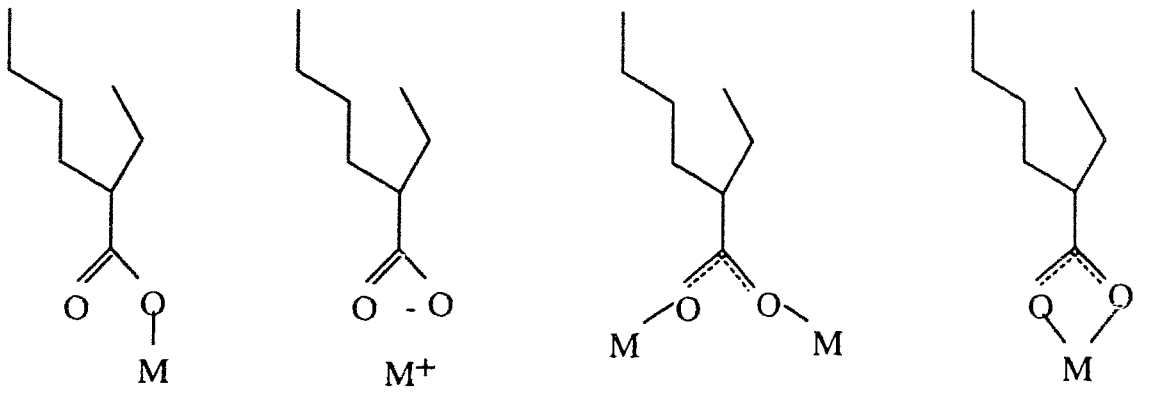

i) unidentate *ii)* ionic *iii)* bridging bidentate *iv)* bidentate

Bonding Type:	*i)* M= Ni(II), Zr(IV), Mn(II), Fe(III), Sn(II); 2-ethylhexanoic acid
	ii) 2-ethylhexanoic acid
	iii) M= Zr(IV), Mn(II), Fe(III), Ca(II), Li(I), Sn(II)
	iv) M= Zr(IV), Pb(II), Mn(II), Fe(III), Ca(II), Li(I), Sn(II)

The $\nu_a(CO_2)$ and $\nu_s(CO_2)$ values used to calculate $\Delta\nu$ for the complexes in this chapter were obtained from the data in Table 6.1 and the $\Delta\nu$ values are shown in Table 6.2. From this table it is evident that there are a number of different types of bonding of the carboxylate to each of the metals (refer to Figure 6.1). All complexes exhibit covalent bonding, with one or more of the three following types: unidentate, bridging bidentate, and bidentate. No evidence was observed for ionic bonding, where we would expect a $\Delta\nu$ value in the range between the $\Delta\nu$ values for unidentate and bridging types of approximately 247 cm^{-1}, as observed for the acid (see Table 6.2).

Table 6.2 Bonding type and characteristic frequency difference values, $\Delta\nu = \nu_a(CO_2)-\nu_s(CO_2)$ from the FTIR spectra of metal hexanoates. The data is reported in Table 6.1.

	Ni(II)	Zr(IV)	Pb(II)	Mn(II)	Fe(III)	Ca(II)	Li(I)	Sn(II)	free acid
$\nu_a-\nu_s$ (cm^{-1}) -unidentate	297	380		378	309			395	326
$\nu_a-\nu_s$ (cm^{-1}) -ionic									247
$\nu_a-\nu_s$ (cm^{-1}) -bridging		153		177	165	141	164	203	
$\nu_a-\nu_s$ (cm^{-1}) -bidentate		89	60	75	93	83	87	102	

[a] $\Delta\nu = \nu_a(CO)- \nu_s(CO)$; from Table 6.1.

Nickel (II) 2-ethylhexanoate has a $\nu_a(CO_2)$-$\nu_s(CO_2)$ of 297 cm^{-1} indicating only unidentate carboxylate bonds with the metal. It should be noted that weak interactions between molecules in the film are likely to be present. This indicates that it is a monomeric species, which is similar to the bonding found for Ni(II) acetate [121]. The lead (II) 2-ethylhexanoate also showed only one type of bonding with a ν_a- ν_s of 60 cm^{-1}. In this case the lead is coordinated to the 2-ethylhexanoate ligands in a bidentate fashion, hence it is also monomeric. Based on the frequency difference values in Table 6.2, all of the metal 2-ethylhexanoate complexes (except for Ni(II) and Pb(II)) have both bidentate and bridging bidentate metal-carboxylate bonds. This indicates that most of the complexes exist in dimeric or polymeric form in amorphous films. The 2-ethylhexanoate complexes of Zr(IV), Mn(II), Fe(III) and Sn(II) exhibit a mixture of unidentate, bidentate and bridging metal-carboxylate bonds. The Ca(II) and Li(I) 2-ethylhexanoates have bidentate and bridging metal-carboxylate bonds. The $\Delta\nu$ values for Ca(II) 2-ethylhexanoate are 141 cm^{-1} and 83 cm^{-1}, corresponding to bridging and bidentate carboxylate coordination respectively. This result is similar to the FTIR results found for Ca(II) acetate, which has frequency difference values of 148 cm^{-1} for bridging and 86 cm^{-1} for bidentate acetate [121].

6.2.1.2 Titanium bis-acetylacetonate di-isopropoxide

The FTIR spectroscopic data for the complex $Ti(CH_3COCHCOCH_3)_2(OCH(CH_3)_2)_2$ is reported in Table 6.3. The FTIR spectrum of the

$Ti(acac)_2(i\text{-}prop)_2$ was assigned by analogy with the assignments of various metal acetylacetonate and metal alkoxide complexes [64]. The absorptions at 1013 and 993 cm^{-1} are assigned to the ν(CO) bands of the isopropoxide ligands. The absorption band at 930 cm^{-1} is assigned to ν(CC) + ν(CO) of the isopropoxide. The remaining absorptions are assigned to the acac ligand. The band at 1589 cm^{-1} is assigned to ν(CC) coupled with ν(CO) and the band at 1524 cm^{-1} is assigned to ν(CO) coupled with ν(CC). The acac ligand is bidentate, and the isopropoxide ligands are *cis* oriented [122].

Table 6.3 FTIR spectroscopic data for $Ti(CH_3COCHCOCH_3)_2(OCH(CH_3)_2)_2$

frequency (cm^{-1})	Assignment[a]	ligand
1605		
1589	ν(CC) + ν(CO)	acac
1524	ν(CO) + ν(CC)	acac
1435	δ(CH) + ν(CC)	acac
1383	$\delta_S(CH_3)$	acac
1360 sh		
1327		
1277	ν(C-CH_3) + ν(CC)	acac
1013	ν(CO)	i-prop
993	ν(CO)	i-prop
930	ν(CC) + ν(CO)	i-prop
851	π(CH)	acac
770		
665	π(CH_3CCO)	acac
624	ring deformation + ν(TiO)	acac

[a]assignments based on $M(acac)_x$ and $M(OR)_x$ complexes [64]

6.2.2 Preparation of metal oxide films

6.2.2.1 Photochemistry of manganese (II) 2-ethylhexanoate films

An amorphous film of manganese (II) 2-ethylhexanoate was prepared by spin coating a solution of the complex in CH_2Cl_2 onto a silicon substrate. The photolysis of the complex was monitored by FTIR spectroscopy. Figure 6.2 shows the photoinduced decay of the FTIR bands at 1684, 1589 and 1537 cm^{-1} associated with the $\nu_a(CO_2)$ and 1462, 1412 and 1316 cm^{-1} associated with the $\nu_s(CO_2)$ stretches. Concurrently, a broad band centered at 1550 cm^{-1} is observed to grow in intensity and then decay following further photolysis. This indicates that irradiation of manganese (II) 2-ethylhexanoate yields a thermally stable, photosensitive product, which loses all ligands upon prolonged photolysis. The photoreaction observed is consistent with equation 6.1. In the presence of air, reaction with oxygen is expected to yield manganese oxide. The film was analysed by Auger spectroscopy to determine the product of photolysis.

Figure 6.2 Spectroscopic changes associated with photolysis of Manganese (II) 2-ethylhexanoate for 0, 15, 30, 60 and 1440 min.

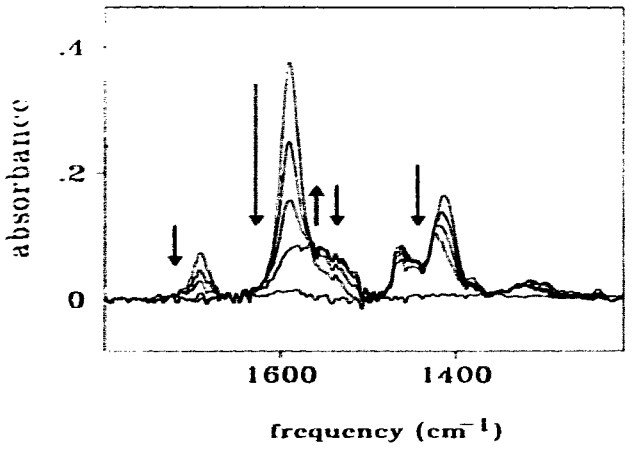

$$Mn(O_2CCH(C_2H_5)C_4H_9)_2 \xrightarrow{h\nu} Mn(O_2CCH(C_2H_5)C_4H_9) + CO_2$$
$$+ \bullet CH(C_2H_5)C_4H_9 \xrightarrow{h\nu} Mn + 2CO_2 + 2\bullet CH(C_2H_5)C_4H_9 \qquad (6.1)$$

Following the photolysis of a Mn(II) 2-ethylhexanoate film, the resultant film was analysed by Auger electron spectroscopy. The surface of the film, cleaned by sputtering the surface with Ar^+ ions for 5 seconds, contained 45.5 (±9)% manganese and 54.5 (±11)% oxygen. No signal due to carbon was observed. This confirms that the ligands are lost upon photolysis. The composition of the film is within error of MnO or Mn_2O_3, stable oxides of manganese [123]. The results of Auger analysis are summarized in Table 6.4.

Table 6.4 Auger analysis of films resultant from photolysis of metal 2-ethylhexanoates (M= Ni, Zr, Pb, Mn, Fe, Ca, Li, Sn) and $Ti(acac)_2(i\text{-prop})_2$ with 254 nm light.

Precursor	sputter time (sec)	% M[a]	% O[a]	% C[a]	composition (calcd)
$Mn(O_2CCH(C_2H_5)C_4H_9)_2$	0	35.8 (±7)	47.7 (±10)	16.5 (±3)	Mn_3O_4
	5	45.5 (±9)	54.5 (±11)	--	Mn_5O_6
	10	45.5 (±9)	54.5 (±11)	--	Mn_5O_6
$Zr(O_2CCH(C_2H_5)C_4H_9)_4$	0	21.2 (±4)	67.8 (±14)	11.0 (±2)	Zr_5O_{16}
	5	27.4 (±5)	72.6 (±15)	--	Zr_3O_8
	10	26.5 (±5)	73.5 (±15)	--	Zr_4O_{11}
	20	28.5 (±6)	71.5 (±14)	--	Zr_2O_5
$Sn(O_2CCH(C_2H_5)C_4H_9)_2$	0	40.8 (±8)	58.6 (±12)	--	Sn_2O_3
	10	46.2 (±9)	53.8 (±11)	--	Sn_6O_7
$Fe(O_2CCH(C_2H_5)C_4H_9)_3$	0	29.9 (±6)	41.7 (±8)	28.5 (±6)	Fe_3O_4
	20	45.8 (±9)	54.2 (±11)	--	Fe_5O_6
$Ca(O_2CCH(C_2H_5)C_4H_9)_2$	0	38.5 (±8)	31.9 (±6)	29.6 (±8)	Ca_6O_5
	10	55.6 (±11)	34.7 (±7)	9.7 (±2)	Ca_8O_5
	25	62.5 (±12)	37.5 (±7)	--	Ca_5O_3
$Li(O_2CCH(C_2H_5)C_4H_9)$	5	41.2 (±8)	39.2 (±8)	19.6 (±4)	LiO
$Pb(O_2CCH(C_2H_5)C_4H_9)_2$	10	55.4 (±11)	44.6 (±9)	--	Pb_5O_4
	20	52.5 (±10)	47.5 (±10)	--	$Pb_{11}O_{10}$
	30	49.1 (±10)	50.9 (±10)	--	PbO
$Ni(O_2CCH(C_2H_5)C_4H_9)_2$	10	60.6 (±12)	27.6 (±6)	11.8 (±2)	$Ni_{11}O_5$
	35	75.0 (±15)	14.5 (±3)	10.5 (±2)	$Ni_{31}O_6$
$Ti(CH_3COCHCOCH_3)_2$ $(OCH(CH_3)_2)_2$	0	23.7 (±5)	76.3 (±15)	--	Ti_5O_{16}
	10	28.8 (±6)	71.2 (±14)	--	Ti_2O_3
	15	29.9 (±6)	70.1 (±14)	--	Ti_3O_7

[a] error approximately 20 atom% [85]

6.2.2.2 Photochemistryof zirconium (IV) 2-ethylhexanoate films

Photolysis of a film of Zr(IV) 2-ethylhexanoate resulted in the loss of all FTIR absorptions associated with the complex. No new absorptions were observed throughout the experiment, however, the rate of decay of the absorption bands at 1578 and 1551 cm^{-1} decayed at a slower rate than the bands at 1462 and 1425 cm^{-1}. This indicates that a thermally stable primary photoproduct has absorptions coincident with the starting material. Loss of all IR absorptions was observed on prolonged photolysis. These results are consistent with equation 6.2.

$$Zr(O_2CCH(C_2H_5)C_4H_9)_4 \xrightarrow{h\nu} Zr(O_2CCH(C_2H_5)C_4H_9)_3 + CO_2$$
$$+ \bullet CH(C_2H_5)C_4H_9 \xrightarrow{h\nu} Zr + 4CO_2 + 4 \bullet CH(C_2H_5)C_4H_9 \qquad (6.2)$$

The results of Auger analysis of a film produced from photolysis of zirconium (IV) 2-ethylhexanoate in air are summarized in Table 6.4. The surface of the film contained 11(±2) % carbon, originating presumably from the atmosphere. After a 20 sec sputter the film contained 28.5(±6) % Zr and 71.5(±14) % O. The composition of the film was within error of ZrO_2, the only known stable form of zirconium oxide [123].

6.2.2.3 Photochemistry of tin (II) 2-ethylhexanoate films

The photolysis of an amorphous film of tin (II) 2-ethylhexanoate was monitored by FTIR spectroscopy. All FTIR absorption bands corresponding to the ligands decayed completely and no evidence was found for the formation of an intermediate. This indicates that all ligands were lost on photolysis consistent with equation 6.3.

$$Sn(O_2CCH(C_2H_5)C_4H_9)_2 \xrightarrow{h\nu} Sn + 2CO_2 + 2 \bullet CH(C_2H_5)C_4H_9 \qquad (6.3)$$

Auger analysis of a film resultant from photolysis of $Sn(O_2CCH(C_2H_5)C_4H_9)_2$ in air indicated that the film contained 40.8(±8) % Sn and 58.6(±12) % O. No signal due to carbon was observed. This indicates that all ligands are lost upon photolysis. The composition of the resultant film was within error of SnO.

6.2.2.4 Photochemistry of iron (III) 2-ethylhexanoate films

The photolysis of an amorphous film of iron (III) 2-ethylhexanoate was monitored by FTIR spectroscopy. All FTIR absorptions corresponding to the ligands decreased to zero intensity. No evidence was found for the formation of an intermediate. The reaction is shown in equation 6.4.

$$Fe(O_2CCH(C_2H_5)C_4H_9)_3 \xrightarrow{h\nu} Fe + 3CO_2 + 3 \cdot CH(C_2H_5)C_4H_9 \qquad (6.4)$$

Auger analysis of a film resultant from photolysis of $Fe(O_2CCH(C_2H_5)C_4H_9)_3$ in air indicated that the surface contained 28.5(±6) % carbon (see Table 6.4). Following a 20 sec sputter, no signal due to carbon was observed. The film contained 45.8(±9) %Fe and 54.2(±11) %O. The composition of the film was within error of Fe_3O_4, however, iron oxide is often found to be nonstoichiometric [123].

6.2.2.5 Photochemistry of calcium (II) 2-ethylhexanoate films

Tne photolysis of an amorphous film of calcium (II) 2-ethylhexanoate was monitored by FTIR spectroscopy. All absorptions due to the ligand vibrations decreased

to zero intensity. No evidence was observed for the formation of a thermally stable primary photoproduct. The photoreaction is summarized in equation 6.5.

$$Ca(O_2CCH(C_2H_5)C_4H_9)_2 \xrightarrow{h\nu} Ca + 2CO_2 + 2 \bullet CH(C_2H_5)C_4H_9 \qquad (6.5)$$

The film resultant from photolysis was analysed by Auger electron spectroscopy. The surface of the film contained 38.5(±8)% Ca, 31.9(±6)% O and 29.6(±6)% C. Following a 25 sec sputter, the film contained 62.5(±12)% Ca and 37.5(±7)% O. The composition of the surface of the film was CaO (within error), the only known, stable form of calcium oxide. The inner portion of the film has a higher Ca:O ratio which may be due to preferential sputtering of the oxygen [19]. The results of Auger analysis are summarized in Table 6.4.

6.2.2.6 Photochemistry of lithium (I) 2-ethylhexanoate films

The photolysis of lithium (I) 2-ethylhexanoate was followed by FTIR spectroscopy. The loss of all FTIR absorptions corresponding to the ligands was observed on photolysis. No evidence for the formation of an intermediate was observed. The photoreaction is shown in equation 6.6.

$$Li(O_2CCH(C_2H_5)C_4H_9) \xrightarrow{h\nu} Li + CO_2 + \bullet CH(C_2H_5)C_4H_9 \qquad (6.6)$$

The film resultant from photolysis was analysed by Auger spectroscopy. Following a 5 sec sputter the film contained 41.2(±8)% Li, 39.2(±8)% O and 19.6(±4)% C. The film was contaminated with carbon, presumably from the atmosphere. The composition of the metal oxide in this film according to Auger analysis was LiO. The

only known oxide of lithium is Li_2O [123]. Presumably, this is due to the noise in the lithium signal at low energy (43 eV) [124].

6.2.2.7 Photochemistry of lead (II) 2-ethylhexanoate films

The photolysis of lead (II) 2-ethylhexanoate was monitored by FTIR spectroscopy. All FTIR absorption bands due to the 2-ethylhexanoate ligand decreased to zero intensity on photolysis. A broad band centered around 1400 cm^{-1} appeared during photolysis and increased in intensity. This absorption remained after prolonged photolysis. This sample was then analysed by Auger spectroscopy to determine if all the ligands were removed from the film.

The results of Auger analysis are summarized in Table 6.4. The film, following a 30 sec sputter, contained 49.1(±10)% Pb and 50.9(±10)% O. No signal due to carbon was observed. The composition was approximately PbO. It should be noted that the sensitivity factor for lead was approximated by extrapolation of the sensitivity factors for the elements found in the *Handbook of Auger Electron Spectroscopy* [124]. Therefore, the relative amounts of Pb:O are approximate. However, of most importance is the observation that there is no carbon within the film. This indicates that the broad FTIR absorption at approximately 1400 cm^{-1} contains no carbon. This band is presumably due to lead hydroxide. The photoreaction of the lead (II) 2-ethylhexanoate film is shown in equation 6.7.

$$Pb(O_2CCH(C_2H_5)C_4H_9)_2 \xrightarrow{h\nu} Pb + 2CO_2 + 2 \cdot CH(C_2H_5)C_4H_9 \qquad (6.7)$$

6.2.2.8 Photochemistry of nickel (II) 2-ethylhexanoate films

The photolysis of an amorphous film of nickel (II) 2-ethylhexanoate was monitored by FTIR spectroscopy. The film contained a mixture of the nickel complex and free 2-ethylhexanoic acid. The loss of all IR absorptions corresponding to the 2-ethylhexanoate was observed on photolysis. No evidence consistent with the formation of an intermediate was observed. The photoreaction observed is consistent with equation 6.8.

$$Ni(O_2CCH(C_2H_5)C_4H_9)_2 \xrightarrow{h\nu} Ni + 2CO_2 + 2 \bullet CH(C_2H_5)C_4H_9 \qquad (6.8)$$

The film resultant from photolysis of $Ni(O_2CCH(C_2H_5)C_4H_9)_2$ was analysed by Auger spectroscopy. Following a 10 sec sputter the film contained 60.6(±12)% Ni, 27.6(±6)% O and 11.8(±2)% C. The composition of the film was Ni_2O, within error. There is no known nickel oxide with this stoichiometry [123]. Preferential sputtering of oxygen may have occurred, or, alternatively, the film may be composed of Ni and NiO. Carbon contamination was evident throughout the film (Table 6.4). Films of nickel (II) 2-ethylhexanoate had a tendency to crystallize. Recombination of the photoejected ligands with the metal fragments may have prevented complete ejection of the ligands from the film.

6.2.2.9 Photochemistry of titanium bis-acetylacetonate di-isopropoxide films

The photolysis of an amorphous film of $Ti(acac)_2(i\text{-}prop)_2$ was monitored by FTIR spectroscopy. Loss of all IR absorptions was observed on photolysis. No evidence

consistent with the formation of an intermediate was observed throughout the reaction. The photoreaction is shown in equation 6.9.

$$Ti(CH_3COCHCOCH_3)_2(OCH(CH_3)_2)_2 \xrightarrow{h\nu} Ti + 2 \cdot CH_3COCHCOCH_3 + 2 \cdot OCH(CH_3)_2 \qquad (6.9)$$

The film resultant from photolysis was analysed by Auger spectroscopy. Following a 10 sec sputter, the film contained 28.8(±6)% Ti and 71.2(±14)% O. No signal due to carbon was observed throughout the film. The composition of this film was TiO_2, within error. The results of Auger analysis are summarized in Table 6.4.

6.2.3 Preparation *of various mixed metal oxides*

6.2.3.1 Preparation of lithium manganese oxide ($LiMnO_2$) films

A 1:1 stoichiometric mixture of $Li(O_2CCH(C_2H_4)C_4H_9)$ and $Mn(O_2CCH(C_2H_4)C_4H_9)_2$ was prepared. An FTIR spectrum was obtained. This film was photolysed for 14 hours. Another FTIR spectrum was obtained to ensure that all absorptions had decreased to zero intensity. Auger analysis of this film indicated that the composition was approximately LiMnO. The surface of the Li:Mn sample contained 16.7 % carbon; but no signal due to carbon was observed in the inner portion of the film. The stoichiometry LiMnO is not known. Presumably, the true composition is $LiMnO_2$, and the low percentage of oxygen observed is due to preferential sputtering.

Table 6.5 Auger analysis using a 3 keV beam of various mixed metal oxide, $M_xM'_yO_z$ films.

Precursor ratio	sputter (sec)	%Ba[a,b]	%Ti[b]	%Li[b]	%Mn[b]	%Bi[b,c]	%O[b]	%C[b]	composition (calcd)
Li:Mn	0			40.0	21.8		26.5	16.7	Li_2MnO
1:1	10			32.7	33.6		33.7	--	LiMnO
	20			33.5	32.9		33.6	--	LiMnO
Ba:Ti	0	24.1	14.0				52.4	9.5	$Ba_5Ti_3O_{11}$
1:1	10	22.9	18.2				58.9	--	$BaTiO_3$
	20	21.2	19.0				59.8	--	$BaTiO_3$
Bi:Mn	0				24.7	24.7[c]	45.6	5.0	$Bi_5Mn_5O_9$
1:1	10				23.1	23.1[c]	46.3	7.5	$BiMnO_2$
	15				23.3	23.3[c]	46.7	6.7	$BiMnO_2$
Ba:Bi	0	19.2				19.2[c]	37.8	23.8	$BaBiO_2$
1:1	10	26.7				26.7[c]	46.6	--	$Ba_4Bi_4O_7$
	20	27.6				27.6[c]	44.8	--	$Ba_5Bi_5O_8$

[a] sensitivity factor=0.32, obtained from a standard BaO film [125]
[b] error estimated at approximately 20 atom% [85]
[c] estimated as 1:1 ratio Bi:M (no sensitivity factor available for Bi)

6.2.3.2 Preparation of barium titanate ($BaTiO_3$) films

The photochemistry of $Ba(O_2CCH(C_2H_4)C_4H_9)_2$ was studied previously in our laboratory. This complex loses all ligands upon photolysis [125]. A 1:1 stoichiometric mixture of $Ba(O_2CCH(C_2H_4)C_4H_9)_2$ and $Ti(acac)_2(i\text{-}prop)_2$ was spin coated on silicon and an FTIR spectrum of the film was obtained. This film was irradiated with 254 nm light for 1 week, and another FTIR spectrum was obtained to ensure that the FTIR absorptions decreased to zero intensity. This sample was analysed by Auger spectroscopy and the results are summarized in Table 6.5. The surface was contaminated with carbon. Following a 10 sec sputter cleaning, no signal due to carbon was observed. The

composition of the film was $BaTiO_3$. The sensitivity factor used for Ba in the calculations was 0.32, which was determined using a standard sample of BaO [125].

6.2.3.3 Preparation of bismuth manganate ($BiMnO_3$) films

A film of 1:1 bismuth (III) 2-ethylhexanoate and manganese (II) 2-ethylhexanoate was irradiated. No sensitivity factor was published for bismuth using 3 keV excitation [124]. Therefore, the ratio of bismuth to manganese was estimated as 1:1 in the calculation. A small amount of carbon was found throughout the film (<10 %). The composition of this film was calculated as $BiMnO_2$, but is more likely $BiMnO_3$.

6.2.3.4 Preparation of barium bismuthate ($BaBiO_3$) films

A film of Ba:Bi (1:1) was prepared. Auger analysis indicated that the composition of the film resultant from photolysis was calculated as $BaBiO_2$, but is more likely $BaBiO_3$. This sample contained 24% carbon on the surface and no signal due to carbon was observed in the inner portions of the film.

6.2.4 Preparation of $PbTiO_3$, $PbZrO_3$ and $Pb(Zr_{0.5}Ti_{0.5})O_3$ films

6.2.4.1 Preparation of $PbTiO_3$ and $PbZrO_3$ films

The stoichiometric solutions used for the preparation of $PbTiO_3$ and $PbZrO_3$ were made with 1:1 mole ratios of Pb:Ti and Pb:Zr respectively. The photolysis of these mixtures was monitored by FTIR spectroscopy. All FTIR bands associated with the ligands decreased to zero intensity, indicating the loss of all ligands. The films resultant from photolysis were analysed by Auger spectroscopy.

The results of Auger analysis of $PbTiO_x$ and $PbZrO_x$ films resultant from photolysis are summarized in Table 6.6. The sensitivity factor for Pb relative to Ti (0.696 Pb/Ti sensitivity) was calibrated by Yoon et. al. [126] and used in these calculations. The surfaces of both films were contaminated with carbon from the atmosphere. After sputter cleaning with 3 kV Ar^+ ions for 10 sec no carbon contamination was observed. This indicates that photolysis of these mixtures ejects all ligands from the film resulting in the mixed metal oxides when the films are exposed to air. The composition of the film resultant from photolysis of a 1:1 Pb:Ti precursor was $PbTiO_3$, within error. The composition of the 1:1 Pb:Zr film was $PbZrO_3$, within error.

Table 6.6 Auger analysis of films resultant from photolysis of 1:1 Pb:Zr, 1:1 Pb:Ti and 2:1:1 Pb:Zr:Ti precursors with 254 nm light.

precursor/ conditions	sputter (sec)	% Pb[a]	% Zr[a]	% Ti[a]	% O[a]	% C[a]	composition (calcd)
Pb, Zr	0	18.1	14.3		34.8	32.9	
(1:1)	10	24.1	20.8		55.1	--	$Pb_{1.2}ZrO_{2.6}$
	20	22.9	19.8		57.3	--	$Pb_{1.2}ZrO_{2.9}$
Pb, Ti	0	17.1		10.1	55.8	17.0	
(1:1)	10	15.6		18.4	65.9	--	$Pb_{0.8}TiO_{3.6}$
	20	14.1		19.6	66.3	--	$Pb_{0.7}TiO_{3.4}$
Pb, Zr, Ti (2:1:1) no anneal	20	22.6	10.0	10.0	57.5	--	$Pb_{1.1}(Zr_{0.5}Ti_{0.5})O_{2.9}$
Pb, Zr, Ti	0	25.9	6.3	6.7	55.4	5.6	$Pb_{2.0}(Zr_{.48}Ti_{.52})O_2$
(2:1:1)	20	13.1	6.1	6.7	74.0	--	$Pb_{1.0}(Zr_{.48}Ti_{.52})O_{5.8}$
anneal[b]							

[a]error approximately 20 atom% [85], [b]30 min at 650°C, air atmosphere

6.2.4.2 Lead zirconate titanate ($Pb(Zr_{0.5}Ti_{0.5})O_3$) (PZT) films

A 2:1:1 stoichiometric solution of the lead, zirconium and titanium precursors was prepared. An amorphous film of these precursors in the 2:1:1 Pb:Zr:Ti ratio was prepared by spin coating on silicon. This was the precursor used for the desired product, $Pb(Zr_{0.5}Ti_{0.5})O_3$. An FTIR spectrum of the precursor film was obtained, and exhibited an overlap of the FTIR absorptions of each complex (see Tables 6.1 and 6.3 for absorption band positions). The film was then irradiated for 1 hour and another FTIR spectrum was obtained. This irradiation procedure was repeated for cumulative photolysis times of 20 and 52 hours. Loss of all infrared absorptions was observed.

Figure 6.3 illustrates the loss of intensity of all absorptions due to the ligands in the FTIR spectra of a) $Pb(O_2CCH(C_2H_5)C_4H_9)_2$, b) $Zr(O_2CCH(C_2H_5)C_4H_9)_4$, c) $Ti(CH_3COCHCOCH_3)_2(OCH(CH_3)_2)_2$ and d) 2: 1: 1 Pb: Zr: Ti precursor mixture films following photolysis. It is apparent that when the precursors are mixed, the same spectral changes occur on photolysis as that of the separate precursors (Fig. 6.3 a), b), c)). This is based on the observation that all bands due to the starting material decrease to zero intensity, with subsequent production of a broad band around 1400 cm^{-1} coincident with the product of the lead precursor. No evidence for a unique intermediate is observed for the process.

Figure 6.3 Spectroscopic changes associated with photolysis with 254 nm light of films of the a) Pb precursor for 0, 1 and 20 hr; b) Zr precursor for 0 min, 10 min, 190 min, 1 day, 1 week; c) Ti precursor for 0, 1, 20 hr d) 2:1:1 Pb:Zr:Ti precursors for 0 min, 20 min, 20 hr.

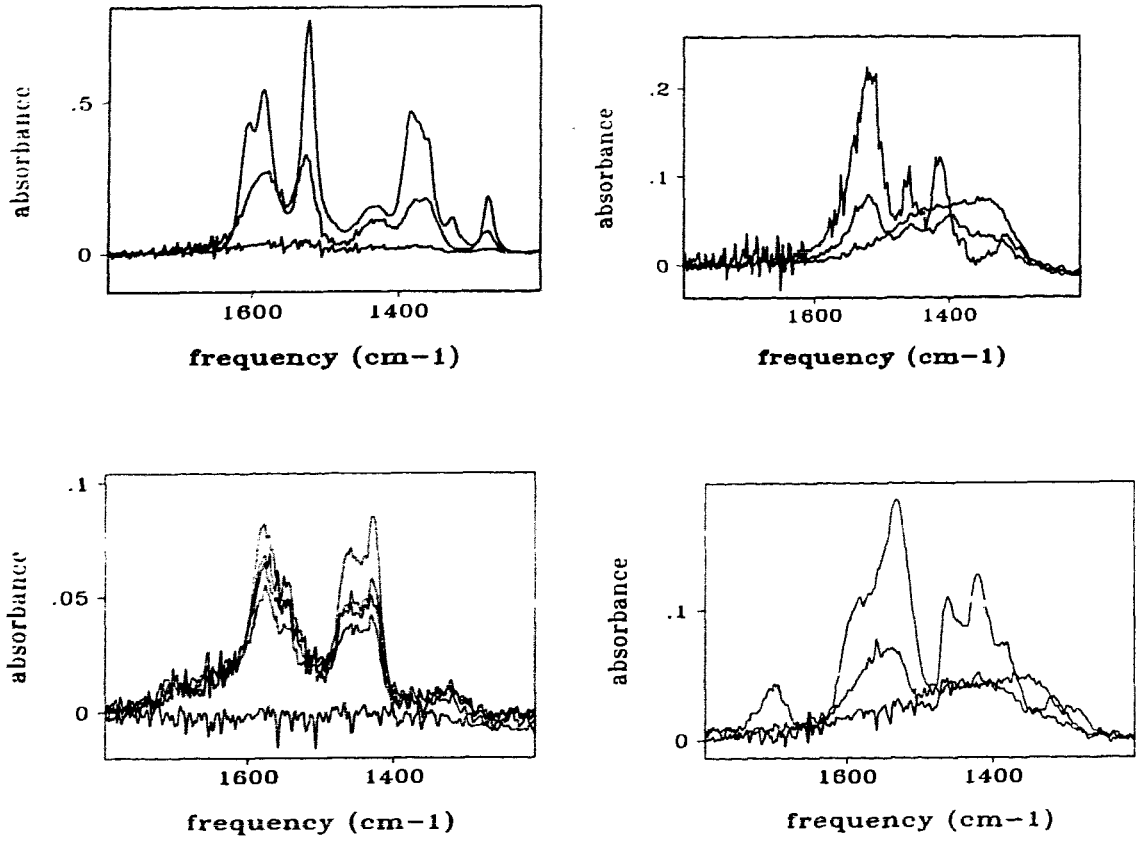

It should be noted that the efficiency of decomposition of the multicomponent precursor solutions appears to be different from that of single component systems. In particular, the efficiency of decomposition of the precursor mixtures used to prepare $PbZrO_3$ and $Pb(Zr_{0.5}Ti_{0.5})O_3$, is greater than the efficiency of decomposition of the Zr precursor alone. For example, the half-life for photolysis of the lead, zirconium and titanium precursors was 38.5, 73.3 and 47.5 min, respectively. The half-life for the combined precursors, for the deposition of $Pb(Zr_{0.5}Ti_{0.5})O_3$, was 44.3 min under the same conditions.

The difference in efficiency of decomposition may indicate the following. The Zr precursor is polymeric, and when photolysed alone, it may recombine with nearest neighbours, retaining its polymeric structure, thus slowing the process of decomposition. When the Zr complex is present in a multicomponent system, the polymeric structure may break down more readily as a result of having no "like" neighbours.

Photolysis of $Pb(O_2CCH(C_2H_4)C_4H_9)_2$, $Zr(O_2CCH(C_2H_4)C_4H_9)_4$ and $Ti(CH_3COCHCOCH_3)_2(OCH(CH_3)_2)_2$ precursor films separately yielded pure metal oxide films (Table 6.4). After photolysis of a film containing a 2:1:1 Pb:Zr:Ti ratio of precursors, the film was placed in an Auger spectrometer for elemental analysis of the surface. No carbon was found in the film indicating that all ligands were ejected from the film during photolysis. The composition of the film calculated from the Auger spectrum [124, 126] was $Pb_{1.1}(Zr_{0.48}Ti_{0.52})O_{2.9}$. The results are reported in Table 6.6. This film was annealed in an air atmosphere at 650 °C for 30 min in a Lindberg furnace and allowed to return to room temperature slowly. This was done in attempt to form the

tetragonal phase. This phase is the ferroelectric phase of the material. The film was then analysed by Auger spectroscopy. On the surface of this film, some carbon contamination was observed. Sputter cleaning the surface with argon ions revealed a carbon-free surface with a composition of $Pb_{1.0}(Zr_{0.48}Ti_{0.52})O_{5.8}$. These results indicate that photolysis of a stoichiometric mixture of these precursors yields the same composition in the product film. The surface was lead rich, consistent with the diffusion of lead to the surface during the annealing process [37].

Crystalline forms of $PbTiO_3$, $PbZrO_3$, and $Pb(Zr_{0.5}Ti_{0.5})O_3$ have the perovskite ABO_3 structure (A= Pb^{2+}, B= Zr^{4+}, Ti^{4+}) in which TiO_6 (and ZrO_6) octahedra are linked at the faces and Pb^{2+} occupy the corners of the unit cell (Figure 6.4). In the cubic arrangement, the paraelectric phase, a = b = c in the unit cell (Fig. 6.4 a)). The tetragonal phase is the ferroelectric phase, in which the axial O-B-O (B= Zr, Ti) c-axis is elongated, therefore $a = b \neq c$ (Figure 6.4 b)).

Figure 6.4 Perovskite structure for $Pb(Zr_xTi_{1-x})O_3$ a) cubic and b) tetragonal phases

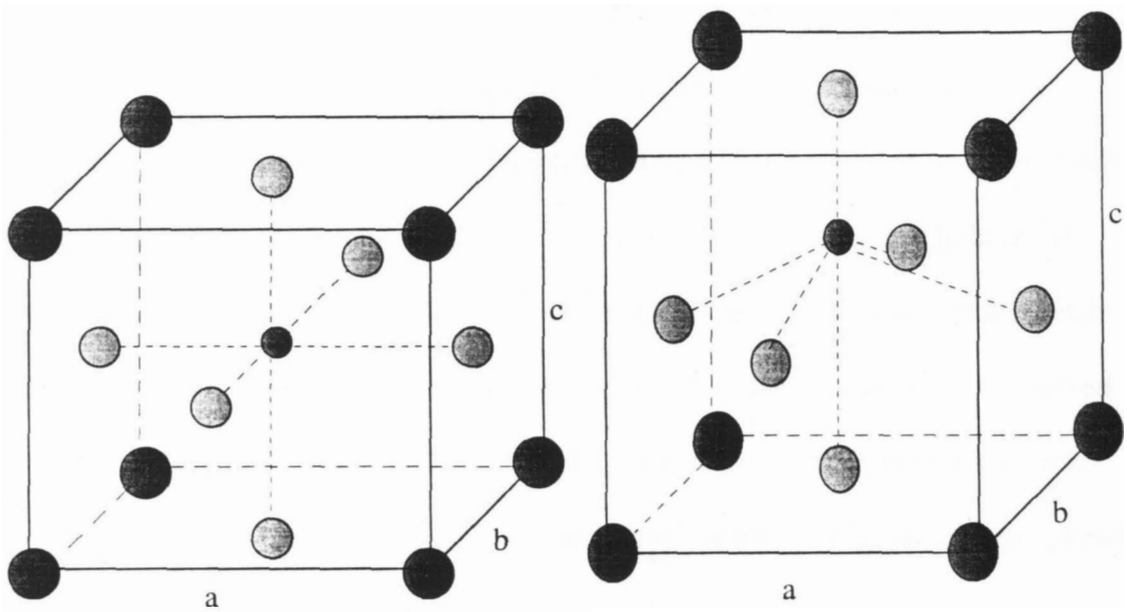

a) cubic phase (a=b=c)

b) tetragonal phase (a=b≠c)

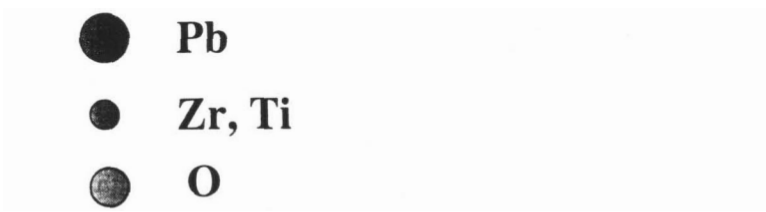

In order to determine if the tetragonal phase of $Pb(Zr_{0.5}Ti_{0.5})O_3$ was formed upon annealing, a film was analysed by XRD. The 2:1:1 stoichiometric mixture of Pb:Zr:Ti precursors was spin coated onto a Pt(111)/Ti/Si (2000 Å Pt, 500 Å Ti) surface [34] and the film was photolysed to remove all ligands. The Pt(111) substrate was used for this study since PZT is known to deposit preferentially in the (111) orientation on this surface under the appropriate conditions [34, 37]. This substrate does not transmit light in the infrared region therefore a control film was prepared and the photolysis was monitored by FTIR spectroscopy. When the loss of all FTIR bands due to the precursors was observed for the control film, the film on the Pt(111) surface was removed from the light source.

Thermal annealing experiments were performed on the photoproduced amorphous film. To determine whether the perovskite $Pb(Zr_{0.5}Ti_{0.5})O_3$ phase could be formed, a film on Pt(111) after photolysis was annealed according to literature procedures, at 650°C for 30 minutes [34]. This film was analysed by grazing incidence X-ray powder diffraction and the spectrum is shown in Figure 6.5.

Figure 6.5 X-ray powder diffraction pattern for $Pb(Zr_{0.5}Ti_{0.5})O_3$ on Pt(111)/Ti/Si.

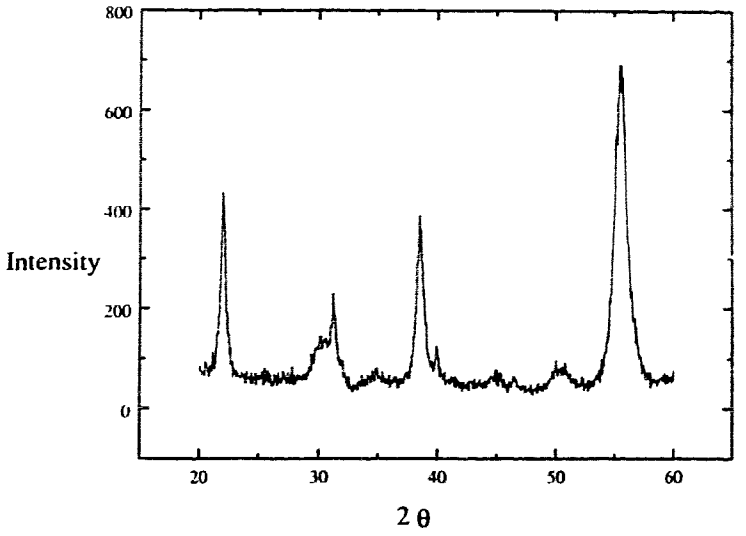

The polycrystalline film consists of the tetragonal phase of PZT with peaks arising at approximately $2\theta = 22°$, 31°, 39°, 45°, and 55°. These peaks correspond to the (100), (110), (111), (200), and (211) orientations, respectively. A broad peak centered around $2\theta = 30°$ was also evident. This may correspond to the metastable pyrochlore phase. The pyrochlore phase is lead deficient, which means the amount of Pb, labelled x, in $Pb_x(Zr_{0.48}Ti_{0.52})O_3$ is less than one, consistent with the loss of lead oxide during the anneal at 650 °C. Lead oxide is known to evaporate from films during the thermal annealing conditions described here [33, 37].

The tetragonal form has a unit cell that c >(a = b) (see Fig. 6.4 b)). These lattice parameters were calculated from the position of the 2θ values using the Bragg equation (eq. 6.1) and equation 6.2. The 2θ values at 43.55 and 44.9, corresponding to the (002)

and (200) (*hkl*) orientations respectively, were used in the calculation. The value for c was calculated as 4.152, and a= 4.033. The c/a ratio is 1.030, within error of the literature value for $Pb(Zr_{0.52}Ti_{0.48})O_3$ of 1.027 [127, 128].

$$n\lambda = 2d\sin\theta \tag{6.10}$$

$$\frac{1}{d^2} = \frac{h^2 + k^2}{a^2} + \frac{l^2}{c^2} \tag{6.11}$$

6.2.5 Lithography

Photolithography experiments were conducted with amorphous films of the compounds to determine minimum dose requirements to leave an insoluble pattern on the surface. An amorphous film of manganese (II) 2-ethylhexanoate on silicon was made by spin coating. The film was then partially covered and the sample was irradiated for 1 min with 254 nm light. The light intensity was 4.4 $mWcm^{-2}$. The light source was then removed and the film was dipped in ethanol. Both the exposed and the unexposed portions of the film dissolved. Another film of the complex was made and the same procedure was followed for an irradiation time of 5 minutes. Again, both exposed and unexposed areas dissolved in ethanol. A new film was prepared and irradiated for 10 min. When the resultant film was dipped in ethanol, the unexposed region dissolved and the exposed region remained on the surface. This indicates that films of this complex required 2.6 J/cm^2 dose of 254 nm light to leave a pattern on the surface (see Table 6.7). It should be noted that this dosage is an upper limit for the minimum dose required.

Table 6.7 Dose requirements for patterning with 4.4 mW/cm^2 output of a 254 nm mercury light source.

Precursor	Image formation (P= pattern,--= no pattern) with various dosages in J cm^{-2}						
	0.044	0.26	1.3	2.6	7.9	32	380
$Pb(O_2CCH(C_2H_5)C_4H_9)_2$	P	P	P	P	P	P	P
$Mn(O_2CCH(C_2H_5)C_4H_9)_2$	--	--	--	P	P	P	P
$Sn(O_2CCH(C_2H_5)C_4H_9)_2$	--	--	--	P	P	P	P
$Fe(O_2CCH(C_2H_5)C_4H_9)_3$	--	--	--	--	P	P	P
$Ti(CH_3COCHCOCH_3)_2(OCH(CH_3)_2)_2$	--	--	--	--	P	P	P
$Zr(O_2CCH(C_2H_5)C_4H_9)_4$	--	--	--	--	--	P	P
$Ni(O_2CCH(C_2H_5)C_4H_9)_2$	--	--	--	--	--	--	P
$Ca(O_2CCH(C_2H_5)C_4H_9)_2$	--	--	--	--	--	--	P
$Li(O_2CCH(C_2H_5)C_4H_9)$	--	--	--	--	--	--	P
Pb:Zr (1:1)	--	--	P	P	P	P	P
Pb:Ti (1:1)	--	--	--	P	P	P	P
Pb:Zr:Ti (2:1:1)	--	--	--	P	P	P	P

Dose experiments were conducted for each complex. These experiments determine the minimum amount of energy required to deposit a pattern that remains on the silicon after rinsing the selectively exposed film. Ethanol was used as the solvent to develop the films after photolysis. The zirconium, manganese and iron precursor films were spin coated from the commercially obtained solutions. Stock solutions were made for the remaining complexes by dissolving (or diluting) each complex in a minimum amount of CH_2Cl_2. For each precursor, the same stock solution was used to spin coat the precursor films for separate dose experiments. The dose requirement results are summarized in Table 6.7. The compound that required the smallest dose to leave a pattern after rinsing was lead (II) 2-ethylhexanoate. Thin films of the lead precursor required 10 sec photolysis with 4.4 mW cm^{-2} of 254 nm light to leave patterns on the surface after rinsing the film with ethanol. This dose corresponds to 44 mJ cm^{-2} required to pattern material from these precursors. Manganese and tin precursors required 10 min, or a dose of 2.6 Jcm^{-2}. Iron and titanium precursors required 30 minutes exposure time, corresponding to a dose of 7.9 Jcm^{-2}. The zirconium precursor films required 2 hours exposure, or a 32 Jcm^{-2} dose. Irradiation of films of nickel, calcium and lithium precursors resulted in patterns after 24 hours of exposure (380 Jcm^{-2}).

In order to determine the compatibility of our process with current lithography techniques, an attempt was made to pattern PZT on silicon. For this experiment a thin film of a stoichiometric mixture of the 2:1:1 ratio of precursors as described in *Section 6.2.4* was deposited on a Si(100) substrate. The film was irradiated through a mask for

90 min and, after rinsing the unexposed starting material with ethanol, 2 μm wide lines are visible (see Figure 6.6).

Figure 6.6 Optical micrograph of 2 x 50 μm lines produced by photolithography of a 2:1:1 Pb: Zr: Ti precursor mixture.

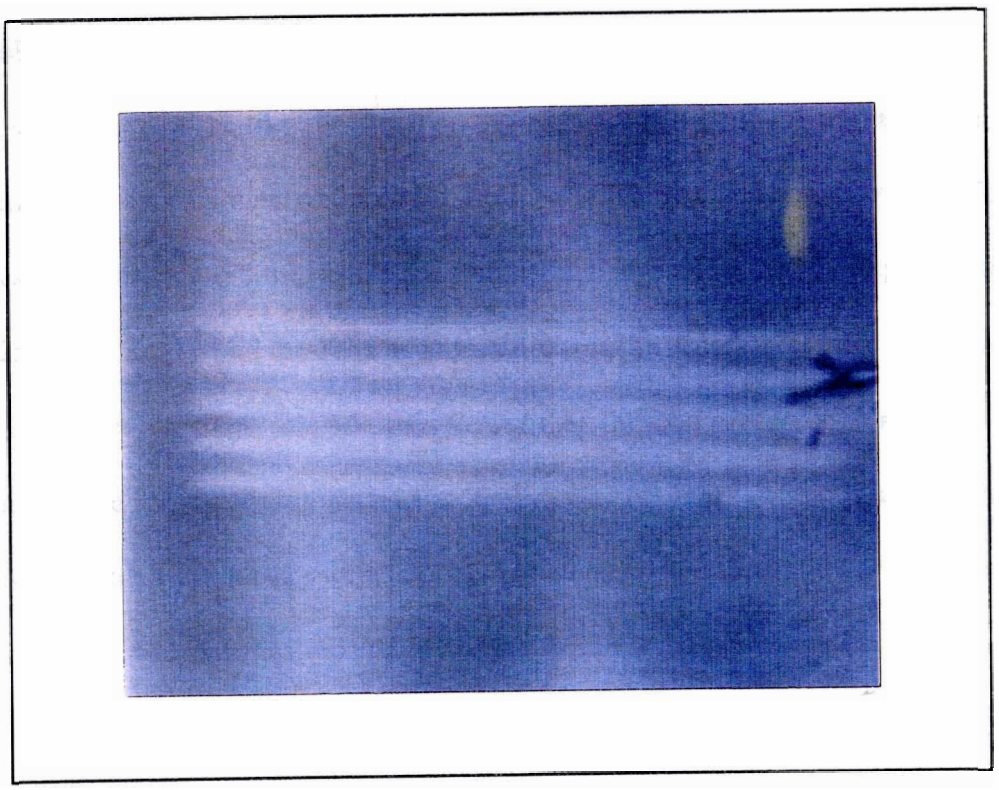

Dose requirements were also determined for the mixed precursor films. An amorphous film of a 2:1:1 stoichiometric mixture of the lead: zirconium: titanium precursors was spin coated onto silicon. The film was partially covered and irradiated for 1 min with a 4.4 mW cm^{-2} mercury lamp. The light source was removed and the film was uncovered and then dipped in ethanol. Both the exposed and unexposed regions of the film dissolved. Another film was made, and photolysed for 5 min, and the complete film dissolved also. When a film that was photolysed for 10 min was dipped in ethanol, the exposed portion of the film remained on the surface. Therefore the minimum dosage required was approximately 10 min (or 2.6 Jcm^{-2}). These experiments were performed for various dosages and the results are summarized in Table 6.7. The required dose for the 2:1:1 Pb: Zr: Ti and the 1:1 Pb: Ti mixture was the same (2.6 Jcm^{-2}) as that for the titanium precursor alone and 60 times slower than the lead precursor alone. However, the required dose for patterning the 1:1 Pb: Zr film was 1.3 Jcm^{-2}, which is approximately 26 times faster than when zirconium is patterned alone and 30 times slower than lead alone.

6.2.6 Film Morphology

To determine the thickness variation across a wafer for a spin coated film, the thickness was determined using ellipsometry. A 4" silicon wafer coated with $Zr(O_2CCH(C_2H_5)C_4H_9)_4$ using a spin-speed of 2000 rpm had a thickness of 3668 ± 38 Å.

The surface of a photoproduced film of amorphous ZrO_2 was imaged by atomic force microscopy. The results indicate that the surface of the film is smooth, with a root mean square roughness of 5.7 Å over a 1 μm square section. Over the 1 micron square area, 90% o :he surface fell within a 20 Å height range.

Figure 6.7 Atomic force micrograph of a 1 μm^2 surface of amorphous zirconium oxide.

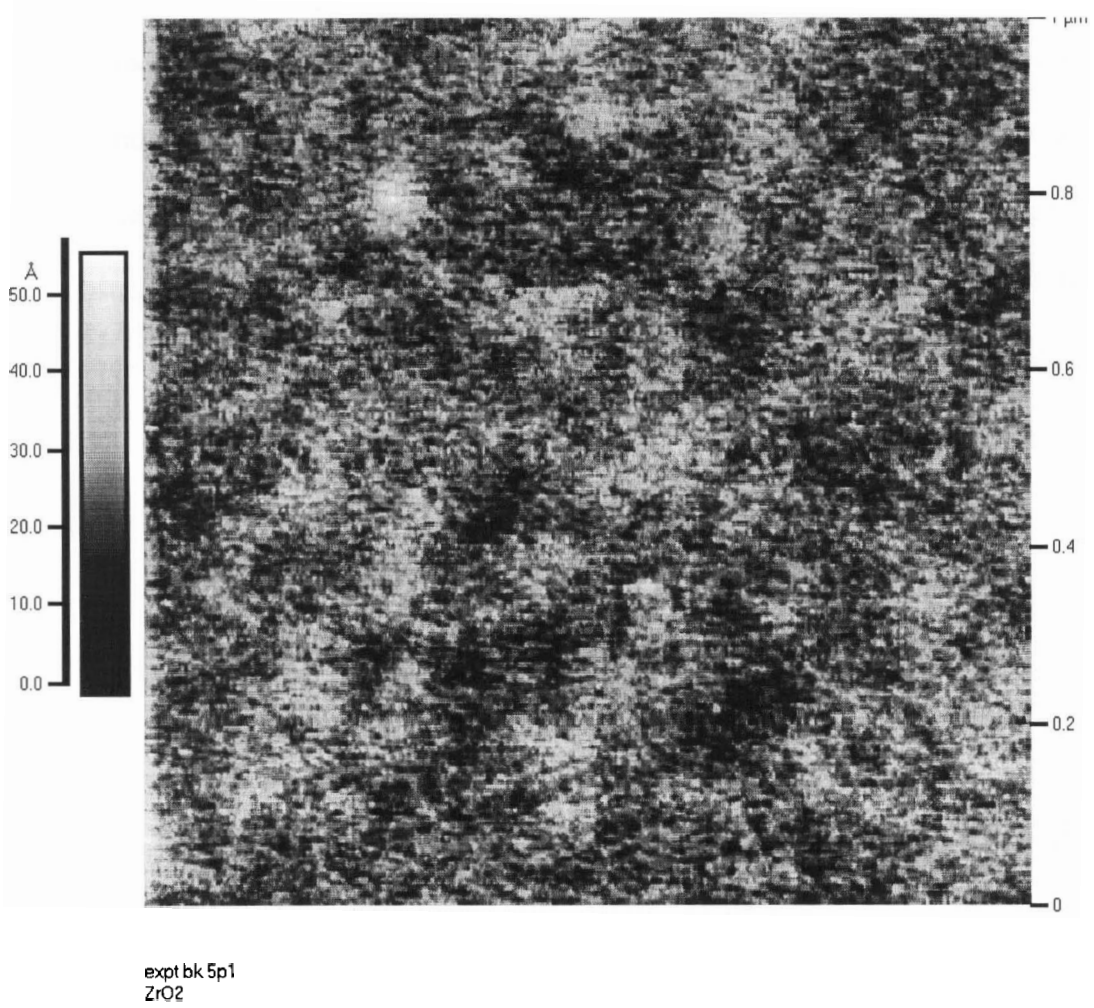

6.3 Discussion

Amorphous films of metal 2-ethylhexanoate complexes underwent primary photochemical reactions according to equation 6.12. Presumably, the 2-ethylhexanoate ligand is ejected as a radical and decarboxylates producing the products CO_2 and a heptyl radical. The radical can either combine with another heptyl radical, forming $C_{14}H_{30}$, or abstract a hydrogen from another radical forming 2-heptene or 3-heptene and heptane (equation 6.13). These products have been observed previously on photolysis of thin films of copper (II) 2-ethylhexanoate [50] and uranyl (VI) 2-ethylhexanoate [41].

$$M(O_2CCH(C_2H_5)C_4H_9)_x \xrightarrow{h\nu} \bullet M(O_2CCH(C_2H_5)C_4H_9)_{x-1} + CO_2 + \bullet CH(C_2H_5)C_4H_9 \qquad (6.12)$$

M(X) = Ni(II), Zr(IV), Pb(II), Mn(II), Fe(III), Ca(II), Li(I), Sn(II)

$$6 \bullet CH(C_2H_5)C_4H_9 \longrightarrow C_{14}H_{30} + C_2H_5CHCHC_3H_7 + CH_3CHCHC_4H_9 + 2\,C_7H_{16} \qquad (6.13)$$

Subsequent reactions of the metal 2-ethylhexanoate fragments were either thermal or photochemical depending on the metal. No FTIR bands that would indicate the formation of an intermediate were observed during the photolysis of the nickel, lead, iron, calcium, lithium and tin 2-ethylhexanoates. This indicates that the primary photoproducts underwent rapid thermal decomposition (equation 6.14).

In the case of the manganese and zirconium precursors, an additional photon was required. Manganese (II)- and zirconium (IV) 2-ethylhexanoate contain bridging,

bidentate and unidentate metal carboxylate bonds. Presumably, the primary photoreaction is loss of a terminal 2-ethylhexanoate radical, and the remaining bridged photoproduct is sufficiently stable to be observed in the FTIR spectrum. Upon further photolysis, the polymeric form breaks down and decomposes (equation 6.15).

$$\bullet M(O_2CCH(C_2H_5)C_4H_9)_{x-1} \xrightarrow{\Delta} M + (x-1)\,CO_2 + (x-1)\,\bullet CH(C_2H_5)C_4H_9 \qquad (6.14)$$

M(X) = Ni(II), Pb(II), Fe(III), Ca(II), Li(I), Sn(II)

$$(RCO_2)_x[\bullet M(O_2CR)_y]_n(O_2CR)_x \xrightarrow{h\nu} nM + (ny+2x)CO_2 + (ny+2x)\bullet R \qquad (6.15)$$

M(X) = Mn(II), Zr(IV); R= $CH(C_2H_5)C_4H_9$

Photolysis of $Ti(CH_3COCHCOCH_3)_2(OCH(CH_3)_2)_2$ resulted in loss of all ligands as indicated by the loss of all FTIR bands associated with the complex. Presumably, the primary photoreaction is loss of an acetylacetonate ligand (acac) as a radical (equation 6.16). This product is thermally unstable, and rapidly decomposes to yield titanium (equation 6.17). The ejected acac and isopropoxyl radicals may react, resulting in the abstraction of a hydrogen from an isopropoxyl radical, yielding acacH and acetone (equation 6.18). Hydrogen abstraction by an ejected acac radical has been observed previously, following photolysis of an amorphous film of uranyl acetylacetonate hydrate [41].

$$Ti(CH_3COCHCOCH_3)_2(OCH(CH_3)_2)_2 \xrightarrow{h\nu} \bullet Ti(CH_3COCHCOCH_3)(OCH(CH_3)_2)_2 + \bullet CH_3COCHCOCH_3 \qquad (6.16)$$

$$\bullet Ti(CH_3COCHCOCH_3)(CH(CH_3)_2)_2 \xrightarrow{\Delta} Ti + \bullet CH_3COCHCOCH_3 + \bullet OCH(CH_3)_2 \quad (6.17)$$

$$\bullet CH_3COCHCOCH_3 + \bullet OCH(CH_3)_2 \longrightarrow CH_3COCH_2COCH_3 + OC(CH_3)_2 \quad (6.18)$$

Auger spectroscopic results indicate that all of the metal products formed in equations 6.14, 6.15 and 6.17 react with air to form the metal oxide. Amorphous films produced from photolysis of lithium and nickel precursors were contaminated with carbon. The similarity between these three complexes was that they were only sparingly soluble and a drop of 2-ethylhexanoic acid was added to aid in the dissolution of the complexes. These results indicate that the 2-ethylhexanoates of nickel and lithium, are not ideal precursors for the photodeposition of the pure metal oxides. An alternate choice of alkyl group, R, in the carboxylate (O_2CR) ligand, may improve the solubility of these precursors. All other systems yielded pure metal oxides.

Photolysis of amorphous films of the complexes studied in this chapter results in the loss of all ligands, and, in the presence of air produce metal oxide films. Photolithography experiments demonstrated that direct patterning of metal oxides from amorphous films of inorganic precursors can be achieved. Minimum dose measurements indicate that the selective photolysis of lead(II) 2-ethylhexanoate films require 44 $mJcm^{-2}$. This is comparable to dosage requirements for photoresists. A typical dose for patterning of a diazonaphthaquinone (DNQ)/novolak resist system is approximately 55 $mJcm^{-2}$ [129]. This indicates that this method of photolithographic deposition of lead oxide is more efficient than present resist technology. It should be noted that the patterns made

during dose experiments are a result of solubility change. It does not necessarily infer reaction completion. The most important factor for us to minimize is the dose because the equipment used in industry for photolithography has a very high capital cost. The resultant patterns can later be converted to pure material following lithography by either nonselective irradiation or heat, depending on the application.

The precursors, with the exception of lead, require 2.6 to 380 Jcm^{-2}, which is approximately 47 to 6900 times more than current photoresists. It should be noted that, although these are the required doses given the conditions of the experiment, some conditions may be altered to reduce the required dose. For example, an alternate rinsing solvent may increase the differential solubility between the exposed and unexposed portions of the film.

Photolithography of a 2: 1: 1 Pb: Zr: Ti precursor mixture resulted in the formation of 2 x 50 μm lines. Dose requirements for patterning of mixed metal oxides were made. The required dose for both Pb: Zr: Ti (2: 1: 1) and Pb: Ti (1: 1) was 2.6 Jcm^{-2}. This dose is the same as that found for the titanium precursor alone. The required dosage for Pb: Zr (1: 1) was 1.3 Jcm^{-2}, which is approximately 25 times less than when the zirconium precursor is irradiated alone. It is apparent that the addition of the lead precursor to the zirconium precursor, reduces the recombination of the zirconium photofragments. This results in more efficient decomposition of the zirconium precursor. These results indicate that a mixture of precursors may improve the efficiency of photodecomposition.

The required dose for pattern formation was found to change with the addition of

another precursor complex. The use of multiple component precursors may be used to design a precursor system that would improve the efficiency of decomposition. This may be applied not only to the deposition of mixed metal oxides but also to deposition of binary metal oxides, M_xO_y. For example, the photodeposition of zirconium oxide may be enhanced by mixing the zirconium (IV) 2-ethylhexanoate with another zirconium carboxylate. The change in environment of the precursor may reduce the stability of the primary photoproducts, resulting in more rapid decomposition. It could also increase the differential solubility between the exposed and unexposed regions of the film. These changes could result in smaller dose requirements for patterning.

Photodeposition from an amorphous film with a 2:1:1 ratio of Pb: Zr: Ti precursors yielded a pure, amorphous mixed metal oxide film. X-ray powder diffraction experiments confirmed the polycrystalline formation of the tetragonal phase of $Pb(Zr_{0.52}Ti_{0.48})O_3$, when the amorphous film was annealed at 650 °C for 30 min. The predominant orientation was the (211) orientation, with c/a = 1.030. This result is consistent with the literature report for the c/a ratio of 1.027 for the tetragonal polycrystalline $Pb(Zr_{0.52}Ti_{0.48})O_3$ [127]. Also present was the pyrochlore phase, by observation of the broad signal at approximately $2\theta = 30°$. This phase is a lead deficient phase of $Pb(Zr_{0.52}Ti_{0.48})O_3$ (PZT), which is caused by evaporation of PbO from the film during the annealing process.

The film was not primarily (111) oriented on the Pt(111) surface, which may be a result of the method of annealing. If the PZT was preferentially (111) oriented on Pt(111) we would expect a single signal at approximately 38.3°, close to the Pt(111) signal (2θ =

39.8°) [34]. This may be due to the method of annealing. The length of time the film and substrate are annealed, affects both the film and the substrate. Oxygen can diffuse through the PZT and the Pt layer into the Ti layer, forming TiO_2. This would result in expansion of the Ti layer causing lateral stresses on the Pt(111) layer. This has been demonstrated previously for annealing studies of PZT on Pt(111)/Ti/Si [34]. If the sample was annealed using a rapid thermal process, the film crystallized preferentially (111) oriented, and was polycrystalline when furnace-annealed [34].

6.4 Conclusions

In this study , it has been demonstrated that elementally pure amorphous metal oxide thin films of Zr, Pb, Ti, Mn, Fe, Ca and Sn may be prepared photochemically from thin film precursors at room temperature by our method. This demonstrates that metal carboxylate as well as acetylacetonate compounds are suitable precursors for the deposition of metal oxides. If a mixture of these precursors are codeposited, the mixed metal oxide was produced.

A novel method for the deposition of thin films of $Pb(Zr_xTi_{1-x})O_3$ has been demonstrated. Amorphous films of $Pb_{1.1}(Zr_{0.48}Ti_{0.52})O_{2.9}$ were prepared by photolysis of a 2: 1: 1 film mixture of lead: zirconium: titanium precursors. Thermal annealing studies indicated that the polycrystalline tetragonal phase of $Pb(Zr_{0.48}Ti_{0.52})O_3$ was produced.

The dosage required for the lead (II) 2-ethylhexanoate precursor was 44 mJ cm^{-2} and is comparable current photoresist technology. Dose experiments indicate that the energy required to leave a pattern on silicon is one to three orders of magnitude greater

than current photoresist technology for manganese, tin, zirconium, titanium and iron. Alternate rinsing solvents may be necessary which may improve the selective solubility of the product and precursor materials. Otherwise, different metal carboxylates as precursors, may photodecompose more efficiently. Optical lithography of 2 x 50 μm lines of PZT demonstrated compatibility with current lithography technology.

6.5 Experimental details

6.5.1 Instruments and materials

The silicon wafers were obtained from Wafernet Incorporated. Si (100) surfaces were used in these studies and the wafers were p-type silicon with tolerances and specifications as per SEMI Standard M1.1.STD.5 cut to the approximate dimensions 10 x 12 mm as needed. The substrates used for PZT deposition were Si(111) wafers coated with 1000 Å of titanium and 2000 Å of Pt(111). These wafers were prepared and donated by Northern Telecom Canada.

The Fourier transform infrared (FTIR) spectra were obtained with 4 cm^{-1} resolution using a Bomem Michelson 120 FTIR spectrophotometer. FTIR spectra of the thin films.on silicon were obtained in air with Si (100) used as a reference.

The photolysis beam was the output from a UVP Inc. model UVG-54 short wave UV-254 nm lamp. All photolysis experiments were performed in air. Light intensity measurements were made using an International Light IL 1350 radiometer.

Auger spectra were obtained using a PHI double pass CMA at 0.85 eV resolution at the Surface Physics Laboratory, Department of Physics, Simon Fraser University. The

chromium plated quartz lithography mask was kindly donated by IBM Corp. The light source used for lithography experiments was an Osram 150 W high pressure Xe lamp. The resultant lithography images were printed on a Mitsubishi Colour Video Printer CP-10U. Grazing incidence X-ray diffraction patterns were obtained using a Siemens D5000 X-ray diffractometer, Department of Physics, Simon Fraser University. The X-ray source was a Cu Kα (1.54 Å) beam. The atomic force microscope (AFM) image was obtained using a Park Scientific Instruments Inc. Autoprobe CP NC-AFM in contact mode, Department of Physics, Simon Fraser University.

6.5.2 Preparation of amorphous precursor films

The complexes were obtained commercially as follows. The 2-ethylhexanoates of Pb, Li, and Sn were obtained as viscous liquids. The complexes $M(O_2CCH(C_2H_5)C_4H_9)_x$ (M(X)= Ni(II), Ca(II)), existed as 78% and 40% solutions, respectively, in 2-ethylhexanoic acid. The complexes $M(O_2CCH(C_2H_5)C_4H_9)_x$ (M(X)= Zr(IV), Mn(II) and Fe(III)), were obtained as solutions in mineral spirits. The $Ti(CH_3COCHCOCH_3)_2(OC(CH_3)_2)_2$ complex was obtained as a 75% solution in isopropanol.

The following is a typical procedure for thin film preparation. A silicon chip was placed on a Teflon platform attached to a motor. The motor was turned on and the silicon chip started spinning. A drop of a solution of $Mn(O_2CCH(C_2H_5)C_4H_9)_2$ dissolved in CH_2Cl_2 solvent was dispensed from a disposable pipette onto the silicon chip. The solution was allowed to spread and the solvent to evaporate. At this point, the motor was

turned off and a thin film of the complex remained on the chip.

A 2: 1: 1 mole ratio precursor mixture of lead: zirconium: titanium as prepared as the precursor mixture for $Pb(Zr_{0.5}Ti_{0.5})O_3$. A 0.442 g sample of lead (II) 2-ethylhexanoate (0.00089 mol Pb) was dissolved in CH_2Cl_2. To this solution, 0.217 g (0.000447 mol Ti) of a 75% solution of $Ti(acac)_2(i\text{-}prop)_2$ in isopropanol was added. Then 0.677 g (0.000445 mol Zr) of Zr(IV) 2-ethylhexanoate in mineral spirits (6% Zr).

6.5.3 Photolysis of the complexes as thin films on silicon surfaces

The Si (100) surface was used as the substrate in all experiments. A typical experiment will be described. An FTIR spectrum of silicon was obtained and used as a reference throughout the experiment. A thin, amorphous film of $Mn(O_2CCH(C_2H_5)C_4H_9)_2$ was deposited on silicon as described in Section *6.5.2*. An FTIR spectrum was then obtained (see Figure 6.1). The sample was placed in the irradiation beam, exposed for 15 min and another FTIR spectrum was obtained. The extent of reaction was monitored by the changes in intensity of the FTIR bands associated with the complex. This procedure was repeated for accumulated photolysis times of 30, 60 min and 24 hours at which time the FTIR absorptions due to the ligands in the precursor complex decreased to zero intensity. When the intensity of the bands were at the baseline, the sample was then moved to the scanning Auger microprobe for further analysis. Auger spectra were obtained to determine if all the ligands were extruded from the film and to determine the composition of the films. The results are summarized in

Table 6.4.

6.5.4 Lithography

Lithography experiments were performed as follows. The mask was placed in contact with a thin amorphous film of a precursor. The film was irradiated through the mask, and after photolysis, the film was rinsed with ethanol to remove unexposed starting material.

Dosage experiments were conducted in the following manner. Amorphous films of the precursors on Si(100) were made by spin-coating. The precursor films were partially masked with blank silicon chips and irradiated with a 254 nm mercury lamp. The light intensity measured at 4.4 mW/cm^2. After 10 minutes, the light was removed and the films were rinsed with ethanol. Dosages of 10 sec, 1 min, 5 min, 10 min, 30 minutes, 2 hours and 24 hours were also attempted. The results are summarized in Table 6.7. The required dosage for a complex is the amount of energy required to produce a pattern that remains on the substrate after rinsing with solvent.

References

1. C. G. Dupuy, D. B. Beach, J. E. Hurst, Jr. and J. M. Jasinski, *Chem. Mater.* **1**, 16 (1989).

2. D. K. Liu, R. J. Chin and A. L. Lai, *Chem. Mater.* **3**, 13 (1991).

3. N. H. Dryden, R. Kumar, E. Ou, M. Rashidi, S. Roy, P. R. Norton, R. J. Puddephatt and J. D. Scott, *Chem. Mater.* **3**, 677 (1991).

4. H. H. Gilgen, T. Cacouris, P. S. Shaw, R. R. Krchnavek and R. M. Osgood, *Appl. Phys. B* **42**, 55 (1987).

5. M. J. Rand, *J. Electrochem. Soc.* **120**, 686 (1973).

6. J. E. Gozum, D. M. Pollina, K. A. Jensen and G. S. Girolami, *J. Am. Chem. Soc.* **110**, 2688 (1988).

7. G. Meyer and J. Saura, *J. Mater. Sci. Lett.* **11**, 143 (1992).

8. B. J. Tan, L. Hwan and S. L. Suib, *Chem. Mater.* **3**, 368 (1991).

9. H.-T. Chiu and W.-P. Chang, *J. Mater. Sci. Lett.* **11**, 570 (1992).

10. C.-S. Jun, T. P. Fehlner and G. J. Long, *Chem. Mater.* **4**, 440 (1992).

11. T. H. Baum and C. E. Larson, *Chem. Mater.* **4**, 365 (1992).

12. W. B. Chou, M. N. Azer and J. Mazumder, *J. Appl. Phys.* **66**, 191 (1989).

13. C. Niu and C. M. Leiber, *J. Am. Chem. Soc.* **114**, 3570 (1992).

14. N. S. Gluck, Z. Ying, C. E. Bartosch and W. Ho, *J. Chem. Phys.* **86**, 4957 (1987).

15. J. R. Creighton and J. E. Parmeter, *Crit. Rev. in Solid State and Mat. Sci.* **18**, 175 (1993).

16. I. P. Herman, *Chem. Rev.* **89**, 1323 (1989).

17. C. J. Brinker and G. W. Scherer, *Sol-Gel Science: The Physics and Chemistry of Sol-Gel Processing*, Boston: Academic Press Inc. (1990).

18. W. S. Ruska, *Microelectronics Processing: An Introduction to the Manufacture of Integrated Circuits*, New York: McGraw-Hill (1987).

19. J. L. Vossen and W. Kern, Eds., *Thin Film Processes II*, San Diego: Academic Press (1991).

20. K. Wasa and S. Hayakawa, *Handbook of Sputter Deposition Technology: Principles, Technology and Applications*, New Jersey: Noyes Publications (1992) p. 23.

21. D. L. Smith, *Thin Film Deposition: Principles and Practice*, New York: McGraw-Hill, Inc. (1995).

22. L. F. Thompson, C. G. Wilson and M. J. Bowden, *Introduction to Microlithography*, 2nd ed., Washington, D. C.: American Chemical Society (1994).

23. S. P. Murarka and S. W. Hymes, *Crit. Rev. in Solid State and Mat. Sci.* **20**, 87 (1995).

24. P. P. Sahay, M. Shamsuddin and R. S. Srivastava, *Microelec. J.* **23**, 625 (1992).

25. B. G. Streetman, *Solid State Electronic Devices*, 2nd ed., New Jersey: Prentice-Hall (1980).

26. S. M. Sze, ed., *Semiconductor Sensors*, New York: John Wiley & Sons (1994).

27. C. A. Harper and R. N. Sampson, Eds., *Electronic Materials and Processes Handbook*, 2nd ed., New York: McGraw-Hill, Inc. (1994) Chapter 8.

28. A. Nagy and J. Helbert, *Solid State Technol.*, **34**, 77 (1991).

29. C. G. Granqvist, *Handbook of Inorganic Electrochromic Materials*, Amsterdam: Elsevier Science B. V. (1995).

30. M. E. F. Baudais and J. R. Dahn, *Solid State Ionics* **66**, 175 (1993).

31. J. R. Dahn, U. von Sacken, M. W. Juzkow and H. Al-Janaby, *J. Electrochem. Soc.* **138**, 2207 (1991).

32. K. Tominaga, Y. Sakashita, H. Nakashima and M. Okada, *J. Cryst. Growth* **145**, 219 (1994).

33. J.-H. Choi and H.-G. Kim, *J. Appl. Phys.* **74**, 6413 (1993).

34. Y. S. Hwang, S. H. Paek, C. S. Park, J. P. Mah, J. S. Choi, J. K. Jung and Y. N. Kim, *J. Mat. Sci. Lett.* **14**, 1168 (1995).

35. J. F. Scott and C. A. Paz de Araujo, *Science* **246**, 1400 (1989).

36. K. -H. Hellwege, Ed. in chief, *Landolt-Börnstein New Series, Group III Volume 16, Ferroelectrics and Related Substances*, Berlin: Springer-Verlag (1981) pp. 663-679.

37. S. S. Dana, K. F. Etzold and J. Clabes, *J. Appl. Phys.* **69**, 4398 (1991).

38. M. Sayer, C. V. R. Vasant Kumar, D. Barrow, L. Zou and D. T. Amm, *Mater. Res. Soc. Symp. Proc.* **243**, 39 (1992).

39. V. Balzani and V. Carassiti, *Photochemistry of Coordination Compounds*, 1st ed., New York: Academic Press (1970).

40. G. J. Ferraudi, *Elements of Inorganic Photochemistry*, New York: Wiley (1988).

41. M. Gao, *Solid State Photochemistry of Uranyl Carboxylate and 1,3-Diketonate Complexes: Photochemical Patterning of Uranium Oxide Lines via Uranyl Complex Thin Film Precursors*, M. Sc. Thesis, Simon Fraser University (1995).

42. B. J. Palmer, *Photochemistry of Inorganic and Organometallic Complexes in Various Media*, Ph. D. Thesis, Simon Fraser University (1992).

43. A. Becalska, R. J. Batchelor, F. W. B. Einstein, R. H. Hill and B. J. Palmer, *Inorg. Chem.* **31**, 3118 (1992).

44. A. Gupta and R. Jagannathan, *Appl. Phys. Lett.* **51**, 2254 (1987).

45. D. Briggs and M. P. Seah, in *Practical Surface Analysis by Auger and X-ray Photoelectron Spectroscopy*, New York: John Wiley & Sons (1983).

46. D. A. Skoog, *Principles of Instrumental Analysis*, 3rd ed., New York: Saunders College Publishing (1985).

47. S. L. Flegler, J. W. Heckman, Jr., and K. L. Klomparens, *Scanning and Transmision Electron Microscopy. An Introduction*, New York: W. H. Freeman and Company (1993).

48. A. Guinier, *X-Ray Diffraction in Crystals, Imperfect Crystals, and Amorphous Bodies*, San Fransisco: W. H. Freeman and Company (1963).

49. J. C. Anderson and K. D. Leaver, *Materials Science*, New York: Van Nostrand Reinhold Company (1969).

50. A. A. Avey and R. H. Hill, *J. Am. Chem. Soc.* **118**, 237 (1996).

51. L. B. Goetting, B. J. Palmer, M. Gao and R. H. Hill, *J. Mater. Sci.* **29**, 6147 (1994).

52. D. M. L. Goodgame and L. M. Venanzi, *J. Chem. Soc. A* 616 (1963).

53. D. M. L. Goodgame and L. M. Venanzi, *J. Chem Soc. A* 5909 (1963).

54. A. W. Adamson, *J. Phys. Chem.* **71**, 798 (1967).

55. S. K. Weit and C. Kutal, *Inorg. Chem.* **29**, 1455 (1990).

56. F. Scandola, C. Bartocci and M. A. Scandola, *J. Phys. Chem.* **78**, 572 (1974).

57. F. Scandola, C. Bartocci and M. A. Scandola, *J. Am. Chem. Soc.* **95**, 7898 (1973).

58. J. F. Endicott, *Inorg. Chem.* **14**, 448 (1975).

59. L. Costanzo, A. Giuffrida, G. Guglielmo and V. Ricevuto, *Inorg. Chim. Acta* **33**, 29 (1979).

60. B. J. Palmer and R. H. Hill, *J. Photochem. Photobiol. A: Chem.* **72**, 243 (1993).

61. G. J. Ferraudi, *Elements of Inorganic Photochemistry*, New York: Wiley (1988) p.155.

62. A. K. Mukherjee, M. Mukherjee, A. J. Welch, A. Ghosh, G. De and N. R. Chaudhuri, *J. Chem. Soc. Dalton Trans.* 997 (1987).

63. D. M. L. Goodgame and M. A. Hitchman, *Inorg. Chem.* **4**, 721 (1965).

64. K. Nakamoto, *Infrared and Raman Spectra of Inorganic and Organometallic Compounds*, 4th ed., New York: John Wiley & Sons (1986).

65. a) D. M. L. Goodgame and M. A. Hitchman, *Inorg. Chem.* **5**, 1303 (1966).
b) M. A. Hitchman and G. L. Rowbottom, *Coord. Chem. Rev.* **42**, 55 (1982).

66. S. Koner, A. Ghosh and N. R. Chaudhuri, *J. Chem. Soc. Dalton Trans.* 1563 (1990).

67. D. M. L. Goodgame, M. A. Hitchman and D. F Marsham, *J. Chem. Soc. A* 259 (1971).

68. R. Birdy, D. M. L. Goodgame, J. C. McConway and D. Rogers, *J. Chem. Soc. Dalton Trans.* 1730 (1977).

69. A. E. Shvelashvili, M. A. Porai-Koshits, A. I. Kvitashvili and B. M. Shchedrin, *Zh. Strukt. Khim.* **15**, 307 (1974).

70. M. G. B. Drew, D. M. L. Goodgame, M. A. Hitchman and D. Rogers, *J. Chem. Soc. Chem. Commun.* 477 (1965).

71. N. F. Curtis and Y. M. Curtis, *Inorg. Chem.* **4**, 804 (1965).

72. J. T. Yardley, B. Gitlin, G. Nathanson and A. M. Rosan, *J. Chem. Phys.* **74**, 370 (1981).

73. G. L. Geoffroy, M. S. Wrighton, *Organometallic Photochemistry*, New York: Academic Press (1979).

74. S. K. Nayak and T. J. Burkey, *J. Am. Chem. Soc.* **115**, 6391 (1993).

75. D. K. Liu, C. G. Brinkley and M. S. Wrighton, *Organomet.* **3**, 1449 (1984).

76. M. Poliakoff and J. J. Turner, *J. Chem. Soc. Faraday Trans.* **70**, 93 (1974).

77. M. Poliakoff, *J. Chem. Soc. Dalton Trans.* 210 (1974).

78. R. D. Sanner, R. G. Austin, M. S. Wrighton, W. D. Honnick and C. U. Pittman, Jr., *Inorg. Chem.* **18**, 928 (1979).

79. D. Sunil, J. Sokolov, M. H. Rafailovich, X. Duan and H. D. Gafney, *Inorg. Chem.* **32**, 4489 (1993).

80. S. B. Butts and D. F. Shriver, *J. Organomet. Chem.* **169**, 191 (1979).

81. P. A. Dawson, B. M. Peake, B. H. Robinson and J. Simpson, *Inorg. Chem.* **19**, 465 (1980).

82. S. M. Grant and A. R. Manning, *Inorg. Chim. Acta* **31**, 41 (1978).

83. T. R. Gaffney and J. A. Ibers, *Inorg. Chem.* **21**, 2851 (1982).

84. D. F. Shriver, P. Atkins and C. H. Langford, *Inorganic Chemistry*, 2nd ed., New York: W. H. Freeman and Company (1994) p. 293.

85. L. E. Davis, N. C. MacDonald, P. W. Palmberg, G. E. Riach and R. E. Weber, *Handbook of Auger Electron Spectroscopy: A reference book of Standard Data for Identification and Interpretation of Auger Electron Spectroscopy Data*, 2nd

ed., Eden Prairie, MN: Physical Electronics Division Perkin-Elmer Corp. (1976), p. 12.

86. H. L. Conder and M. Y. Darensbourg, *J. Organomet. Chem.* **67**, 93 (1974).

87. W. O. Siegl, *J. Organomet. Chem.* **92**, 321 (1975).

88. 19 $Å^3$ per non-H atom was used for the calculation.

89. R. Kumar, S. Roy, M. Rashidi and R. J. Puddephatt, *Polyhedron* **8**, 551 (1989).

90. T. W. H. Ho, S. L. Blair, R. H. Hill and D. G. Bickley, *J. Photochem. Photobiol. A: Chem.* **69**, 229 (1992).

91. D. G. Bickley, R. H. Hill and C. I. Horvath, *J. Photochem. Photobiol A: Chem.* **67**, 181 (1992).

92. H. Hennig, R. Stich, D. Rehorek, P. Thomas and T. J. Kemp, *Inorg. Chim. Acta* **143**, 7 (1988).

93. H. Knoll, R. Stich, H. Hennig and D. J. Stufkens, *Inorg. Chim. Acta* **178**, 71 (1990).

94. H. Hennig, R. Stich, H. Knoll and D. Rehorek, Z. *Anorg. Allg. Chem.* **576**, 139 (1989).

95. R. Tian, J. C. Facelli and J. Michl, *J. Phys. Chem.* **92**, 4073 (1988).

96. C. R. Brazier, P. F. Bernath, J. B. Burkholder and C. J. Howard, *J. Chem. Phys.* **89**, 1762 (1988).

97. B. J. Palmer, A. Becalska, T. W. H. Ho and R. H. Hill, *J. Mater. Sci.* **28**, 6013 (1993).

98. a) M. J. Shaw and D. G. Bickley, unpublished results (1988).
b) H. C. Clark and L. E. Manzer, *J. Organomet. Chem.* **59**, 411 (1973).

99. E. E. Wegner and A. W. Adamson, *J. Am. Chem. Soc.* **88**, 394 (1966).

100. G. J. Ferraudi, J. F. Endicott and J. Barber, *J. Am. Chem. Soc.* **97**, 6406 (1975).

101. P. Riccieri and E. Zinato, *Proc. Intl. Conf. Coord. Chem., IUPAC* 252 (1972).

102. L. Moggi, F. Boletta, V. Balzani and F. Scandola, *J. Inorg. Nucl. Chem.* **28**, 2589 (1966).

103. A. W. Adamson and A. H. Sporer, *J. Inorg. Nucl. Chem.* **8**, 209 (1958).

104. A. W. Adamson, A. Chiang and E. Zinato, *J. Am. Chem. Soc.* **91**, 5467 (1969).

105. D. T. Doughty, G. Gordon and R. P. Stewart, Jr., *J. Am. Chem. Soc.* **101**, 2645 (1979).

106. C. R. C. Coussmaker, M. H. Hutchinson, J. R. Mellor, L. E. S. Sutton and L. M. Venanzi, *J. Chem. Soc.* (1961) 2705.

107. J. M. Solar, M. A. Ozkan, H. Isci and W. R. Mason, *Inorg. Chem.* **23**, 758 (1984).

108. A. Merle, M. Dartiguenave and Y. Dartiguenave, *J. Molec. Struct.* **13**, 413 (1972).

109. J. Nelson and S. M. Nelson, *J. Chem. Soc. A* 1597 (1969).

110. R. A. Bailey, S. L. Kozak, T. W. Michelson and W. L. Mills, *Coord. Chem. Rev.* **6**, 407 (1971).

111. P. L. Goggin and R. J. Goodfellow, *J. Chem. Soc. A* 1462 (1966).

112. A. B. P. Lever, *Inorganic Electronic Spectroscopy*, 2nd ed., Netherlands: Elsevier Science Publishers B. V., 1984.

113. P. W. Atkins, *Physical Chemistry*, 3rd ed., New York: W. H. Freeman and Company, 1986.

114. Oriel Corporation Volume II: *Light Sources, Monochromators, Detection Systems*, Stratford, CT (1989) p. 81.

115. K. A. Jenson, P. H. Nielson, C. T. Peterson, *Acta Chem. Scand.* **17**, 1113 (1963).

116. R. D. Feltham, *Inorg. Chem.* **3**, 116 (1964).

117. J. Chatt, A. Duncanson, B. M. Gatehouse, J. Lewis, R. S. Nyholm, M. L. Tobe, P. F. Todd and L. M. Venanzi, *J. Chem. Soc.* 4073 (1959).

118. P. Rigo, C. Pecile and A. Turco, *Inorg.Chem.* **6**, 1636 (1967).

119. S. Wolf, *Silicon Processing for the VLSI Era, Vol. 2*, Sunset Beach, CA: Lattice Press (1986).

120. Y. Xu, *Ferroelectric Materials and Their Applications*, Amsterdam: North-Holland (1991).

121. R. C. Mehrotra and R. Bohra, *Metal Carboxylates*, London: Academic Press (1983).

122. a) D. C. Bradley and C. E. Holloway, *Chem. Commun.* 284 (1965).
b) D. C. Bradley and C. E. Holloway, *J. Chem. Soc. A* 282 (1969).

123. P. Kofstad, *Nonstoichiometry, Diffusion and Electrical Conductivity in Binary Metal Oxides*, New York: Wiley-Interscience (1972).

124. L. E. Davis, N. C. MacDonald, P. W. Palmberg, G. E. Riach and R. E. Weber, *Handbook of Auger Electron Spectroscopy: A reference book of Standard Data for Identification and Interpretation of Auger Electron Spectroscopy Data*, 2nd ed., Eden Prairie, MN: Physical Electronics Division Perkin-Elmer Corp. (1976).

125. A. A. Avey and R. H. Hill, unpublished results.

126. S. G. Yoon and H. G. Kim, *IEEE Trans. Ultrasonics, Ferroelectrics and Frequency Control* **37**, 333 (1990).

127. K. Kakegawa, J. Mohri, T. Takahashi, H. Yamamura and S. Shirasaki, *Solid State Commun.* **24**, 769 (1977).

128. JCPDS-ICDD, file number 33-784.

129. R. Dammel, *Diazonaphthaquinone-based Resists, Volume TT 11*, SPIE-The International Society for Optical Engineering, Washington, USA (1993) p. 11.